Multiscale Modelling of Radiation Induced Microstructure Evolution: Assessment of Spent Fuel Element Integrity for Extended Interim Storage

Von der Fakultät für Georessourcen und Materialtechnik der
Rheinisch-Westfälischen Technischen Hochschule Aachen

zur Erlangung des akademischen Grades einer

Doktorin der Ingenieurwissenschaften

genehmigte Dissertation

vorgelegt von

Neslihan Yanikömer, M. Sc.

Berichtende: **Univ.-Prof. Dr.rer. nat. Klaus Fischer-Appelt**
Prof. Dr.rer. nat. Rahim Nabbi
Univ.-Prof. Dr.-Ing. Axel Preuße

Tag der mündlichen Prüfung: 24.08.2023

Diese Dissertation ist auf den Internetseiten der Universitätsbibliothek online verfügbar

KURZFASSUNG

Für den in der Bundesrepublik Deutschland anfallenden hochaktiven Abfall, nach bisheriger Prognose abgebrannte Brennelemente mit einer Schwermetallmasse von etwa 10.500 t, sieht das derzeitige Konzept eine Zwischenlagerung von bis zu 40 Jahren vor. Nach derzeitigem Kenntnisstand werden die zulässigen Lagerungszeiträume jedoch überschritten, was eine Erweiterung des Sicherheitsnachweises erfordert. Im Rahmen eines vom BMUV geförderten Forschungsprojekts zielt die vorliegende Doktorarbeit darauf ab, ein Multiskalenverfahren zu entwickeln und anzuwenden, welches Aufschluss über den Ablauf der mehrstufigen strahleninduzierten Schädigung der Hüllrohre der abgebrannten Brennelemente und Auswirkungen auf die strukturmechanischen Eigenschaften des Hüllrohrs gibt.

Die Hüllrohre der Brennstäbe der Brennelemente sind nach der Brennstoffmatrix die letzte Barriere gegen einen Austritt der im Brennstoff enthaltenen Radionuklide. Dementsprechend ist die Untersuchung der strukturellen Integrität der abgebrannten Brennelemente von zentraler Bedeutung für weitere Sicherheitsaussagen hinsichtlich der langfristigen Zwischenlagerung. Unter verschiedenen Schädingsprozesse sind strahleninduzierte Schädigung des Hüllrohrmaterials und die daraus resultierenden strukturmechanischen Auswirkungen von besonderer Bedeutung für die Integrität der BE. Hierbei handelt es sich um eine vielschichtige Prozesskette, die sich auf der atomischen Ebene der Schädigung beginnt und sich bis zur makroskopischen Ebene mit der strukturmechanischen Veränderung des Hüllrohrmaterials erstreckt.

Als erster Schritt des Multi Skalen Verfahrens werden unter Anwendung der Monte-Carlo-Methode die Auswirkungen des Strahlungsfeldes auf das Hüllrohrmaterial (Zircalloy-4) der Brennelemente simuliert. Dabei wird die Energieverteilung der atomaren Primärdefekte für eine typische LWR-Betriebsphase mit dem neutronenphysikalischen Code SPECTER ermittelt. Im Rahmen der nächsten Schädigungsstufe wird nach dem molekulardynamischen Verfahren, mit dem Programm LAMMPS die Simulation der Entwicklung der Defektkaskaden im Gitter des Zry-4-Materials durchgeführt, wobei die räumliche

Verteilung, das Energiespektrum und die Dichte der Zwischengitteratome und Leerstellen am Ende der Kaskadenphase bestimmt werden.

Anschließend werden, im Anschluss an die Kaskadenphase, die Modellierung und Simulation der Wechselwirkung der Defektkaskaden untereinander sowie ihre Diffusion durch das multikristalline Metallgitter durchgeführt. Dies erfolgt auf der Basis der KMC-Methode (objektkinetische Monte-Carlo-Methode), wobei die Größen- und Dichteverteilung von Defektclustern bzw. Mikrostrukturen sowie deren Agglomerationsgrad in Abhängigkeit von der Bestrahlungsdosis simuliert bzw. bestimmt werden. Außerdem wird die zeitliche Veränderung dieser strahleninduzierten Mikrostrukturen für verschiedene Lagerphasentemperaturen unter Anwendung einer Cluster-dynamischen Routine und ratentheoretischer Algorithmen untersucht und bestimmt. Im Hinblick auf die Prüfung und Validierung des gesamten multiskalen Modells werden die Ergebnisse der Modellrechnungen und Simulationen mit denen aus TEM-Messung (Transmissions-Elektronen-Mikroskopie) über die Verteilung und den Aufbau strahleninduzierter Mikrostrukturen verglichen. Mit dieser Untersuchung wird im Rahmen der Variationsbreite der experimentellen Messdaten und der Ergebnisse der einzelnen Simulationsmodelle die Genauigkeit des Multiskalenverfahrens bestätigt.

Aufgrund der Auswirkungen der mikrostrukturellen Materialschädigung (die sich auch aus den Multiskalensimulationen ergibt) auf die Werkstoffeigenschaften des Hüllrohrmaterials werden die strukturmechanischen Materialparameter untersucht und dabei eine deutliche Veränderung am Beispiel der Kenngrößen Streckgrenze und Strahlenwachstum (Dehnung) als Funktion der Dosis und der Betriebstemperatur während Naß- und Trockenlagerung (Zwischenlagerung) festgestellt.

Ein weiterer Aspekt, der mit der Werkstoffschädigung im Zusammenhang steht, sind die Auswirkungen physikalisch-chemische Vorgänge wie Hydridbildung und -ausfällungen, die im Zusammenwirken mit Strahlenschäden die Veränderung der Werkstoffeigenschaften bewirken. Für eine Beurteilung des Bauteilverhaltens bzw. der Integrität der Hüllrohre ist die Fortentwicklung der mikrostrukturellen Schäden in Richtung von Rissinitiierung und -ausbreitung infolge thermomechanischer Spannungen und äußerer mechanischer Beanspruchungen von besonderer

Bedeutung. Dieser Auswirkungen sind Gegenstand anderweitiger bruchmechanischer Untersuchungen auf der Basis der Methode der Kontinuumsmechanik und der Finiten Elemente.

Zusammenfassend lässt sich feststellen, dass mit der Entwicklung und Anwendung eines multiskalen Rechenmodells die Simulation der gesamten Prozesskette der strahleninduzierten Materialschädigung, ausgehend von der atomaren Ebene, realisiert wurde und das Verfahren genaue Kenntnisse über die zeitliche Veränderung der sicherheitsrelevanten strukturmechanischen Eigenschaftsgrößen des bestrahlten Hüllrohrmaterials ermöglicht. Damit wird ein Beitrag zu Beantwortung der Frage der Verlängerung der Zwischenlagerzeiten abgebrannter Brennelemente geliefert.

ABSTRACT

For the high-level waste accumulating in the Federal Republic of Germany, according to the current prognosis spent fuel elements with a heavy metal mass of about 10,500 t, the current concept provides for an interim storage period of up to 40 years. According to current knowledge, however, the permissible storage periods will be exceeded, which requires an extension of the safety demonstration. Within the framework of a research project funded by the BMUV, the present doctoral thesis aims to develop and apply a multiscale method that provides information on the sequence of the multi-stage radiation-induced damage of the cladding tubes of the spent fuel elements and effects on the structural-mechanical properties of the cladding tube.

After the fuel matrix, the cladding tubes of the fuel rods of the fuel assemblies (FAs) are the last barrier against an escape of the radionuclides contained in the fuel. Accordingly, the investigation of the structural integrity of the spent fuel elements is of crucial importance for further safety statements regarding long-term interim storage. Among various damage processes, radiation-induced damage to the cladding tube material and the resulting structural-mechanical effects are of particular importance for the integrity of the FAs. This is a multi-scale process sequence that starts at the atomic level of damage and extends to the macroscopic level with the structural mechanical change of the cladding tube material.

Using the Monte Carlo method, the first step in the hierarchical improved modelling sequence is to determine the effects of the radiation field on the cladding material (Zircalloy-4) of the fuel element. The energy distribution of primary defects for a typical LWR operating phase was obtained with the neutronic damage code SPECTER. Next, the primary defects cascades in the lattice of Zry-4 material were simulated using the molecular dynamics program LAMMPS to determine the spatial distribution, energy spectrum, and density of interstitial atoms and vacancies at the end of the cascade.

Following the end of the cascade, defects interact with each other and diffuse through the multi-crystalline metal lattice, which becomes increasingly damaged. This is done based on the KMC method (Object Kinetic Monte Carlo method), whereby the size and density distribution of defect clusters or microstructures and

their degree of agglomeration are simulated or determined as a function of the irradiation dose. Furthermore, the temporal change of these radiation-induced microstructures is investigated and determined for dry storage temperatures using a cluster-dynamic routine and rate-theoretical algorithms. With a view to testing and validating the overall multiscale model, the results of the model calculations and simulations are compared with those obtained from TEM (transmission electron microscopy) measurements on the distribution and structure of radiation-induced microstructures. This investigation confirms the accuracy of the multiscale method within the range of variation of the experimental measurement data and the results of the individual simulation models.

Due to the effects of the microstructural material damage (which also results from the multi-scale simulations) on the material properties of the cladding tube material, the structural-mechanical material parameters are investigated and a significant change is found using the characteristic parameters yield strength and radiation growth (elongation) as a function of dose and operating temperature during wet and dry storage (intermediate storage) as an example.

Another aspect related to material damage is the impact of physico-chemical processes such as hydride formation and precipitation, which, in combination with radiation damage, cause the material properties to change. For an assessment of the component behaviour or the integrity of the cladding tubes, the further development of the microstructural damage in the direction of crack initiation and propagation as a result of thermomechanical stresses and external mechanical loads is of particular importance. These effects are the subject of other fracture mechanics investigations based on the method of continuum mechanics and finite elements.

In summary, it can be stated that with the development and application of a multiscale computational model, the simulation of the entire process chain of radiation-induced material damage, starting from the atomic level, has been realised and the procedure enables precise knowledge about the temporal change of the safety-relevant structural-mechanical property variables of the irradiated cladding tube material. The evaluation results obtained by this work can fill a critical data gap in studies related to the extension of interim storage periods.

ACKNOWLEDGMENT

This is where I would like to thank all the people without whose cooperation and support this work could not have been accomplished.

It is with gratitude that I would like to thank my supervisor, Prof. Dr. Rahim Nabbi, for his guidance and advice on this PhD work. This work in its present form would not have been possible without many fruitful discussions.

I would like to thank Prof. Dr. Klaus Fischer-Appelt, the best boss I have had so far, for always being supportive and for the friendly atmosphere he provides at the institute.

I would like to thank Prof. Dr. Axel Preuße, who accompanied me in the reviewing of the dissertation and who is as reporter, initiated the completion of this work through his expert opinion.

I would like to thank Dr. Frank Charlier for his support during my entire time at the institute. He approached every obstacle I presented to him in a solution-oriented manner.

In particular, I would like to thank Michael Heyers for his patience in solving all my computer problems.

I would also like to thank my current and former colleagues Hajar El Fatihi, Kurt Diedrich, Christoph Gärtner, Agnes Scaramus, Markus Nolden. I greatly appreciated the insightful professional exchanges, the wonderful cooperation, and the moral support you provided.

I would like to express my appreciation for the support of the sponsor “BMUV: the Federal Ministry of Environment, Nature Conservation and Nuclear Safety and Consumer Protection” under the grant program nuclear safety and waste disposal research.

I would like to acknowledge TUBITAK (The Scientific and Technological Research Council of Türkiye) for the financial support from the 2213-A program.

Finally, I would like to thank my family for their love and unconditional support.

CONTENTS

1 Introduction 1

1.1 Motivation and Research Statement 1

1.2 Organization of the Work 4

2 Details on Literature 7

2.1 Multi-scale Modelling Aspect 7

2.2 Multi-Scale Modelling Techniques For Radiation Effects 9

2.3 Research on Multiscale Simulation of Reactor Materials 11

3 Background 14

3.1 Light Water Reactors 14

3.1.1 Pressurized Water Reactor Power Plant Design 14

3.1.2 Design Of Typical PWR Core and Configuration 16

3.1.3 Fuel Element 17

3.2 Irradiation Effects in LWR Fuel Cladding 21

3.2.1 Effects on Microstructure 21

3.2.2 Effects of Mechanical Behaviour 29

4 Theory of Radiation Damage 34

4.1 Neutron-Nucleus Interaction 36

4.1.1 Elastic Scattering 37

4.1.2 Inelastic Scattering 39

4.2 Displacement Cascades 40

4.3 Microstructural Effect of Radiation Damage 42

4.3.1 Clusters Formation 43

4.3.2 Dislocation Loops 45

5 Mathematical Description of Modelling Radiation Damage 47
5.1 Modeling Techniques 47
5.2 Neutronic Damage Calculations 48
5.3 Molecular Dynamics Method 52
5.3.1 Molecular Dynamics Procedure.....52
5.3.2 . Parameters of MD Simulation 54
5.4 Kinetic Monte Carlo 57
5.4.1 OKMC Simulation Parameters 58
5.5 Rate Theory.....62
6 Numerical Tools and Codes.....65
6.1 Architecture of the Modelling Sequence 65
6.2 Tools and Codes 66
6.2.1 SPECTER 66
6.2.2 LAMMPS 68
6.2.3 OVITO 69
6.2.4 KSOME 70
6.2.5 RT/Scipy 70
7 Method and Parametrization 72
7.1 Radiation in Microstructure Evolution After Operating Condition...72
7.1.1 Neutronic Damage Calculation.....72
7.1.2 MD simulation of Defect Cascades 74
7.1.3 OKMC Simulation of Defect Cluster 77
7.2 Radiation Induced Microstructure Evolution in Storage Phase.....82
7.2.1 Model Description of Defect Evolution.....83
7.2.2 Simplifications for the Storage Case 84
8 Results.....86
8.1 Results of Multiscale Simulations 86

8.1.1 Primary Defects (SPECTER)....86
8.1.2 Defect Cascade (MD)....88
8.1.3 Defect Cluster (KMC)....100
8.2 Results of Rate Theory Modelling....109
8.2.1 Wet Storage (Phase 0)....109
8.2.2 Drying Process (Phase 1)....110
8.2.3 The First 10 Years at Dry Storage (Phase 2)....110
8.2.4 40 Years at Storage (Phase 3)....112
8.2.5 60 Years at Dry Storage (Phase 4)....112

9 Macroscopic Effects of Radiation Induced Microstructures....113

9.1 Method....113
9.1.1 Analytic Model of Hardening....114
9.1.2 Analytic Model of Growth....115
9.2 Results....118
9.2.1 Change in Yield Strength....118
9.2.2 Dimensional Instability....122
9.2.3 Macroscopic Behaviour on Storage Period....126

10 The Effect of Variables....129

10.1 Effect of Temperature....129
10.2 Effect of Alloy Content....131
10.3 Effect of Dose Rate....133

11 Validation of Multiscale Model....140

11.1 Multiscale Simulation of The Experiments: Density and Size Distribution 140
11.2 Macroscopic Deformation Effect....146
11.2.1 Change in Yield Strength....147
11.2.2 Growth Calculation....148

12 Conclusions and Outlook 153

12.1 Summary and Conclusions 153

12.2 Outlook 155

13 References 157

LIST OF FIGURES

Figure 2.1: The multiscale modelling approach applied to radiation effects.....10

Figure 3.1: Schematic of a pressurized water reactor power plant [42] 15

Figure 3.2: PWR core of a KONVOI plant 17

Figure 3.3: Schematic view of the fuel element (courtesy of AREVA NPGmbH), the fuel rod, and its environment 18

Figure 3.4: Structure of hexagonal close-packed (hcp) lattice and main lattice planes 20

Figure 3.5: Edge dislocation [29] (left); <a>- and <c>-loop locations in the hcp lattice (right) 22

Figure 3.6: Left: <a> loops in annealed Zry-2; right: $< c >$loops in recrystallized low-tin Zry-4, irradiated at Research Reactor [57].....26

Figure 3.7: Chemical segregation close to an SPP (center). The BF-STEM image in a) in Zircaloy-2 after neutron irradiation in a BWR to 9.5 x 10^{25} nm^{-2} ~15.8 dpa. Sn, Fe, Cr and Ni maps are shown in c), d), e), f), respectively, and a line scan along the ⟨0001⟩ arrow in a) is shown in b [82].....29

Figure 3.8: Effect of neutron irradiation on the mechanical properties of Zry-4 [96].....30

Figure 3.9: Post-irradiated irradiation hardening data for Zircaloys irradiated at nominally at 358°C compared with the literature results for Zircaloy irradiation at 260–326 °C [72].....31

Figure 3.10: Irradiation growth of Zircaloy-4 as functions of fluence, texture and irradiation temperature $(20 = 3\text{dpa})$ [105]. 33

Figure 4.1: Approximate timescale for the production of defects in irradiated metals (from [106]).....35

Figure 4.2: Mechanisms of irradiation damage in the nuclear reactors by thermal and fast neutrons [109]. 37

Figure 4.3: Energy transfer as a function of center of mass scattering angle([111]) 38

Figure 4.4: a typical neutron spectrum for PWR 40

Figure 4.5: Time evolution of a displacement cascade in Zirconium caused by a PKA with the energy of 15keV. Blue (vacancy), Red(interstitial) 41

Figure 4.6: Different processes in one displacement cascade [126] 42

Figure 4.7: Radiation damage defects creation processes [127] 43

Figure 4.8: Defects in the lattice structure of materials [128] 44

Figure 4.9: Formation energy for various vacancy cluster defects in zirconium as a function of the number of vacancies in the cluster [130] 46

Figure 5.1: Multiscale modeling methods for radiation effects in materials 48

Figure 5.2: MD simulation procedure 53

Figure 6.1: Multiscale modelling sequence 67

Figure 7.1: Determination of PKA spectrum 73

Figure 7.2: (709 groups) average neutron spectrum in the fuel assembly of a PWR 73

Figure 7.3: (100 groups) average neutron spectrum at the core horizontal midplane with Oak Ridge HFIR operating at 85MW 74

Figure 7.4: Determination of defect cascade 75

Figure 7.5: Simulation of defect clusters 77

Figure 7.6: Internal and external events involved in the model 80

Figure 8.1: (100 groups) The normalized PKA spectra for the PWR case 86

Figure 8.2: (100 groups) The normalized PKA spectrums at different irradiation time for the HFIR cases 88

Figure 8.3: Cascade spatial distribution for a 20 keV PKA in Zirconium at 0.78ps. 89

Figure 8.4: Cascade configuration after thermal spike for the cascades at different PKA energies(vacancies and interstitials are presented with green and blue respectively) 91

Figure 8.5: Time evolution of defects formed during displacement cascades 92

Figure 8.6: Stable defect configurations at 573°K in (1) with 12fp for 5 keV PKA, (2) with 38fp for 22keV PKA, (3) with 78 fp for 45 keV PKA and (4) with 112 fp for 65 keV 92

Figure 8.7: Vacancies (in blue) and interstitials (in red) obtained after the cascade relaxation of a 65.7 keV Zr PKA (at 50 ps) using the Wigner-Seitz module: the yellow surfaces represents the cascade overlay using the MD "Construct Surface Mesh" module, the black lines represent the convex-hull of the cascade. 93

Figure 8.8: Stable point defect formation as a function of PKA energy in cascade simulations 97

Figure 8.9: Temperature dependence of stable defect formation in cascade simulations: ratio of simulated point defects to NRT displacements 98

Figure 8.10: Fraction of surviving interstitials relative to the total number of point defects created at different temperatures 99

Figure 8.11: Fractional size distributions of interstitial clusters formed directly within the cascade, comparison of 10 and 50 keV cascades at 630 °K 99

Figure 8.12: Fractional size distributions of vacancy clusters formed directly within the cascade, comparison of 10 and 50 keV cascades at 630 °K 100

Figure 8.13: The spatial distribution of defect clusters at a dose of 7dpa. <a> type vacancy clusters are red spheres, <c> type vacancy clusters are cyan loops and <a> type vacancy clusters are blue loops. 103

Figure 8.14: Total number density of defect clusters versus dpa (fluence) 104

Figure 8.15: Average cluster sizes versus dpa (fluence) 105

Figure 8.16: a: size and density distribution of microstructures, b: configurations (where blue loops are <a> type vacancy clusters and red spheres are <a> type interstitial clusters for the pure Zr model regarding defect type at 1.99dpa 106

Figure 8.17: a: size and density distribution of microstructures, b: configurations (where blue loops are <a> type vacancy clusters and red spheres are <a> type interstitial clusters for the 1.14%Sn-Zr model regarding defect type at 1.99dpa 107

Figure 8.18: Defect Concentration and Sizes on Phase 0. 109

Figure 8.19: Defect Concentration and Sizes on Phase 1. 110

Figure 8.20: Defect Concentration and Sizes on Phase 2 111

Figure 8.21: Defect Concentration and Sizes on Phase 3 111

Figure 8.22: Defect Concentration and Sizes on Phase 4 112

Figure 9.1: Orowan mechanism.....115

Figure 9.2: Left: Schematic showing irradiation growth in Zr. Right: <c> loops form on basal (0001) planes and <a> loops form on {1010} planes.....116

Figure 9.3: Change in Yield Strength with different assumptions 119

Figure 9.4: Ultimate tensile strength and Hardness equivalent of the change in yield strength for the model pure Zr 121

Figure 9.5: Ultimate tensile strength and Hardness equivalent of the change in yield strength for the model 1.14% Sn- Zr 121

Figure 9.6: Point defect equivalents of total cluster densities in (a) for pure Zr model, (b) for 1.14%Sn-Zr model. 123

Figure 9.7: Irradiation growth as a function of fluence for pure Zr model.....125

Figure 9.8: Irradiation growth as a function of fluence for 1.14%Sn-Zr model..126

Figure 9.9: Time Evolution of Yield Strength and Growth Strain During Storage Phases.....128

Figure 10.1: a: Total <a> type vacancy cluster densities, b. average cluster diameters, c. change in yield strength and d. growth strain (axial elongation) of the multiscale simulations at different temperatures as a function of dpa. 131

Figure 10.2: a: Total <a> type vacancy cluster densities, b. average cluster diameters, c. change in yield strength and d. growth strain (axial elongation) of the multiscale simulations with different alloy contents as a function of dpa.....133

Figure 10.3: a: Total <a> type vacancy cluster densities, b. average cluster diameters, c. change in yield strength and d. growth strain (axial elongation) of the multiscale simulations at different dose rates as a function of dpa. ..135

Figure 10.4: a: size and density distribution of microstructures, b: configurations (blue cluster are <a> type vacancy clusters and red spheres are <a> interstitial clusters for the pure Zr model with respect to defect type at dose rate 10^{-6} dpa/s.....137

Figure 10.5: a: size and density distribution of microstructures, b: configurations (blue cluster are <a> type vacancy clusters and red spheres are <a> interstitial clusters for the pure Zr model with respect to defect type at dose rate 10^{-7} dpa/s.....138

Figure 10.6: a: size and density distribution of microstructures, b: configurations (blue cluster are <a> type vacancy clusters and red spheres are <a> interstitial clusters for the pure Zr model with respect to defect type at dose rate 10^{-8} dpa/s. 139

Figure 11.1: TEM image of dislocation loops from alpha-annealed Zircaloy-4 irradiated at nominally 630 °K [72] and the simulated microstructure at same temperature and fluence. 141

Figure 11.2: Microstructure evolution (processed for TEM comparison) in Zr predicted by the OKMC model (lines) for case 1 and case 2. The points are experimental data from [61]. 143

Figure 11.3: Microstructure evolution (processed for TEM comparison) in Zr predicted by the OKMC model (lines) for case 3 and case 4. Error bars are experimental data from [72]. 145

Figure 11.4: Microstructure evolution (processed for TEM comparison) in Zr predicted by the OKMC model (lines) for case 5 and case 6. Error bars are experimental data from [54]. 146

Figure 11.5 a and b: Change of yield strength as a function of fluence for different cases, b. Diagram of measured and calculated change of yield strength. The measured values are taken from Ref. [54,72]. 148

Figure 11.6: Growth elongation as a function of dose for case 1 (573 K) and case 2 (623 K). Red dots (573 K) and green dots (623 K) derived from experimental data in Ref. [92,198]. 151

Figure 11.7: Growth elongation as a function of dose for cases 3, 4, 5, and 6. The red dots and green dots were derived from experimental data in Ref [72] and [54], respectively. 151

LIST OF TABLES

Table 3.1: Standard Composition of Zircaloy-2 and Zircaloy-4 [51].....20
Table 3.2: Main characteristics of <a> dislocation loops observed in zirconium and zircaloy-4 under neutron irradiation 24
Table 3.3: Characteristics of the dislocation loops (c) observed in zirconium and Zircaloy-4 under neutron irradiation.....27
Table 5.1: Expressions of OKMC simulation parameters 60
Table 5.2: Representation of available simulation parameters. The symbols ⊥ and ∥ indicate the directions perpendicular (base plane) and parallel to the direction (c), respectively. 61
Table 5.3: Comparison of reaction rate theory and object kinetic monte carlo methods.....63
Table 7.1: Calculated Lattice Parameters with (EAM) #3 potential.....76
Table 7.2: Kinetic Parameters.....81
Table 7.3: Defect Size and Densities After 2 Years Operation 85
Table 7.4: Parameter List.....85
Table 8.1: Calculated parameters from SPECTER.....87
Table 8.2: Average number of frenkel pairs at different temperatures, maximum values of cascade surface area and volume per PKA energy 94
Table 8.3: The coefficients of the empirical power law formula in hcp-Zr at various temperatures.....96
Table 8.4: Simulation parameters of the test simulation 101
Table 8.5: Simulation parameters used in this study 102
Table 9.1: Employed analytic correlations 118
Table 9.2: Parameters for yield strength calculation 119
Table 9.3: Input parameters of the growth strain calculation 124
Table 9.4: Parameters for yield strength calculation 127
Table 9.5: Average Strain Factors 128
Table 10.1: Simulation parameters.....130
Table 10.2: Simulation parameters.....132
Table 10.3: Simulation parameters.....134
Table 11.1: Simulation parameters.....142
Table 11.2: Simulation parameters.....144
Table 11.3: Simulation parameters.....145
Table 11.4: Parameters for the calculation of the yield strength 147

Table 11.5: Input parameters for the calculation of the growth strain in the pure Zr model 149
Table 11.6: Input parameters for the calculation of the growth strain in the 1.14% Sn-Zr model 150

NOMENCLATURE

ASTM	American Society for Testing and Materials
BCA	Binary Collision Approximation
BWR	Boiled Water Reactor
CNA	Common Neighbor Analysis
DAD	Diffusion Anisotropy Difference
DOE	Department of Energy
EAM	Embedded Atom Methods
ENDF	Evaluated Nuclear Data File
ESK	Entsorgungskommission
GKN	Gemeinschaftskernkraftwerk Neckar
HCP	Hexagonal Close Packed Crystal
HFIR	High Flux Isotope Reactor
HPC	High Performance Computing
IAEA	International Atomic Agency
KMC	Kinetic Monte Carlo
KSOME	Kinetic Simulations of Microstructural Evolution
LAMMPS	Large-scale Atomic/Molecular Massively Parallel Simulator
LWR	Light Water Rector
MCNP	Monte Carlo N-Particle
MD	Molecular Dynamics
MPI	Message Passing Interface
OKMC	Object Kinetic Monte Carlo
OVITO	Open Visualization Tool
PKA	Primary knock-on Atom
PWR	Pressurized Water Reactor
SIA	Self-interstitial atom
TEM	Transmission Electron Microscopy

1 Introduction

1.1 Motivation and Research Statement

The nuclear power industry is ranked fourth in the world in terms of electricity production. Germany's nuclear power plants produced 97,120 billion kWh in 2014, which accounted for 15,8% of the country's overall energy production. Following the amendment to the German atomic energy act (Atomgesetz, AtG) in 2011, eight of the 17 operational nuclear plants had to be shut down. As outlined in the Atomic Energy Act (AtG § 7, para. 1a.), the remaining nine units were scheduled to be shut down until December 31, 2022. A draft amendment to the Atomic Energy Act entered into force on December 9, 2022; allowing the Emsland, Isar 2, and Neckarwestheim 2 plants to operate until 15 April 2023 at latest.

As nuclear reactors are used for energy production as well as scientific and technological research, radioactive waste is created that needs to be monitored, processed, and disposed of in order to minimize its impact on the biosphere. Induced radiation sources, as well as radiological effects, can differ based on the types of materials within the neutron field of a reactor. Nuclear reactors produce high levels of radioactivity as a result of the burning and depletion of the fuel in the core, such as fission products that produce heat, activated uranium and transuranium. In addition, radioactive waste results from the activation of all structures and components exposed to the neutron field of the reactor's core during fission. The different characteristics of the activated materials have led to the classifications of radioactive wastes in Germany as heat-generating wastes and non-heat-generating wastes, which differ - apart from the radiation hazard- in the way they are treated, conditioned, and disposed of [1]. As part of the decommissioning process, highly radioactive nuclear waste in the spent fuel is discharged from the reactor core. However, despite making up only 10% of the volume of radioactive waste, it contributes to 99% of the radioactivity, making it the leading source of hazard [2].

As of December 31, 2013, about 8,216 tons of HM (heavy metal) in the form of irradiated fuel assemblies (FAs) have accumulated from the operation of power reactors and must be directly disposed in the Federal Republic of Germany. In total, it is assumed that about 10,500 tons of HM in the form of irradiated fuel assemblies from the power reactors (including those already accumulated) will accumulate and require final disposal [3].

Konrad is a former iron ore mine, currently being converted into a repository for radioactive waste with negligible heat generation. In terms of radioactive waste volume and inventory, Konrad is limited like any other repository To identify a site for a final disposal facility, in particular for highly radioactive waste, as well as a repository for highly radioactive waste, the Act on the Search and Selection of a Site for a Repository for Heat Generating Radioactive Waste and on the Amendment of Other Laws (Standortauswahlgesetz – StandAG) entered into force on July, 2013. It is expected that the selection procedure for the final repository site will be completed by 2031. This final repository will also store waste with negligible heat generation, such as irradiated fuel assemblies and waste from reprocessing, which cannot be stored in the Konrad repository.

Furthermore, the Site Selection Act specifies that irradiated fuel assemblies must be stored in interim storage facilities until they can be transferred to a repository. The Waste Management Commission (ESK), an advisory body to the Federal Ministry of Environment, Nature Conservation and Nuclear Safety and Consumer Protection (BMUV), regulates the interim storage of irradiated fuel assemblies and heat-generating radioactive waste. The Nuclear Waste Management Commission (ESK) guidelines [4] apply to the storage of spent fuel and heat-generating radioactive waste for a storage period of normally five years of wet storage followed by dry storage in tightly sealed metal canisters at the plant sites. It is stated that "If this period (40 years) is foreseeably not sufficient, suitable additional evidence (e.g., on the long-term behaviour of materials and components of the casks and inventories under storage stress conditions) must be provided." It refers to an extension of the technical basis through.

-physical boundary conditions,

-material behaviour,

-aging effects,

-inaccessible components, such as the fuel cladding tubes.

Within the casks, the cladding tubes serve as the second and final barrier against the leakage of the radionuclides contained within the fuel matrix. Long-term interim storage of spent fuel depends, therefore, on the structural integrity of these structures. As a result of radiation, decay power, and the prevailing internal pressure of the cladding tubes, the fuel rod cladding tubes are continuously subjected to thermal and mechanical stresses during dry interim storage. The safety function of cladding as a structural barrier may result in radiation-induced cladding degradation during whole phases of spent fuel management in this environment. Therefore, in accordance with the BMUV's funding concept, this PhD work concentrates on investigating the effect of radiation damage to the safety and integrity of spent fuel elements with an extended time horizon for interim storage.

With the escalating rise of computer performance, physical models that quantify radiation damage effects on solids have received a major boost. In recent years, using numerical tools in large-scale computer simulations has resulted in a major breakthrough in understanding how pure metals behave under irradiation. This approach, so-called multi-scale modeling or multi-scale simulation, has had rapid success in providing reliable, qualitative and sometimes quantitative predictions [5,6]. As a matter of fact, the use of these models has become so popular that even large utilities and industries are interested in using them to predict the in-service behavior of reactor components. Therefore, within the scope of the present work, knowledge about the sequence of the multi-stage damage mechanisms and thus about the change in the structural-mechanical properties of the cladding tube material of the spent fuel elements are realized by developing and applying a multiscale model.

Under irradiation, damage evolves from atomic to microstructural scales, starting with a primary knock-on atom (PKA) displacement cascade (primary damage), followed by defect clusters. The macroscopic behaviour of materials is necessarily always the result of atomic-level processes. In order to determine the accuracy and rationality of multiscale simulation, physical models must be accurate at each scale, and message communication must be correct between them. Extending the simulation range to all scales, reducing information on transmission between scales,

and understanding how microstructures evolve at the atomic level provides better predictions on material irradiation properties. This is done according to the state of the art in modelling on the basis of hierarchical processes: Monte Carlo (MC) calculations are performed on fuel assembly models using internationally validated databases to determine the atomistic damage rates. To calculate the formation and distribution of defect cascades, molecular dynamic model calculations are performed, considering the recombination behaviour of lattice defects A widely used simulation technique for studying the behaviour of defects in structural materials is the KMC method. The Object Kinetic Monte Carlo (OKMC) method is utilized to simulate the formation and spatial distribution of defect clusters [7]. The simulation sequence is extended to longer time scales. To determine spatial distribution of defect clusters and microstructure formation over longer periods, the rate-theory (RT) method is applied in the last step.

Verifying existing simulation methods is another objective since the damage processes, and mathematical-physical models are complex. This purpose is supported by extensive experimental data. A special focus has been placed on the published measurements from TEM (transmission electron microscopy), which provide data on the size and density distribution of microstructures that have developed.

Another important objective of this work is to assess how the cladding tube material behaves phenomenologically based on the results of radiation-induced microstructure formation. Continuous mechanical methods with structural and mechanical material property parameters are required to study the macroscopic or phenomenological behaviour of the cladding material. Accordingly, the work's final phase involves determining the materials' macroscopic characteristics based on radiation damage in their crystalline structure.

1.2 Organization of the Work

After the introductory chapter, Chapter 2 includes literature view. The essential features of the multi-scale modelling approach and a brief overview of the multi-scale modelling approach is given, as applied to describing the behaviour of structural materials subjected to irradiation.

Chapter 3 is dedicated to description of current knowledge on the scientific and industrial background. First the design and configuration of a LWR reactor core and a fuel element and the structure of Zircaloy as cladding material in terms of microstructure are reviewed then irradiation effects on microstructure and macroscopic behavior of cladding tubes are reviewed. This knowledge was used to determine the most significant phenomena to be considered to simulate irradiation effects in Zircaloy cladding tube.

The theory of radiation damage is discussed in Chapter 4 which is considered starting from theoretical aspects of neutron interaction with matter to irradiation effects with focus on the processes of radiation induce microstructure evolution.

Chapter 5 is devoted to the mathematical description of modelling radiation damage. Within the sequence of multiscale model, methods and implementation procedure of modelling techniques that have been used to describe the radiation damage mechanism in the separate phases are addressed.

Chapter 6 encompasses the description of the numerical tools and computer codes employed for the implementation of the existing work. It focuses on the architecture of the modeling sequence including the numerical methods and the description of codes and models needed for the simulation of radiation induce microstructure evolution.

The application of the simulation method based on the multiscale model is the topic of Chapter 7, in which description of the complete process is divided into two phases as after operating condition and in storage. This chapter encompasses the application of the whole simulation package with the description of the tools and data processing routines Parametrization of codes and implemented algorithms which is the basis for the under-taken multiscale investigation are also presented.

Chapter 8 is devoted to the detailed results of each model applied in the multiscale model sequence. In this respect, the results of each model applied hierarchically are evaluated based on their hierarchy, and a statistical evaluation of the obtained results is provided.

Chapter 9 discusses how radiation-induced microstructure obtained with the multiscale model is evaluated macroscopically. An analysis of the correlation

between the studied phenomena and the methodology used is presented as well as its parametrization. The radiation-induced changes in the microstructure are evaluated in terms of yield strength and dimensional instability.

Chapter 10 focuses on quality of simulations. This can be done by measuring sensitivity to input parameters. In this section, the multiscale model is considered in terms of sensitivity to temperature, dose rate and alloy content and effect of these parameters is evaluated.

The validation of the multiscale model is the subject matter of Chapter 11. First, characterization data collected from experimental studies are presented and a general observation of the radiation-induced microstructures of zirconium and its alloys under neutron irradiation is presented. In terms of model validation of the entire simulation model, a comparison of the experimentally parametrized simulations with the measured results of the experimental works is undertaken.

Finally, the existing work is completed in Chapter 12, summary, and conclusions; and the capability of the developed model is also provided in Outlook.

2 Details on Literature

2.1 Multi-scale Modelling Aspect

There are several challenges involved in defining multi-scale modelling, including philosophical ones. In order to understand the fundamental mechanisms governing the behaviour of a physical system, modelling requires identifying and quantifying the variables and parameters that influence and determine it, so that a suitable physical model can be derived.

In order to identify and quantify mechanisms, different phases are involved, and hence, different modelling approaches are feasible. There are three main types of approach: empirical, mechanistic, and physical. Based on experimental data, purely empirical approaches involve interpreting variables of practical interest, such as neutron flux, as functions of macroscopic properties in an experimental database. Even without knowing the underlying mechanisms, simplified analytical expressions can usually describe the correlation [8]. It is possible to discuss a mechanistic approach if this approach is coupled with a series of microstructural studies [9,10], so as to determine the possible origins of certain macroscopic behaviours based on what is observed on a microscopic level. Models resulting from this process are still oversimplified, but the chemical composition or other features of a material may allow certain contributions to be included or excluded. Currently, this approach is being used in the nuclear industry, and it is widely accepted by regulators. As an example, empirical correlations have been constructed for RPV steels with terms explicitly related to, for example, copper-rich precipitates (dependent on Ni content), matrix damage accumulation (voids, loops, etc.) and phosphorus segregation at grain boundaries which form the foundation for integrity evaluation [11,12].

The purpose of a physical approach is to explain how microstructural features are created, and how they influence material behavior, based on precise physical mechanisms. In order to make accurate physical models that are capable of

predicting outcomes, all the important mechanisms must be identified, together with the variables that influence them. The purpose of computer simulations, in this context, is to identify and quantify mechanisms through virtual experiments. In this respect, computer simulations are on an equal footing with real experiments, provided that they also aim to identify and quantify mechanisms (modeling-oriented experiments), rather than merely provide engineering values. This section focuses on the physical approach.

Throughout the next sections, we will see that computer experiments (physical models) serve primarily two purposes: (i) for assessing quantities, or to study phenomena that cannot be studied by real experiments; and (ii) for determining whether possible physical mechanisms explain the results of real experiments. Models at the atomic level, such as density functional theory calculations and energy minimization techniques, molecular dynamics (MD) simulations, and Monte Carlo methods, are included in the first type of computer experiment. For the latter, interatomic potentials are generally used to describe interatomic forces.

Atomic-level modeling is problematic in terms of experimental validation. There are many phenomena whose existence and features can only be determined by computer simulations (such as displacement cascades), which cannot be directly validated by experiments. It is implicit that in this case the model has not been developed to be compared with experiments. Rather than relying on experimentation, it is grounded in well-established physics (e.g., quantum or classical mechanics), and is used to understand phenomena not directly observable in reality. As these models are based on established physics, experimental validation has already been performed. In practice, validation of these models must be done in direct or indirect ways, though it is not always an easy task.

Mesoscopic models, such as kinetic Monte Carlo, rate theory, and dislocation dynamics, comprise the second class. The capability of computers to manage a large number of variables is exploited here to identify the important mechanisms by comparing the results of the models with experimental results. This allows us to differentiate between mechanisms and parameters that are supposed to drive the evolution of a system. Following identification of the key mechanisms and parameters, these models can be used to discover laws or correlations that exist in situations where experimental data are not available.

This physical approach might be able to describe reliably the process by which radiation damage is produced, evolves, and subsequently leads to material degradation on all relevant time and length scales if computer simulation techniques capable of modeling radiation effects at all different scales are properly developed, parameterised, and coupled. While applying physical methods exploiting multi-scale simulation techniques can be useful independently, regardless of whether a fully integrated multi-scale model is achieved, it must be emphasized that a physical approach can be useful independently.

An approach to multi-scale modelling can be summarized in one sentence, as "the construction of a physical model that describes phenomena occurring at a specific scale and in accordance with known physical mechanisms by harmonising the application of different, dedicated computer simulation tools [13].

But it goes beyond that to look at problems from the right scale and location in order to find the source of a certain phenomenon. This is therefore a powerful approach to use in conjunction with other approaches and experiments to explain, and possibly predict, the behaviour of materials (under irradiation in the case at hand).

2.2 Multi-Scale Modelling Techniques For Radiation Effects

Radiation damage can be described using different theoretical frameworks and computer simulation tools, from the atomic to the meso/macroscopic scale. Below is a brief review of the most important ones.

A multi-scale approach to radiation effects in metals involves the transfer of ab initio data into interatomic potentials, which are then used to perform large-scale molecular dynamics simulations and Monte Carlo simulations of the production and short-term evolution of radiation damage. Using this information, long-term mesoscopic models of microstructural and microchemical evolution can be developed, based on kinetic Monte Carlo or rate theory approaches, and then dislocation dynamics can be used to explain the plastic behavior of a single crystal. To build the link to macroscale models, microstructural/microchemical evolution models and dislocation dynamics models must be combined to formulate physics-based constitutive laws.

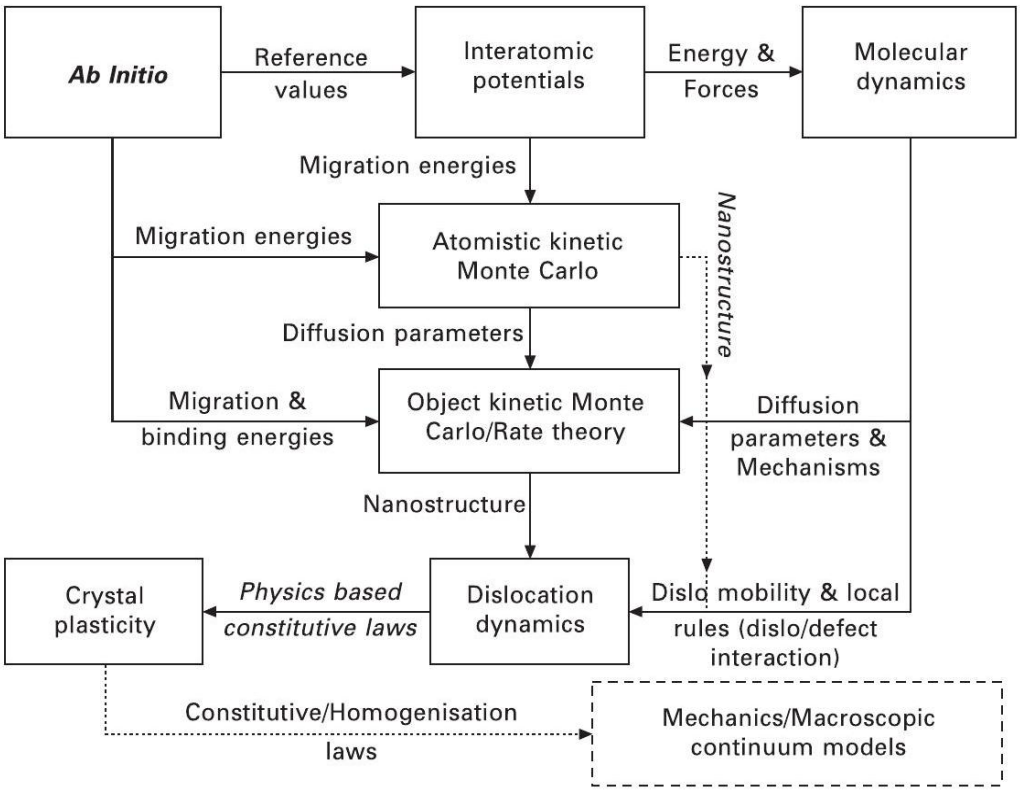

Figure 2.1: The multiscale modelling approach applied to radiation effects

Multi-scale modelling techniques are presented here under five headings based on this broad scheme (see Fig. 2.1): nuclear interactions, atomic-level interactions, atomic-level modeling, microstructure evolution modelling, and mechanical property modelling. Ab initio data is converted to interatomic potentials for use in large-scale molecular dynamics and Monte Carlo simulations of radiation damage and its short-term evolution. In order to describe the material plastic behavior at the level of single crystals, this information is applied to the long-term mesoscopic models of microstructural and microchemical evolution (kinetic Monte Carlo or rate theory). The combination of predictions from the two latter mesoscopic tools should provide input for formulating physics-based constitutive laws that are an essential part of continuum models [14]. All of these classifications are equally valid but are also debatable simultaneously.

Crystal plasticity models, which are often based on finite element techniques, are also not reviewed. Crystal plasticity is indeed modelled at multiple scales e.g. [15–

17]. It is noteworthy, however, that multi-scale is interpreted differently in plasticity than it is in the current context. Microstructure refers to grain size, shape, and phase distribution in plasticity applications. A plasticity model considers this scale to be the lowest. Multi-scale plasticity models, therefore, take grain information explicitly into account. In plasticity, an individual crystal is recognized as a single crystal, a group of grains is recognized as an aggregate, a representative volume element is recognized as an RVE[1], and finally an actual component is recognized. However, in radiation damage problems, the fundamental scale is the atomic scale, and what has been referred to as microstructure here corresponds to what has been referred to as substructure in plasticity, namely defects and precipitates within grains, which are generally not explicitly included in crystal plasticity models. Radiation damage physical multi-scale models have so far focused on investigating microstructure evolution in a reference volume where grain boundaries serve primarily as sinks. A single grain or crystal is modelled in this framework. A number of popular and recent reviews devoted to the field make this evident [18–23]. Thus, up to now, multi-scale modeling of radiation damage essentially ended at crystal plasticity. If a link between the two approaches could be established, and this is the ultimate goal of all multi-scale modelling programmes on radiation damage.

2.3 Research on Multiscale Simulation of Reactor Materials

There have been several studies on reactor structural materials using multiscale simulations in recent years, both in existing reactors and next-generation reactors. The majority of these studies are from Europe, the USA, and China, and some have developed multiscale simulation software for RPV steel research.

DOE has led the Consortium for Advanced Simulation of Light Water Reactors (CASL) project, which has developed the Materials Performance and Optimization (MPO) module to study fuel–cladding interactions and cladding corrosion. In addition, continuum models of material physics are provided in the Virtual Environment for Reactor Applications (VERA) [24,25]. Microscale simulations are used in the MPO module to explain the mechanisms of complex degradation of key topics, such as pellet-clad interaction (PCI), grid-to-rod fretting (GTRF), and CRUD (Corrosion Residual Unidentified Deposit). A 3D, high-resolution

1: The RVE represents the smallest statistically representative unit of material and contains all microstructural information at the origin of its mechanical behaviour, along with radiation damage, if present.

multiphysics coupling simulation environment is being developed to apply continuous fuel/cladding/corrosion models available at the engineering scale.

The European Union (EU) has developed virtual test reactors (VTRs) specifically to study material properties in service, which started in the framework of the Reactor for Virtual Experiments (REVE) project [26,27]. Nuclear safety and service life are assessed using VTRs. Through integrated multiscale simulation programs, it is possible to simulate degradation in performance and failure behavior under adverse operating conditions for critical materials. REVE has already assisted with the construction of the first VTR, known as RPV-1 [28,29]. RPV-1 simulates the irradiation embrittlement of RPV steels in PWRs and BWRs.

It can assess the change in RPV steel's microstructure and yield strength during irradiation. In the context of the PERFECT project supported by the European Commission, RPV-1 provided results that were in accordance with experimental results and led to RPV-2 being developed [29,30]. On the basis of RPV-1, RPV-2 investigated the impact of defects caused by RPV materials under different neutron irradiation conditions on their critical tangential stresses (neutron spectrum, neutron flux, temperature, etc.). RPV-1 and RPV-2 contain modules that simulate irradiation-induced defect clusters at atomic scale, including the MD program DYMOKA [31], the annealing evolution simulation program LAKIMOCA [32], the defect evolution simulation program MFVISC36 based on RT, as well as a thermodynamics theory-based defect cluster simulation program DIFFG [33,34]. Furthermore, the EU launched the 4-year project PERFORM 60 (2009-2013) under PERFECT's roadmap [35,36]. In addition, it developed multiscale simulation and modeling tools for analyzing the effects of irradiation on material microstructure, fracture behavior, and SCC (Stress Corrosion Cracking) [35].

GETMAT, the seventh Euratom Framework Programme, was launched in 2007 by the European Commission [37].The objective of this project was to qualify commercially available materials and develop new materials, and to select oxide dispersion strengthened (ODS) alloys and 9-12 Cr F/M steels as reference materials. Multiscale simulations and experiments were conducted to understand how these materials react to irradiation. For the study of irradiation-induced hardening and embrittlement in Fe-Cr alloys, a compact multiscale model was developed utilizing the ab initio method, MD, the atomic KMC (AKMC), the OKMC method, CD, and dislocation dynamics (DD) [38]. According to GETMAT's research, the Joint

Programme on Nuclear Materials (JPNM) was launched by the European Energy Research Alliance (EERA) in 2010 to develop and research materials essential for fast reactor development and implementation [39].

F/M steels are frequently used as structural materials because they are more resistant to radiation swelling than austenitic steels. As a result of irradiation, F/M steels are limited in terms of their operating temperature range. A project titled Multiscale Modeling for Fusion and Fission Materials (M4F) was launched by the European Union in 2017 to investigate the deformation mechanism of F/M steels under irradiation. Through the use of a physical-based multiscale modeling approach, the project analyzes and predicts hardening induced by neutron irradiation in F/M steels [40]. Currently, most of the research on radiation effects of nuclear materials takes place on an atomic and micro-nano scale. Multiscale simulations coupled with HPC technology play a significant role in computer simulation.

3 Background

3.1 Light Water Reactors

A Light Water Reactor uses light water as the coolant, the moderator, and often as the reflector material. These are typical thermal reactors, which cause nuclear fission reactions of the U^{235} atoms by utilizing thermalized neutrons. LWRs can be classified into two main types: PWRs and BWRs. As a result of differing approaches to generating steam (high quality steam should not contain more than condensed water), these two types were created. The capacity of LWRs has been routinely considered in their design. Due to earlier notions that pressurized liquid water would somehow be safer to handle than steam in the reactor core and would contribute to the core's stability during operation, pressured water reactors were designed and implemented commercially much earlier than BWRs.

3.1.1 Pressurized Water Reactor Power Plant Design

A schematic of a PWR power plant is shown in Figure 3.1. PWR plants contain two water loops, primary and secondary. Inside a ferritic steel reactor pressure vessel (RPV), where the core of a PWR is located. Internally, the reactor shell (typical dimensions: outside diameter ~ 5 m, height ~ 12 m, and wall thickness 30 cm) is lined with reactor cladding of stainless steel 308 or Inconel 617 that provides adequate corrosion resistance against coolant when in contact with the RPV. Steam is formed by transferring the heat from the primary loop water to the secondary loop system. Essentially, a steam generator is a heat exchanger with stainless steel plates (supporting thousands of nickel-based tubes (Incoloy 800) or nickel-based superalloys (e.g., Inconel 600). A PWR core consists of an array of fuel elements with stacks of fuel pellets that are slightly enriched$(2.5 - 4\%)UO_2$ [41].Various reactor designs may differ in terms of the above-mentioned dimensions.

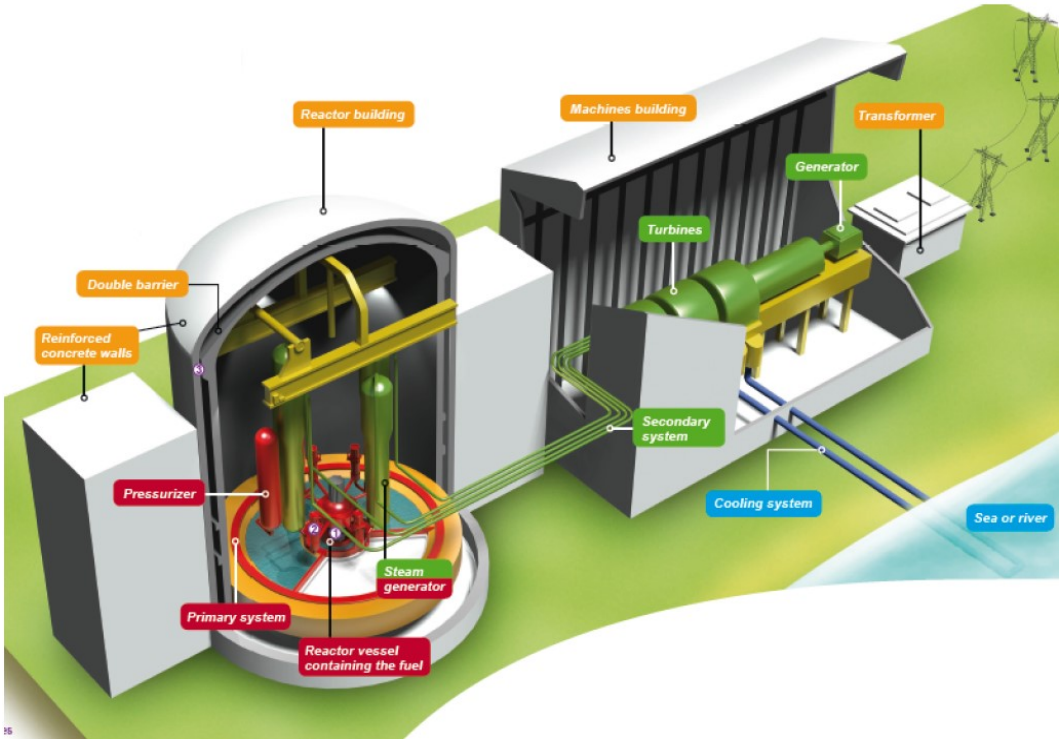

Figure 3.1: Schematic of a pressurized water reactor power plant [42]

Keeping the cooling water from boiling is accomplished by maintaining a pressure of 150 bar in the pressurizer for Isar 2 as a typical German Konvoi plant. As it is pumped from the bottom of the pressure vessel to the top via four primary pumps (see Fig. 2.1), it is heated to a typical temperature of 328° C at the outlet [43]. Coolant temperatures cause fuel cladding outer temperatures to range between 300° C and 330° C. In the pressure vessel outlet, heated water is fed into four steam generators, where heat exchangers between the primary and secondary cooling circuits evaporate the secondary cooling water: the primary cooling water is then reinjected into the pressure vessel. In the secondary circuit, steam is created and directed to one high pressure (HP) turbine with a vapor pressure of 64 bar at its inlet and 11 bar at its outlet; it is then directed to two low pressure turbines, followed by a condenser, where it is repumped into the steam generators. Cooling towers provide the heat sink for the condenser; rivers and the sea could also be used as heat sinks. Turbines with a rotation speed of 1500 r/min drive a generator, producing 1410MWe of net electrical power [43].

A boiling water reactor is designed with a direct cycle cooling system, which means there is only one loop of water, and therefore there is no steam generator. A BWR reactor core is positioned near the bottom of the pressure vessel which is more or less similar to the PWR RPV. The core of the BWR is composed of fuel assemblies with slightly enriched UO_2 fuels [41].

3.1.2 Design Of Typical PWR Core and Configuration

The core is located inside a vessel made of low-carbon steel fitted with an upper head that is removed for refueling purposes (Figure 3.2). Inside the vessel are metal structures (known as internals) that can be completely removed to facilitate periodic inspections:

– the lower structures support the core;

– the side structures (core barrel) separate the cold fluid entering the vessel from the hot fluid exiting the core;

– the upper structures are made up of control rod guide tubes.

The German 4-Loop PWR Neckarwestheim (GKN II) type KONVOI core consists of 193 fuel elements where each fuel element represents a group of around 300 fuel rods (pin arrangement 18×18−24) that are located one close to another [44].

After every refueling cycle, about one fourth of the fuel assemblies are exchanged with new assemblies; German nuclear power plants have one-year refueling cycles, while US or French plants prefer 18-24 months cycles. PWR fuel assembly lifetimes are in the range of five one-year cycles, corresponding to FA end-of-life burnups of 55-60MWd/kgU in typical German PWRs [45]. In refueling, the core is completely removed and reloaded, with a new arrangement of its assemblies; loading patterns are determined based on neutronics calculations of assembly burnup and power levels in order to ensure a uniform power level throughout the entire core. As a result of economic reasons and to reduce the probability of neutron damage to the reactor pressure vessel, a low leakage core loading pattern with high burnup fuel elements is being used.

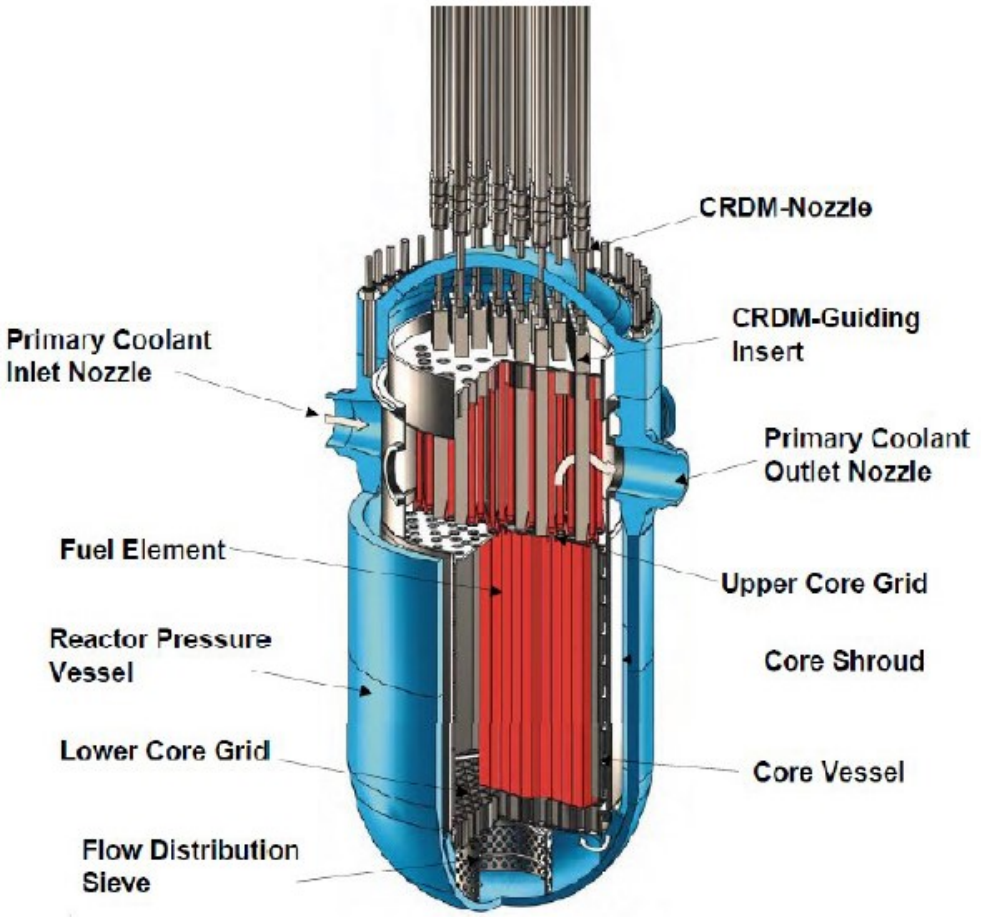

Figure 3.2: PWR core of a KONVOI plant

3.1.3 Fuel Element

The reactor core consists of several fuel assemblies arranged as follows:

The structure holds the fuel elements; the coolant receives the desired thermal power; and the fuel elements receive heat; highly neutron-leak-proof critical assembly provide sufficient coolant volume and flow to remove fission heat from neutrons during fission; the control rods adjust for fuel consumption, so that criticality can be maintained [46].

German Vorkonvoi and Konvoi designs host fuel element with an active length of 3,9m in the PWR core. In Figure 3.3, a schematic illustration of a typical PWR fuel element is provided. Assemblies consist of top and bottom pieces connected by

around 20 - 24 guide tubes, which together with spacer grids located approximately every 500mm other axial position form the assembly skeleton. Spacer grids are composed of 14 x 14 to 18 x 18 square grids; those positions that are not occupied by guide tubes are occupied by fuel rods, which are held by spacer springs and have no fixed connection to the top or bottom end pieces. A fuel rod or fuel pin is a fuel cladding tube stacked with fuel pellets that are slightly enriched on the inside and sealed from the outside. At about 20 bar pressure, free volume the fuel clad is filled with He gas to hold the pellets at their position. Plenum springs lie inside the top of each fuel rod to hold the pellets in place. Using cooling water as a moderator, pellets produce heat by thermal fission of $^{233}_{92}U$, $^{235}_{92}U$, $^{239}_{94}Pu$ and $^{241}_{94}Pu$. Individual cladding tubes are generally made from Zircaloy-4 alloy (the new alloy is Zirlo or M5), and measure about 10 mm in diameter and 0.7 mm in thickness [41].

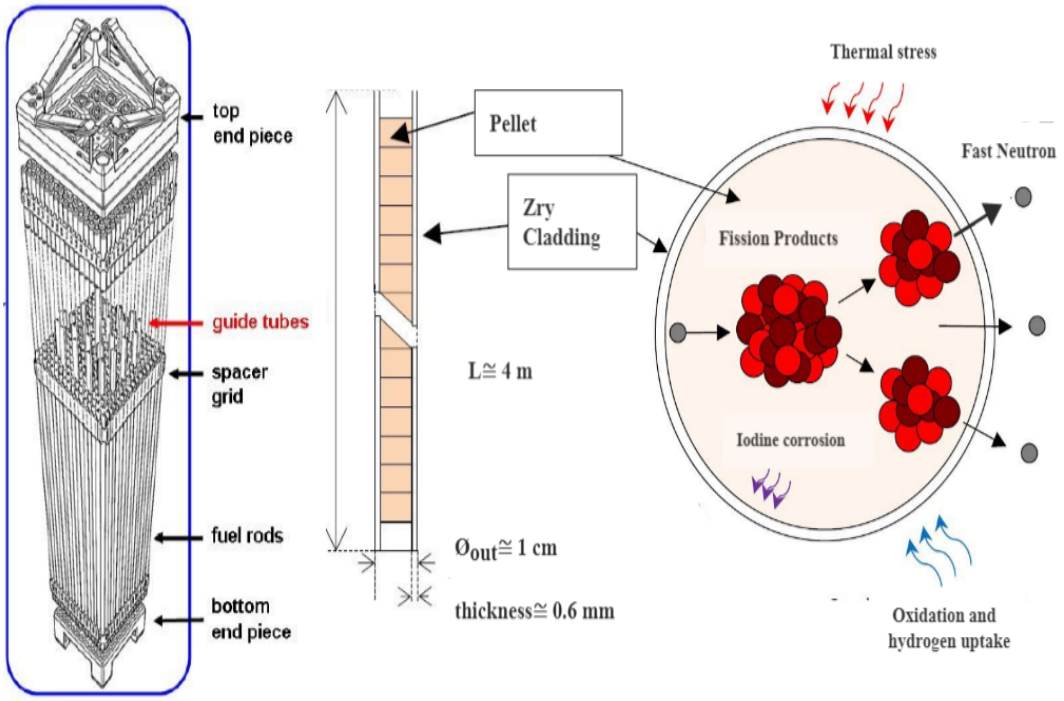

Figure 3.3: Schematic view of the fuel element (courtesy of AREVA **NPGmbH**), the fuel rod, and its environment

In LWRs, the fuel cladding is an essential primary structural component, serving as the first engineering barrier against the release of fission products during irradiation and into the environment during post-irradiation handling and transport of the fuel

assemblies. The fuel clad tube is a thin, long, hollow seamless tube. Inert gas and <5wt% enriched uranium dioxide fuel pellets are filled into the cladding tube, which is sealed by welding plugs on both ends. This combined metal and ceramic component are referred to as a fuel rod. During operation of a reactor, the cladding is subjected to an aggressive environment that includes thermo-mechanical stresses, neutron irradiation, aqueous oxidation and hydrogen uptake on the outer layer, and the risk of iodine stress corrosion on the internal side as seen in Figure 3.3 (right).

3.1.3.1 Zircaloy fuel cladding

Zirconium alloys (Zr alloys) are used as fuel cladding (FC) and core internals in light water reactors (LWRs) because of their low neutron absorption cross section, good corrosion resistance in service, reasonable mechanical strength and dimensional stability under high temperature and irradiation.

The group of Zr-Sn-Fe-Cr alloys contains the so-called Zircaloys (Zrys) with the two main groups Zry-2 and Zry-4. Zr-based alloys with the main alloying elements Sn, Fe and Cr, which mainly differ in their Ni content, have been used for nuclear applications for decades [47]. Zry-4 is currently used in both PWR and BWR, while Zry-2 is just a BWR material. The chemical composition of the Zry-4 and Zry-2 is given in Table 3.1. Although Zircaloy-4 is still used in some PWRs, it is being replaced as fuel discharge burnups have increased and PWR ratings have increased. The advanced PWR cladding alloys are Nb containing alloys: ZIRLO, Optimized ZIRLO and M5 [48]. In BWRs, the cladding has remained essentially Zircaloy-2 (with Zr-Sn-Fe-Cr-Ni). The advanced BWR cladding alloys currently being implemented are Zircaloy-2 with higher iron contents.

Zirconium and Zr-based alloys are in the Zr`s α-phase at room temperature and at typical operating temperatures of the components in the stack of 300° C - 400 °C for claddings. Zr`s α-phase is hcp with space group 6/mmm; the atomic position sequence for hcp is ABABAB... Pure Zr has lattice parameters of a=3.231 and c=5.147 and a density of 6.5 g/cm^3 [49,50]. The lattice parameters shift slightly with alloy content.

Table 3.1: Standard Composition of Zircaloy-2 and Zircaloy-4 [51]

Alloy / Element	**Zircaloy-2 wt %**	**Zircaloy-4 wt %**
Tin	1.20 – 1.70	1.20 – 1.70
Iron	0.07 – 0.20	0.18 – 0.24
Chromium	0.05 – 0.15	0.07 – 0.13
Nickel	0.03 – 0.08	-
Fe + Cr + Ni	0.18 – 0.38	-
Fe + Cr	0.28 – 0.37	-
Oxygen	0.09 – 0.16	0.09 – 0.1
Silicon	0.005 – 0.012	0.006 - 0.012

Fig. 3.4 shows a schematic representation of the hcp lattice structure with the notation of the lattice planes that are most important for irradiation defect accumulation. The basal planes are perpendicular to the basal pole (0001); the prism planes can be divided into two different types, type I $(\bar{1}100)$ and type II $(11\bar{2}0)$ accumulation [52]. The transition from hcp α -Zr to body-centered cubic (bcc) β-Zr occurs for very pure Zr at 862° C; the β- phase has a lattice parameter of 3.545 Å [49]. However, the high temperature phase is not present during normal reactor operation where all Zr-based structures are in the α-phase.

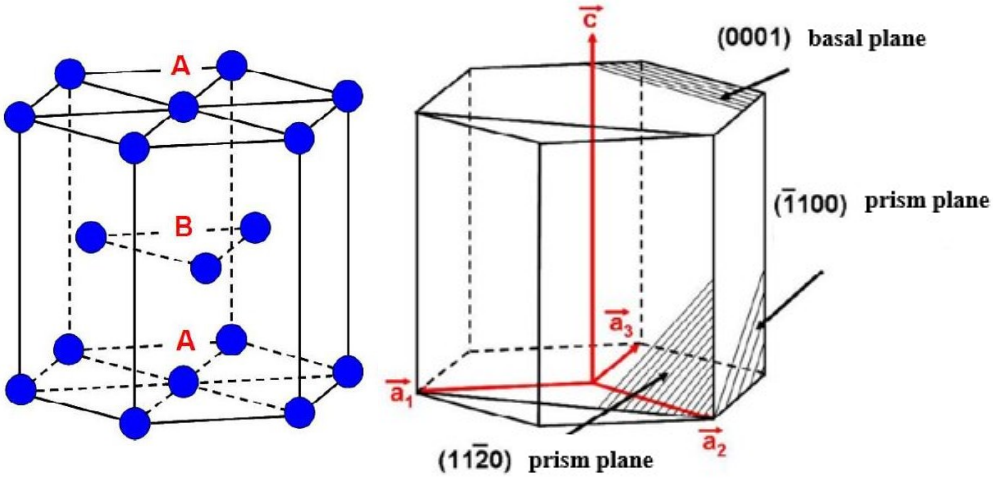

Figure 3.4: Structure of hexagonal close-packed (hcp) lattice and main lattice planes

3.2 Irradiation Effects in LWR Fuel Cladding

3.2.1 Effects on Microstructure

A neutron bombardment of Zr-alloys produces atomic defects in their crystal structures. Zirconium atoms in the HCP crystal lattice are knocked out of equilibrium by the energetic neutrons. Therefore, crystal structures are filled with vacancies and interstitials.

Dislocation loops have been observed on prism planes and basal planes of Zr-based alloys as a result of radiation damage. Loops are either condensed on a basal plane or on a prism plane. During the diffusion of point defects to different sinks, loops are formed in an anisotropic way. Burger's vector of the loop boundary dislocations identifies the loops. In order to describe loops condensing on the prism plane, the a> loops are used, while the c> loops are used when forming on the basal plane. It is common to form a dislocation loop when there are a large number of vacancies or interstitials agglomerating on a plane; the vacancies or interstitials form a disc whose boundary is a circular edge dislocation [30]. The left image in Fig. 3.5 shows a schematic of an edge dislocation. Cutting a crystal along the plane ABCD as shown in Fig. 3.5 can create an edge dislocation. The left upper part of the crystal is then shifted to the right by distance b, while the right upper part of the crystal remains unchanged. Once the strain is released, the upper halves of the crystal will be combined again. Line CD is referred to as a dislocation line.

Many studies have been conducted on the irradiation-induced damage of Zircaloy cladding tubes (e.g. [53–56]). It was demonstrated that neutron irradiation could induce the formation of two distinct types of dislocation loops:

_ a-type (loops that lie in the prismatic plane (1 0 1 0)),

_ c-type (loops that lie in the basal plane (0 0 0 1)).

Depending on the conditions (temperature and fluence), parameters such as dislocation size and density tend to be proportional or inversely proportional [55–57]. However, the loops of an a-dislocation also exhibit some common characteristics in that their Burgers vectors are parallel to the a-axis and tend to be located on prismatic planes.

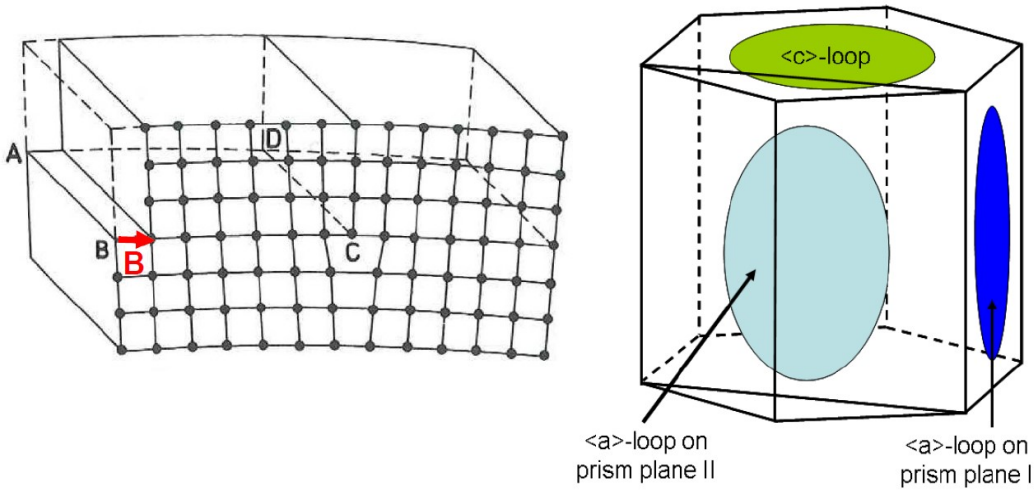

Figure 3.5: Edge dislocation [29] (left); <a>- and <c>-loop locations in the hcp lattice (right)

During and after irradiation, a-loops(see Fig 3.6) are present in the material, but c-loops appear only at high fluences (>4 x 10^{25} neutrons/m^2 at 533° K) [55,58,59]. Several other authors have confirmed that a-loops nucleate since the beginning of irradiation and are both vacancy- and interstitial-type structures, while c-loops form only above a threshold dose and are vacancy structures [60–63].

The lack of experimental techniques to observe the c-type dislocation loop resulted in the absence of experimental evidence of the existence of c-type dislocation loops during the early stages of the nuclear industry. In 1975, Bell and Adamson identified the <c> loop by using what Bell termed the corduroy structure [64]. As Idrees et al. demonstrate [65], alloying elements and stress gradients influence the loop nucleation. It is likely that the appearance of defects in the <c> component coincides with the reported onset of accelerated growth, suggesting that these defects may have a significant influence on the growth process (which can be viewed in 2.2.2.2). Furthermore, thermal annealing (at intermediate temperatures above the irradiation temperature) of pre-breakaway samples restores the dimensions of the pristine material in contrast to post-breakaway samples that cannot recover their original dimensions under the same thermal treatment [59]. According to Holt [66], this indicates a persistence of relatively stable defects associated with breakaway growth. This finding is consistent with the observation

that the vacancy c>-component loops associated with breakaway growth are present after 1 h of post-irradiation annealing at 600 °C [66,67].

3.2.1.1 Characterization of <a> loops

Griffiths [68] has proposed one of the most detailed compilations of experimental results on irradiation effects in zirconium and its alloys. The main point defect cluster observed by transmission electron microscopy in low fluence irradiated zirconium alloys is the dislocation loop which has a Burgers vector $\langle a \rangle = 1/3\langle 11\bar{2}0 \rangle$. This planar defect is called a "<a> loop" or even a "prismatic loop" because the plane of the loop is parallel or close to the prismatic plane of the compact hexagonal structure, i.e., the $\{10\bar{1}0\}$ family. Observations show that the occurrence of <a> loops occur very rapidly upon irradiation. The nature of the loops (interstitial or vacancy), their density and diameter depend on several parameters such as the fluence, the irradiation temperature or the presence of alloying elements.

A dislocation loop can be determined experimentally based on its geometry, Burger's vector, size, and proportion of vacancy and SIA loops. Experimental results showed that all <a> loops have the same Burgers vector $\vec{b} = 1/3 <1\ 1\ 2\ 0>$ and the same habit plain on $(1\ 0\ \bar{1}0)$ [61,69].

The research conducted by Northwood et al. [60,70,71], which pioneered research on the radiation damage in zircaloy-2, also examined zirconium metals. Based on these findings, zircaloy-2 displays dislocation characteristics similar to zirconium metal, in that both vacancy and SIA dislocation loops have Burgers vectors located in prismatic planes. Vacancy loop geometry shows a circular shape with loop size less than 40 nm, but an elliptical shape with loop size greater than 40 nm. In most interstitial cases, regardless of temperature, the shape tends to be circular [59].

The results compiled in Table 3.2 show the following trends:

i. At fixed fluence Ψ, the average size $\bar{d}$ of the loops increases with the irradiation temperature This temperature effect has been highlighted by different authors [55,60,72] and can be explained by the increase of the mobility of the defects with the irradiation temperature which leads to a larger average free path of the point defects. These can then annihilate the loops present in the material.

Table 3.2: Main characteristics of <a> dislocation loops observed in zirconium and zircaloy-4 under neutron irradiation

Ref.	Plane	$\vec{b}$	$\| \vec{b} \|$ (Å)	Type
[68]	$\{11\bar{2}0\}$	$1/3\langle 11\bar{2}0\rangle$	$a = 3.23$	Interstitial or Vacancy
	$\{10\bar{1}0\}$	$1/3\langle 11\bar{2}0\rangle$	$a = 3.23$	Interstitial or Vacancy

Ref.	Material	$T_{Irr.}$ (°K)	$\Psi(\mathrm{p.m^{-2}})$	$\bar{d}$(nm)	$\bar{\rho}(\mathrm{m^{-3}})$
[61]	Zircaloy Zone refined	708	6.4×10^{23}	-	$<0.1 \times 10^{20}$
		668	3.3×10^{23}	33	7×10^{20}
		668	6.4×10^{23}	56	2×10^{20}
		623	2×10^{23}	<10	8×10^{20}
		623	5.3×10^{23}	23	27×10^{20}
		573	3.8×10^{23}	9	120×10^{20}
[73]	Zircaloy-4 Alpha-annealed	630	5.5×10^{24}	11.3	1.89×10^{21}
		630	2.93×10^{25}	9.6	3.42×10^{21}
[54]		673	8.1×10^{24}	3.9	1.63×10^{22}
		673	3×10^{25}	4.5	1.09×10^{22}

ii. At a fixed fluence, the density of loops decreases with the increase of the irradiation temperature. The increase in the mobility of defects would favor their annihilation and thus lead to a decrease in the number of loop germination sites.

iii. At fixed irradiation temperature, the average diameter $\bar{d}$ of the loops increases with fluence This is typically a growth effect of the loops which all else being equal receive more defects over time when more defects are created.

v. Impurities can act as traps for point defects, preventing them from diffusing and favoring the germination of small clusters. Generally speaking, as the number of traps increases, the mobility of defects decreases, thus limiting the growth of loops and promoting sprouting.

vi. The density of the loops increases with the number of alloying elements. This observation is related to the previous one.

3.2.1.2 Characterization of <c> loops

< c > component loops, containing a stacking fault and invariably vacancy type in nature [58,68,74]. No matter which dilutes alloy is considered, <c > component loops are only formed at levels that are substantially higher than those required for < a > loops. The <c> loops are lying in the (0 0 0 1) plane, and the Burgers vector is either 1/2 <0 0 0 1> > or 1/6 <2 0 $\bar{2}\bar{3}$> as it follows the c-axis.

The ⟨c⟩ loops began to be observed for high irradiation doses, typically above 3.0×10^{25} n·m^{-2}. The work of Northwood [60] did not reveal such loops, probably due to too low an irradiation dose (1.0×10^{25} n·m^{-2}). The work of Griffiths and Holt [55,68,75] notice this type of loops at irradiation doses higher than 5.0×10^{25} n·m^{-2}. They are mainly localized in the baseline plane with a Burgers vector $\langle c\rangle=1/6\langle 202\bar{3}\rangle$ that has a component following the c-axis $\vec{}$. These loops are distributed in layers parallel to the ground plane, they will be referred to hereafter as ⟨c⟩ loops.

According to Holt and Gilbert [63], high fluence (8.6 x 10^{25} n/m^2) revealed the behavior of dislocation loops between 553 and 584 °K. In contrast, Zircaloy-2 and Zircaloy-4 exposed to fluences below 3.0 x 10^{25} n/m^2 show only type <a> dislocation and not <c> type of loop. For specimens exposed to more than 3.0 x 10^{25} n/m^2, however, <c> loops were observed. In that research, <c> loops show another special characteristic: dislocations in those components appear to be associated with particles in the second phase.

A review of microstructure evolution in zirconium and its alloys is provided by Griffiths [55,56], along with the characteristics and effective parameters of the "c" type of dislocation. As well, Griffiths investigated neutron irradiation damage in zirconium and Zircaloy-2 and -4 in EBR-II (Experimental Breeder Reactor II) at a

temperature range of 644 to 710 °K and a fast neutron flux of 6 x 10^{22} n/m^2 [68]. It is observed that the <c> component loops are much larger than the <a> loops, but their density is lower. Fig 3.6 shows typical microstructure characteristic of <c> component dislocation loops. It is necessary for loops to have a diameter of at least 10nm in order to be detected by transmission electron microscopy (TEM). Accordingly, the authors suggest the interstitial c-loops are too small to be observed compared with large vacancy loops, which are more commonly observed. <c>-loop nucleation in zirconium and its alloys by irradiation has yet to be explained consistently.

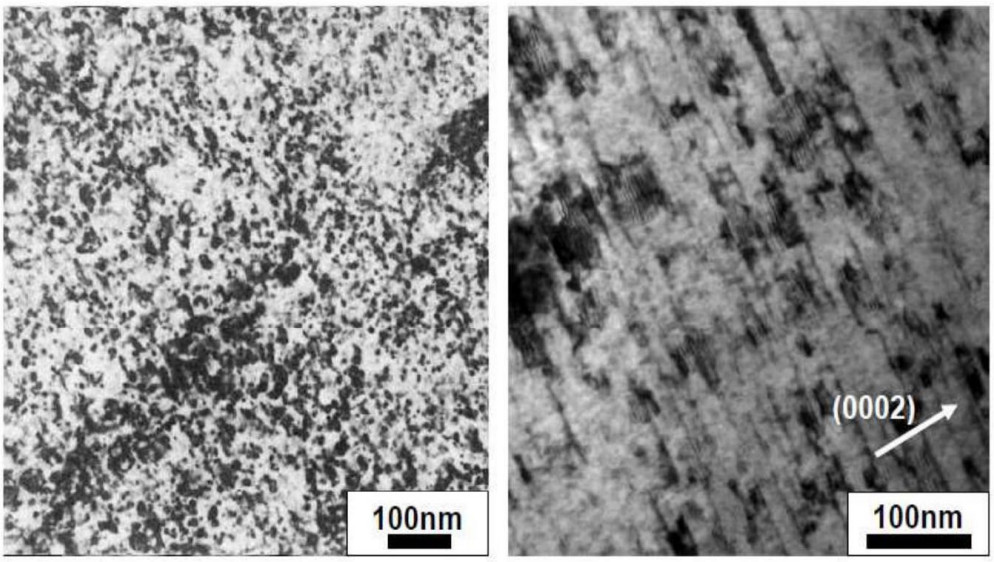

Figure 3.6: Left: <a> loops in annealed Zry-2; right: $< \boldsymbol{c} >$loops in recrystallized low-tin Zry-4, irradiated at Research Reactor [57]

Table 3.3 summarizes various results from transmission electron microscopy observations for ⟨c⟩ loops. The following trends are noted:

i. [76,77] at fixed irradiation temperature, density of loops decreases with the irradiation dose.

ii. [54,73] at a given irradiation dose, the average loop density increases with irradiation temperature. The ability of loops to emit vacancies is greater at higher irradiation temperatures. This should limit their growth in size unlike <a> loops.

Table 3.3: Characteristics of the dislocation loops (c) observed in zirconium and Zircaloy-4 under neutron irradiation

Ref.	Plane	$\vec{b}$	$\| \vec{b} \|$ (Å)	Type
[55,78]	$\{10\bar{1}1\}$	$\frac{1}{3}\langle 11\bar{2}3\rangle$	$\sqrt{a^2+c^2}=6.07$	Interstitial
	(0001)	$\frac{1}{6}\langle 20\bar{2}3\rangle$	$\sqrt{\frac{1}{3}a^2+\frac{1}{4}c^2}=3.17$	Vacancy
	(0001)	$\frac{1}{2}[0001]$	$\frac{1}{2}c=2.57$	Vacancy
	(0001)	[0001]	$c=5.14$	Vacancy

Ref.	Material	$T_{Irr.}$ (°K)	(dpa)	$\Psi(\mathrm{p.m^{-2}})$ x 10^{24}	$\bar{d}$(nm)	$\bar{\rho}(\mathrm{m^{-3}})$ x 10^{19}
[76]	Zircaloy-4 Recrystalized	583	14	-	>150	<120
[77]		583	35	-	>150	<117
[73]	Zircaloy-4 Alpha-annealed	630	-	29.3	>136.7	1.37
[54]		673	-	31	>110	2.21

Ref.	Material	$T_{Irr.}$ (°K)	(dpa)	$\Psi(\mathrm{p.m^{-2}})$	c-component
[68,75]	Zircaloy-4	644	18	1.8×10^{25}	yes
	Sponge-Zr	644	64	1.6×10^{25}	yes
		644	21	5.3×10^{25}	no
		710	22	5.3×10^{25}	yes
	Crystal bar-Zr	700	4	1.1×10^{25}	no

iii. [68,75] ⟨c⟩ loops can form in the vicinity of second phase precipitates. Observations by Griffiths and Holt [55,63] show a higher density of ⟨c⟩ loops in the vicinity of intermetallic precipitates, such as the $Zr(Fe,Cr)_2$ Laves phases. The results observed on the different samples also show that the germination of the loops strongly depends on the presence of alloying elements. Indeed, all things being equal, the irradiation threshold, the size of the loops or their density differ according to the type of material observed.

3.2.1.3 Alloying elements and Secondary Phase Precipitates (SPP)

During displacement, the material becomes overheated, molten, a condition termed "thermal spike". The disordered or amorphous phases may be formed through that process. As a result of cascades, the atomic structure of the target becomes disordered, affecting how alloy precipitates behave when irradiated with neutrons. Under irradiation, Abromeit and colleagues [79] identify two major mechanisms of atomic transport: atomic mixing and radiation-enhanced interdiffusion. The dissolution of preexisting phases occurs as a result of atomic mixing in the recoil cascade volume. The diffusion of vacancies and self-interstitials is slowed by metallic compounds that have small elemental radii. The combination of undersized atoms with self-interstitials results in defects with lower mobility as compared with the self-interstitials alone [80]. Hood specifically mentioned the role that Sn plays in resolving interstitial vacancy clustering and interstitial-vacancy recombination following irradiation damage in Zr [80].

As the SPP becomes amorphous, it has been observed that Fe is the first alloying element that dissolves from the SPP into the matrix, followed by Cr and Ni (see Figure 3.7). Amorphization cannot be driven by diffusion since Motta [81] observed a linear relationship between amorphous layer thickness and dose. In contrast, when the alloying elements are displaced during the amorphization process, their diffusing coefficients may differ, which could contribute to the staggered release of materials. In comparison to other alloying elements, Fe has the highest diffusion coefficient comparing other alloying elements like Cr [82,83]. In contrast to Zr SIAs, Ni, Fe , and Cr diffuse preferentially along the c-direction of the lattice, while SIAs diffuse preferentially in the basal plane [83].

Metal alloying elements tend to segregate to surface and grain boundaries as soon as they are introduced into the matrix. There is an interaction between defects and

the remaining elements in the matrix. An attraction between Fe atoms and vacancies has been demonstrated [84]. The observation that vacancy c-loops form around precipitations dissolving in the matrix and the attraction of vacancies to Fe suggest that Fe could be a nucleation site for vacancy clusters [58,85].

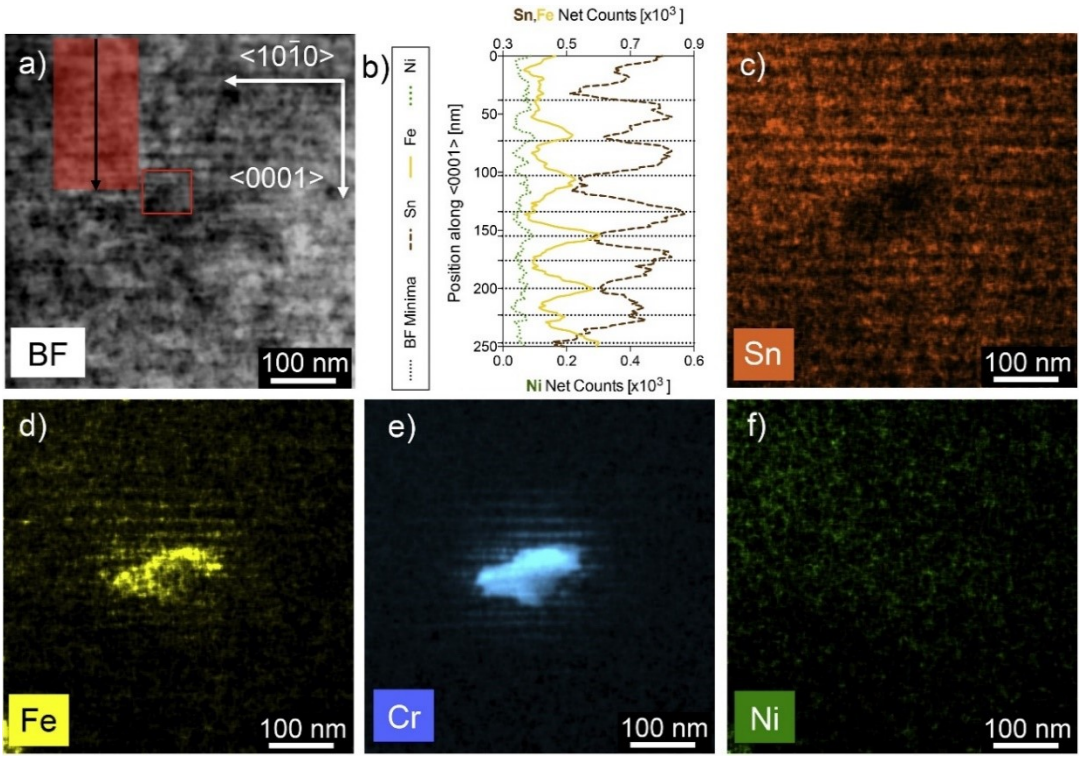

Figure 3.7: Chemical segregation close to an SPP (center). The BF-STEM image in a) in Zircaloy-2 after neutron irradiation in a BWR to 9.5 x 10^{25} nm^{-2} ~15.8 dpa. Sn, Fe, Cr and Ni maps are shown in c), d), e), f), respectively, and a line scan along the ⟨0001⟩ arrow in a) is shown in b [82].

3.2.2 Effects of Mechanical Behaviour

As a result of irradiation, Zircaloys undergo changes in their mechanical properties [52,86,87]. With all metals, neutron irradiation increases strength while decreasing macroscopic ductility [53,54,86]. It is normally observed that tensile yield stress increases (Figure 3.8), ultimate tensile strength increases, hardness increases and ductility decreases (e.g. [54,88,89]).

During the development of the thermal reactor, zirconium alloys have been intensively studied for dimensional changes caused by neutron irradiation

[87,90,91]. In contrast to most other engineering alloys, zirconium alloys resist swelling during irradiation. In the absence of a stress, anisotropic dimensional changes can be observed depending on the microstructure, which is called irradiation growth (e.g. [91–94]). They also exhibit dimensional responses to stress, a process known as irradiation creep (e.g., [91,92,95,96]).

When neutrons are irradiated inside material, defects such as voids and dislocation loops are formed, which alter the slip system's ability to withstand plastic deformation and alter its mechanical properties. Irradiation hardening, growth and creep are the source of mechanical changes for Zircalloys during reactor operation and long term. In this section, the letter was not included since it is not covered by the scope of this work.

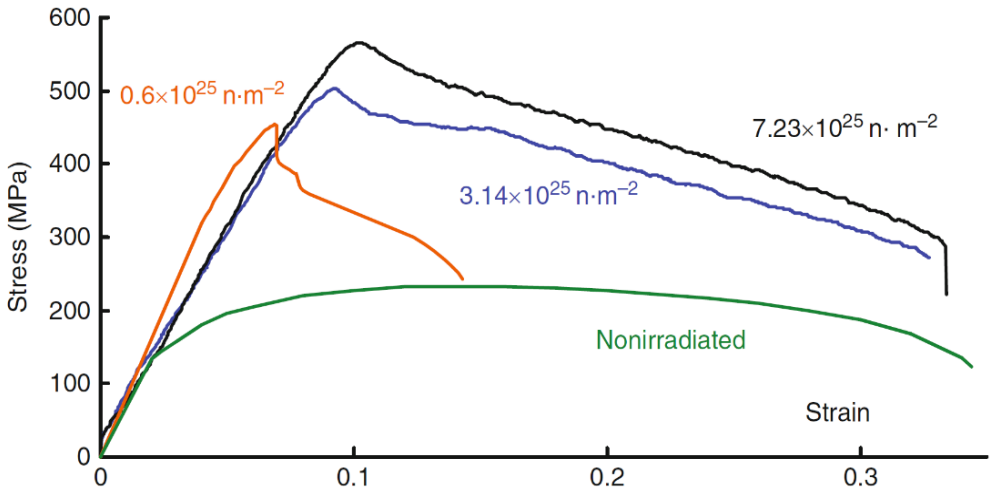

Figure 3.8: Effect of neutron irradiation on the mechanical properties of Zry-4 [97]

3.2.2.1 Irradiation hardening

A common problem with pressurized water reactor fuel cladding tubes is the reduction in ductility associated with irradiation hardening [55,60,97]. Loops act as barriers to dislocation motion and increase the strength of irradiated alloys. It is <a> dislocation obstacles that cause this form of strengthening with irradiation, which occurs at low fluences and saturates at high fluences. Damage loops increase Zr-alloy yield strength simultaneously with damage loop development [98–102]. Furthermore, the presence of strain localization and inhomogeneous deformation

can lead to fractures with low macroscopic strains (i.e., low ductility). Irradiation embrittlement is the term generally used to describe this phenomenon. Dislocation channels within brittle hydrides further increase embrittlement through crack initiation and propagation.

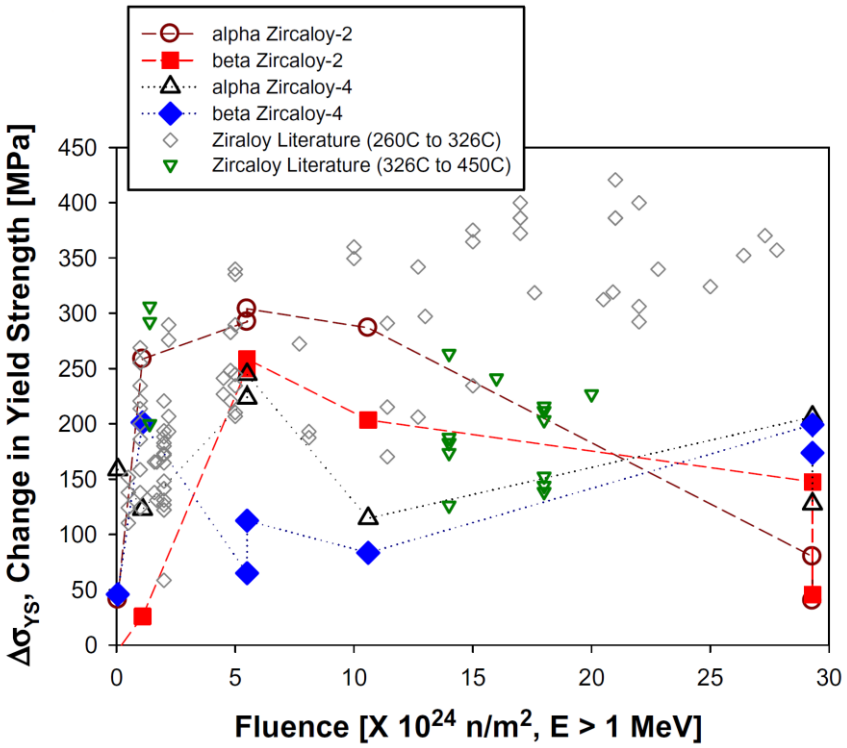

Figure 3.9: Post-irradiated irradiation hardening data for Zircaloys irradiated at nominally at 358°C compared with the literature results for Zircaloy irradiation at 260–326 °C [73].

At about 623° K reactor operating temperature, plastic deformation is associated with <a> dislocation in motion in the prism plane of unirradiated Zr-alloys. Irradiation-induced work hardening occurs when moving dislocations interact with irradiation-induced defects (mainly <a> loops). As a result of irradiation hardening, other slip planes may become active (basal and pyramidal) [91].

There is a common observation that an increase in yield stress of approximately 100 MPa occurs when tested at room temperature when exposed to dose, exposure time, and test conditions [102,103]. Cockeram stated that under a neutron fluence

range of between 15 x 10^{24} neutrons/m^2 and 20 x 10^{24} neutrons/m^2, yield strength increase of zircaloys at 358° C is between 120 and 230 MPa as seen in Figure 3.9[54,73].

3.2.2.2 Irradiation growth

Zr alloys display irradiation-induced growth (IGG) due to their anisotropic crystal structure. When exposed to irradiation without any stress, Zr alloys are observed to grow along the a-axis and contract along the c-axis, preserving the material's volume. Fluence, temperature, texture, chemical composition, and irradiation conditions significantly affect IIG. In low fluences (*1 dpa), a rapid decrease in strain occurs, followed by a saturating period between 1 and 3 dpa, after which the strain rapidly increases again (at fluences of 2 x 10^{26} neutrons/m^2). An increase in strain that occurs rapidly is known as breakaway growth [93]. Holt et al. stated that annealed Zry-4 irradiated by neutrons at about 290°C was shown to have <c>-component loops along with high levels of <a>-loops, while Zry-2 and Zry-4 irradiated at lower doses exhibited only <a>-loops. Observations on the dislocation loops correlated with the observations of growth behaviour in the samples when annealed Zircaloy at 550K began to show an acceleration of growth referred to as 'growth breakaway' [63,104]. Figure 3.10 shows the growth of Zircaloy-4 at low fluence (pre-breakaway). Texture and temperature are effective parameters which can be clearly seen.

For different reactor types, Zr-alloys, and irradiation conditions, irradiation-induced deformation of Zr-based alloy components was studied and discussed [87,100,105]. An empirical model was developed based on these studies and the operational experiences of fuel vendors to predict (among others) the irradiation growth of PWR fuel assemblies. As reported, there is a relationship between the occurrence of <c>-loops and breakaway growth, so it is not sufficient to simply examine macroscopic component deformation, but also the nucleation mechanisms and characteristics of <c>-component dislocation loops to gain a full understanding of the irradiation deformation phenomenon [59].

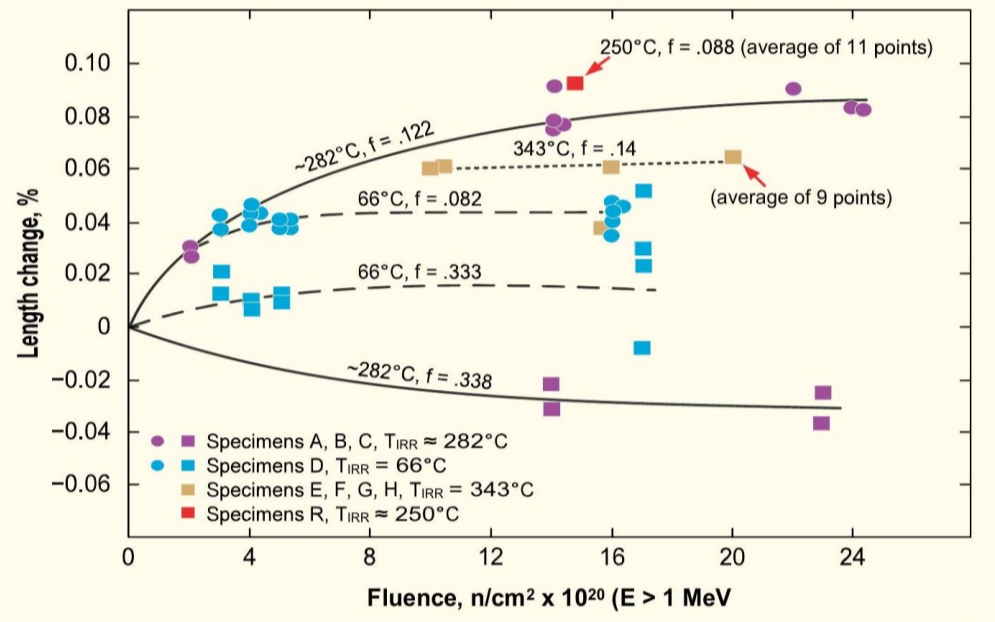

Figure 3.10: Irradiation growth of Zircaloy-4 as functions of fluence, texture and irradiation temperature ($\mathbf{20 = 3dpa}$) [106]

4 Theory of Radiation Damage

The radiation damage event is defined as the transfer of energy from an incident projectile to the solid, which is followed by the distribution of target atoms. Radiation damage occurs as a result of several distinct processes. Following is a list of these processes in order of occurrence:

1. An energetic incident particle interacts with a lattice atom.

2. In this process, kinetic energy is transferred to the lattice atom, resulting in a primary knock-on atom (PKA).

3. Displacement of the atom from the lattice site.

4. Knock-on atoms are formed by the passage of the displaced atom through the lattice.

5. A displacement cascade (a collection of point defects created by the PKA).

6. In the form of an interstitial, the PKA terminates.

Radiation damage will end when an interstitial PKA rests in the lattice. Radiation damage produces vacancies and interstitials in the crystal lattice and clusters of these defects. The entire sequence of events takes only about 10^{-11} s [107] (Fig 4.1). Further events, such as migration and clustering of the defect clusters, are classified as radiation damage effects.

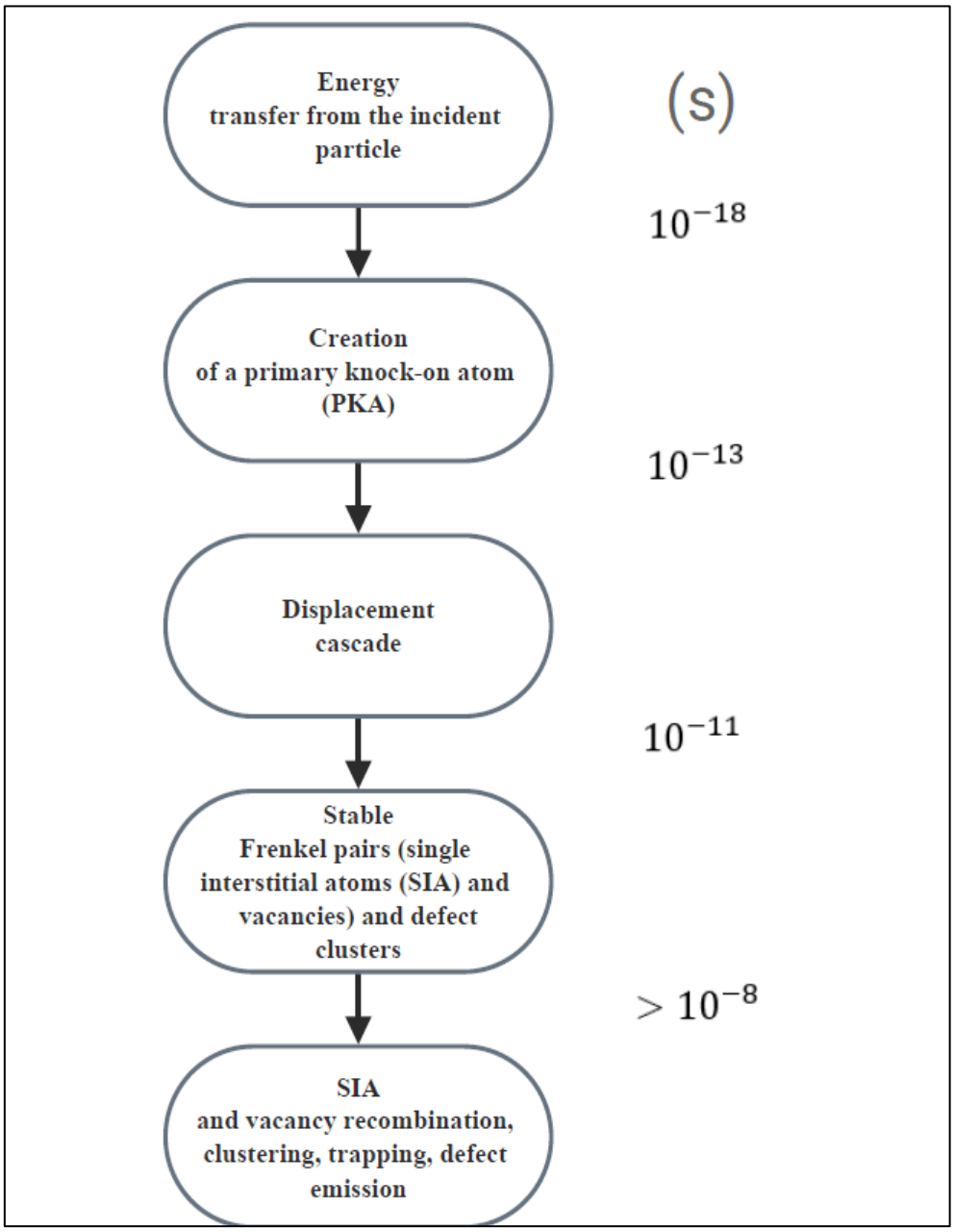

Figure 4.1: Approximate timescale for the production of defects in irradiated metals (from [107])

4.1 Neutron-Nucleus Interaction

Neutron irradiation begins when an unstable radionuclide emits gamma(γ) rays and fissile particles such as neutrons, ions, electrons, and other fission products [52]. According to the energy spectrum generated in a nuclear reactor, thermal neutrons are released along with alpha (α) particles, beta (β) particles, gamma rays, and other fission products.

When thermal neutrons interact with non-fuel material nuclei, they are absorbed or captured, leaving these nuclei in an excited or high energy state. The excess energy (from the gamma rays and nuclei recoiled) is released by emitting high-energy gamma rays, which in turn cause these emitting nuclei to recoil [108]. Fig. 4.2 illustrates how highly energetic radiations or particles change the mechanical properties of matter. It is these changes that begin at the microscopic level and proceed to the macroscopic level. Whenever the kinetic energy exceeds a certain minimum, known as the displacement energy, which in most metals is similar to 25 to 30 eV, the recoiling ("knock-on") atom is displaced from its equilibrium position. In contrast to this, the released high-energy gamma radiation is ionized and excited, resulting in electrons or positrons having kinetic energy which dissipates heat. It is also possible that excited compound nuclei will transmute into other nuclei, which may be radioactive, which results in the accumulation of impurities, such as alpha particles (helium) and protons (hydrogen) [109,110].

Fast neutrons, due to their high energies, collide elastically with atomic nuclei and produce alpha and beta particles in addition to transferring their kinetic energy to the recoil nucleus. As the recoil nucleus undergoes ionization and excitation, electron energy is dissipated as heat. Moreover, the recoiling atom (also known as primary knock-on atom) may be displaced from its equilibrium position in the crystal lattice because of its high kinetic energy [109,110]. As a result, the PKA has a substantial amount of kinetic energy, which allows it to create additional lattice displacement until it no longer possesses the energy to emit another atom. A secondary or higher order knock-on is a result of displaced lattice atoms in the following generation. Finally, once the fast neutron has been slowed down to the point where atomic displacement is no longer possible, much of its remaining energy will be dissipated by vibrations in the target atom (heat) [108,110].

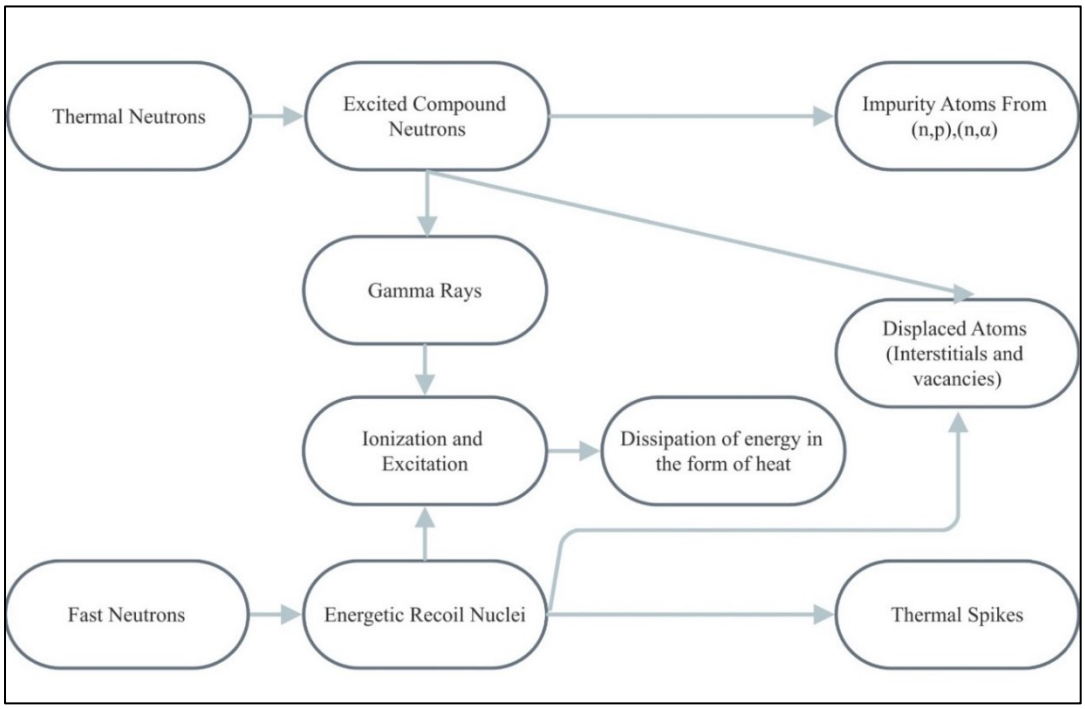

Figure 4.2: Mechanisms of irradiation damage in the nuclear reactors by thermal and fast neutrons [109]

4.1.1 Elastic Scattering

As a result of their electrical neutrality, neutrons and nuclei can be viewed as colliding hard spheres. The probability of neutrons colliding with a lattice atom is finite after they pass through a solid, imparting a recoil energy to it. Double differential scattering cross sections (in energy and angle) $\sigma_s(E_i, E_f, \Omega)$ are used to determine the probability, where are the incident E_i and final energies E_f and is the solid angle in which the neutron is scattered [111]. Our interest is often limited to the scattering probability as a function of E_i and the scattering angle. The total scattering probability of neutrons is as follows:

$$\boldsymbol{\sigma_s(E_i) = \int \sigma_s(E_i, \Omega) d\Omega} \qquad 4.1$$

Studying irradiation effects involves examining the behavior of the struck atom. Hence, we are interested in the cross section for energy transfer $\sigma_s(E_i, T)$, or whether a neutron will transmit recoil energy T to a mass atom M after elastically scattering against it. First, one must determine T in terms of the neutron energy and scattering angle.

$$\mathbf{T} = \frac{\boldsymbol{\gamma}}{\mathbf{2}}\mathbf{E_i}(\mathbf{1} - \mathbf{cos}\ \boldsymbol{\phi}) \tag{4.2}$$

where it is defined as

$$\boldsymbol{\gamma} = \frac{\mathbf{4mM}}{\mathbf{(M+m)^2}} = \frac{\mathbf{4A}}{\mathbf{(1+A)^2}} \tag{4.3}$$

where $1 = m$ and $A = M$. The energy transferred rises from 0 at $\phi = 0$ to a maximum of γE_i at $\phi = \pi$, or $T_\mathrm{max} = \hat{T} = \gamma E_\mathrm{i}$ as shown in Fig. 4.3. When a particle backscatters, the energy transferred is the most, while if it misses its target, the energy transferred is the least($\phi = 0$).

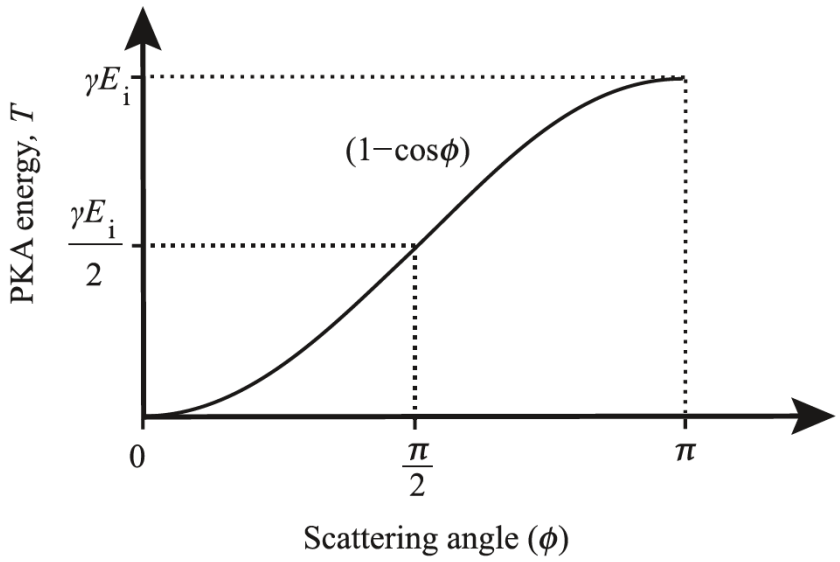

Figure 4.3: Energy transfer as a function of center of mass scattering angle([111])

In order to determine whether a given T will be imparted to the recoil atom, we need to have a probability for it. It depends on the differential cross section. As differential probabilities depend on transformed variables, $\sigma_\mathrm{s}(E_\mathrm{i}, \phi)$ can be expressed as [111]:

$$\boldsymbol{\sigma_s}(\mathbf{E_i}, \boldsymbol{\phi})\mathbf{d\Omega} = \boldsymbol{\sigma_s}(\mathbf{E_i}, \mathbf{T})\mathbf{dT}. \tag{4.4}$$

The probability that a neutron of energy E_i will impart a recoil energy T to an atom of mass M does not depend on its recoil energy. Now the average recoil energy can be calculated as follows [112]:

$$\bar{\mathbf{T}} = \frac{\int_{\check{\mathbf{T}}}^{\hat{\mathbf{T}}} \mathbf{T}\boldsymbol{\sigma}_{\mathbf{s}}(\mathbf{E_i},\mathbf{T})\mathbf{dT}}{\int_{\check{\mathbf{T}}}^{\hat{\mathbf{T}}} \boldsymbol{\sigma}_{\mathbf{s}}(\mathbf{E_i},\mathbf{T})\mathbf{dT}} = \frac{\check{\mathbf{T}}+\hat{\mathbf{T}}}{\mathbf{2}} \approx \frac{\hat{\mathbf{T}}}{\mathbf{2}} = \frac{\boldsymbol{\gamma}\mathbf{E_i}}{\mathbf{2}}. \quad 4.5$$

4.1.2 Inelastic Scattering

A neutron absorbs by a nucleus during an inelastic collision, resulting in a compound nucleus that emits a neutron and a γ -ray. In the event of an interaction, more than one γ emission may occur as well as the nucleus remaining in an excited state. It is possible to distinguish between resolved and unresolved resonance components in inelastic scattering [113]. As a function of the γ decay energy Q_j of the residual nucleus, the scattering cross section will be determined for a given resonance (j^{th} resonance) of the target nucleus. Differential equality $\sigma_{sj}(E_i, Q_j, T)\mathrm{d}T = \sigma_{sj}(E_i, Q_j, \phi)\mathrm{d}\Omega$ can be expressed in the following way:

$$\boldsymbol{\sigma}_{\mathbf{sj}}(\mathbf{E_i}, \mathbf{Q_j}, \mathbf{T}) = \boldsymbol{\sigma}_{\mathbf{sj}}(\mathbf{E_i}, \mathbf{Q_j}, \boldsymbol{\phi})\mathbf{2\pi sin}\ \boldsymbol{\phi}\frac{\mathbf{d}\boldsymbol{\phi}}{\mathbf{dT}} \quad 4.6$$

Since kinetic energy is not conserved, the expression of recoil energy as follows:

$$\mathbf{T}(\mathbf{E_i}, \mathbf{Q_j}, \boldsymbol{\phi}) = \frac{\boldsymbol{\gamma}}{\mathbf{2}}\mathbf{E_i} - \frac{\boldsymbol{\gamma}}{\mathbf{2}}\left[\mathbf{E_i}\left(\mathbf{E_i} + \mathbf{Q_j}\frac{\mathbf{A+1}}{\mathbf{A}}\right)\right]^{\mathbf{1/2}}\mathbf{cos}\ \boldsymbol{\phi} + \frac{\mathbf{Q_j}}{\mathbf{A+1}}. \quad 4.7$$

Energy can be transferred through elastic scattering, inelastic scattering, $(\mathrm{n}, 2\mathrm{n})$ reactions, and (n, γ) reactions. As neutron energies rise above 1.0 and $8.0\mathrm{MeV}$, respectively, the first two reactions become increasingly important, while the last occurs at thermal neutron energies in $^{235}\mathrm{U}$.

It is possible to estimate the recoil energy if the neutron cross section and energy spectrum of neutrons with the target nucleus are known. A typical neutron spectrum on the inner surface of a PWR vessel is given in Figure 4.4, almost all neutrons have an energy lower than 3 MeV. The total number of neutrons with an energy higher than 1 MeV received per time unit (so- called the neutron flux) at the peak location is typically around 10^{12} n.cm^{-2}.s^{-1}. Such a flux leads to a fluence of some 10^{19} ncm^{-2} for 1-year full power operation.

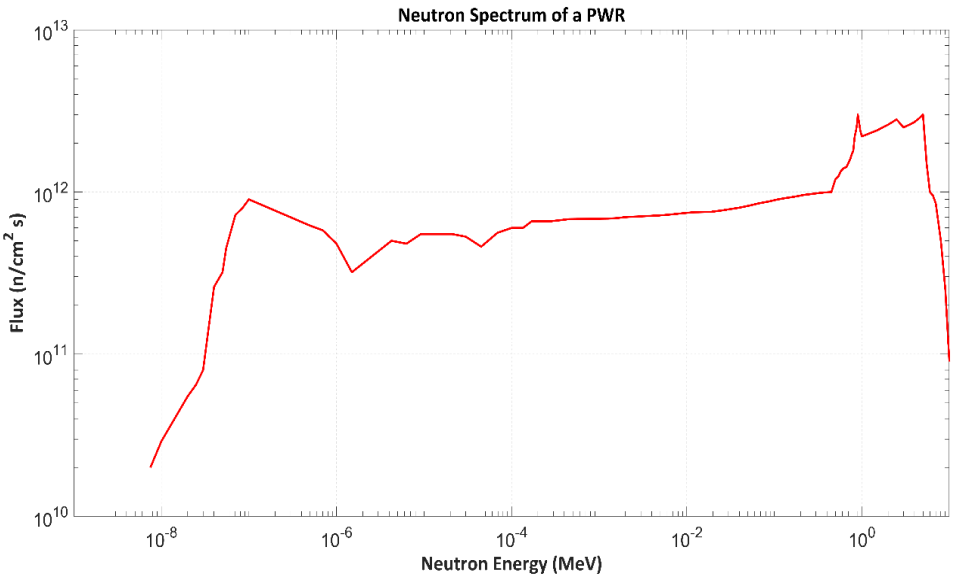

Figure 4.4: a typical neutron spectrum for PWR

4.2 Displacement Cascades

PKAs are the first atoms of a solid to be struck by high energy particles. Through electron excitation in the solid and collisions with surrounding atoms, energy transformed from the particle to PKA will dissipate [111]. Before coming to rest, PKA might undergo a series of lattice displacements. As a result of a single primary knock-on atom, a displacement cascade is created [114–116]. This work does not address ionization caused by electron excitation. The following discussion also ignores energy losses caused by electron excitation and electron-phonon interaction. The reason for simplifying the discussion is that electron excitation energies make a small contribution to cascade evolution and electron-phonon interactions do not have an important role [117–119]. In the recent discussion on the impact of electronic energy losses in cascade simulation, these conclusions are provided in Ref [120–122]. Consequently, the collision can be regarded as purely elastic, and the collision's total kinetic energy is equal to the collision's PKA energy.

In the first 100 fs, a cascade of collisions produces defects like vacancies and interstitials in a tree-like structure. As PKA energy increases, displacement cascades are larger (e.g. [123]); when PKA energy is sufficiently high, displacement cascades divide into sub-cascades [114]. Immediately following the collision stage, a high temperature period in the cascade region, known as the thermal spike, will last for hundreds of femtoseconds. Time evolution of a cascade

is shown in Figure 4.5. When all the PKA energy has been dissipated in the displacement cascade, most of the created vacancies and interstitials annihilate one another. During this recombination phase, only a few point defects remain.

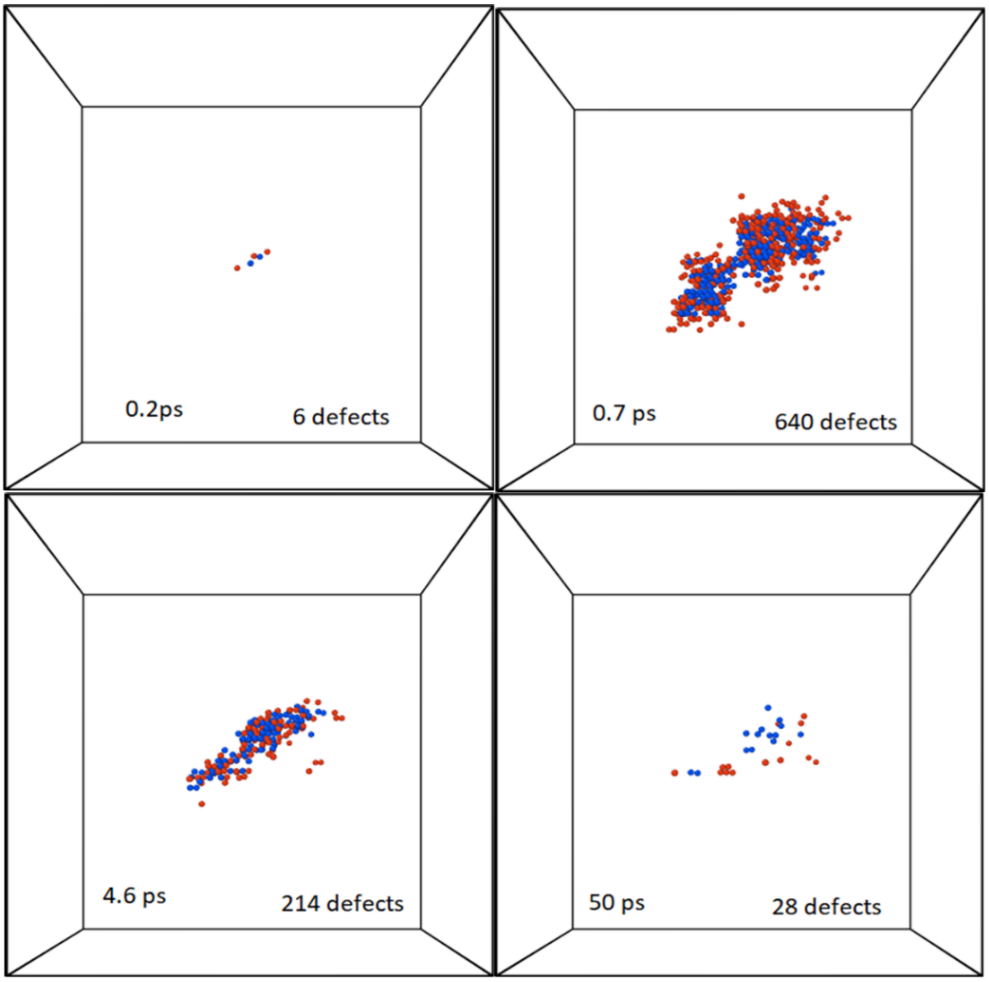

Figure 4.5: Time evolution of a displacement cascade in Zirconium caused by a PKA with the energy of 15keV. Blue (vacancy), Red(interstitial)

Vacancies and interstitials can annihilate one another or agglomerate to form defect clusters shortly after the cascade, when the heated zone cools off from 1 ps to 10 ps. Vacancy clusters, interstitial clusters, and single point defects are the end products of irradiation damage [111].

In the center, there is a zone that is highly diluted with many vacancies [124]. In displacement cascade, several processes are shown in Figure 4.6: crowdion (elongated interstitials in a close packed direction), focusing collisions (sequences

of collisions in a close packed direction [125], Frenkel pairs (Self Interstitial Atom and Vacancy pairs). There is no specific position for the self-interstitial atom (SIA) in the lattice (octahedral or tetrahedral, or another); practically, two SIAs share one lattice site and form a dumbbell shape. Cascades typically measure tens of nanometers in size.

When Zirconium is irradiated by neutrons, the energy of neutron is set as 1 MeV, which means that PKA's maximum energy (Tmax) is around 40 keV. A zirconium neutron cross section will also influence PKA energy, as the probability of elastic collision between zirconium and neutrons depends on neutron energy.

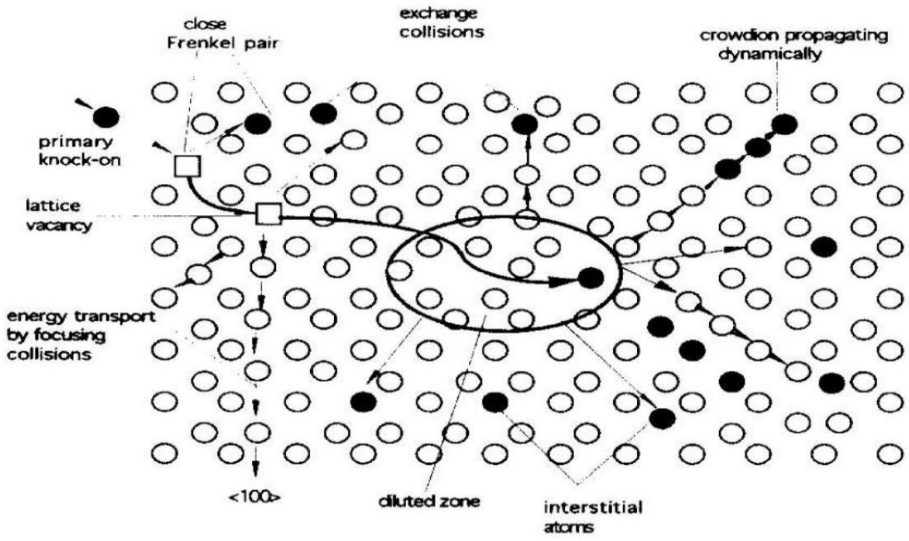

Figure 4.6: Different processes in one displacement cascade [126]

4.3 Microstructural Effect of Radiation Damage

Several phenomena can be classified as radiation damage effects following a Radiation Damage Event:

- Movement of clusters and point defects in a crystal structure, possibly recombination of interstitial vacancies or growth of clusters,
- Change in material composition caused by the mobility of impurities in alloys,

- Degradation of structural properties and impairment of component functionality.

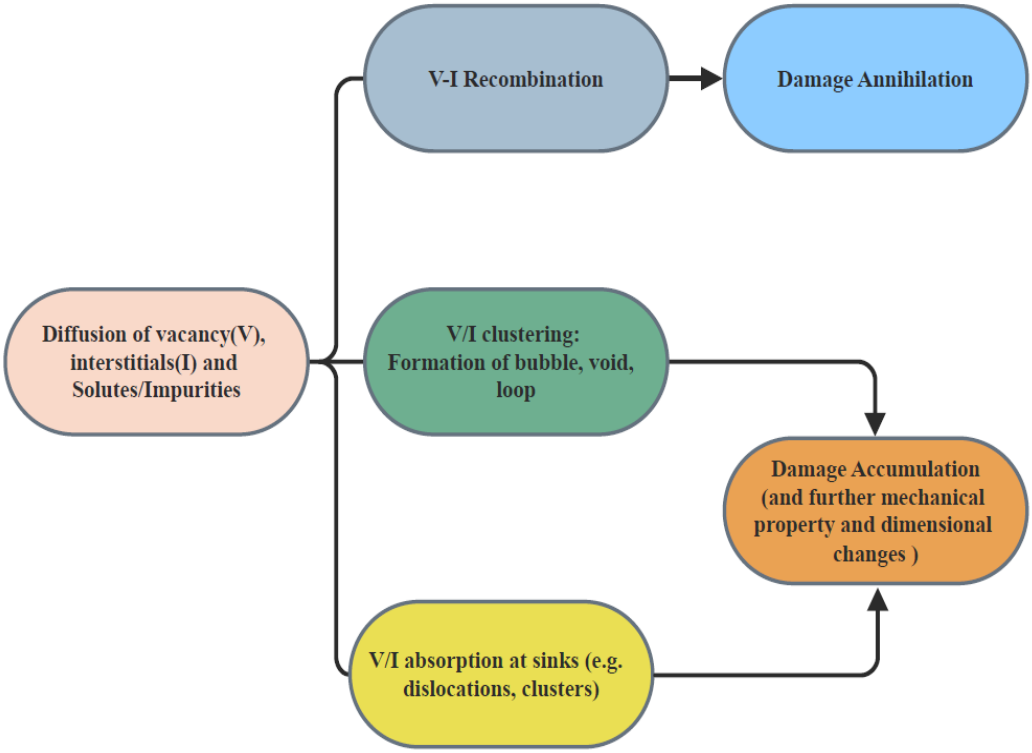

Figure 4.7: Radiation damage defects creation processes [127]

When a lattice is irradiated, as shown in Figure 4.7, interstitial and vacancy point defects in Figure 4.8 appear and often alter the properties of the material. As these freely migrating point defects combine to form higher-order point defect complexes, interstitial and vacancy defects are often highly mobile and readily diffuse through the crystal lattice.

4.3.1 Clusters Formation

Cascade collapse leaves point defects in the material which do not necessarily stay isolated in the target matrix but tend to form clusters and pairs. Whenever a vacancy occurs in an atomic structure, the lattice configuration around it changes slightly, adjusting to the new Coulomb potential. Consequently, the surrounding atoms are subjected to a strain that is absent in the equilibrium state without the vacancy, which increases the material's free energy. The strain caused by two or more

vacancies located next to each other will be less than the strain caused by two single vacancies. In interstitials, the principle is similar, with the difference that the strain pushes the surrounding atoms away from the interstitials' location rather than bringing them closer. This results in a lower free energy for the system, which is why defects tend to aggregate [128].

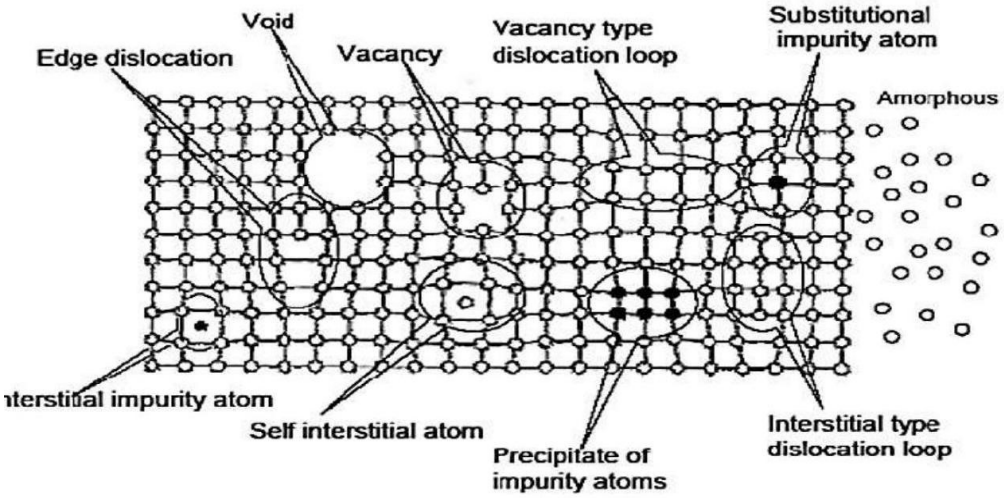

Figure 4.8: Defects in the lattice structure of materials [129]

Due to intracascade recombination, rather than forming single defects, a significant fraction of defects forms clusters. A stable cluster can also migrate away from the cascade region and be absorbed by sinks such as dislocations and grain boundaries. Two types of interstitial clustering exist. In the first case, interstitial clusters are formed as atoms are displaced away from the cascade center by the shock wave and are pushed into interstitial sites during the transition between the collisional and thermal spike phases. Short-range diffusion between neighboring interstitials can also cause clusters during the thermal spike phase. There is also a clustering of vacancies within the cascade core, varying depending on the host lattice. A fraction of vacancies in clusters in irradiated metals is estimated to be less than 15% based on measurements of size and number density. Vacancy clusters are not nearly as stable as interstitial clusters, so the true fraction may be higher due to their invisibility [52].

The mobility of interstitial clusters is greater than that of vacancy clusters [130]. Vacancy clusters have a very similar formation energy to interstitial clusters in prismatic planes, but SIA clusters have a higher binding energy than the

equivalent vacancy cluster [131,132]. While the cascade's lifetime (* 10ps) is being observed, clustered SIAs can migrate over atomic scale distances [133,134]. In Zirconium, cluster motion requires between 0.010 and 0.018 eV of activation energy [135]Cluster jump frequency can be expressed as follows by weakly varying activation energy:

$$\mathbf{v_n = v_0 n^{-S} exp\,(-\langle E_m \rangle / kT)} \qquad 4.8$$

where $\langle E_{\mathrm{m}} \rangle$ is the average effective activation energy, v_0 is the size-independent, pre-exponential factor, and the term n^{-S} is the cluster size dependence, where a value of s describes the cluster size dependence of the pre-exponential factor.

4.3.2 Dislocation Loops

Dislocation loops result from vacancy and interstitial condensations and shrink or grow according to the flux of defects reaching the embryo. As the loops reach a critical size, they become stable and grow until they become unfaulty through interactions with other loops or dislocations in the network.

Point defects form on one dimensional plane by lines, 2 dimensional planes by discs, and 3 dimensional planes by voids. A loop or platelet occupying the minimum energy configuration has a thickness equal to a Burgers vector (which, in two dimensions, lies between adjacent close-packed planes). For large numbers of vacancies, planar loops are more stable [111]. It is qualitatively consistent for zirconium to be devoid of voids with the formation energies for these extended defects shown in Figure 4.9.

Loop nucleation is mainly a clustering process, in which enough of one type of defect clusters in the presence of other types. This will result in an embryo of critical size that will survive and grow. The radius of a loop consisting of n vacancies (or interstitials) is [136,137]:

$$\boldsymbol{r_L = \left(\frac{\sqrt{3} a^2 n}{4\pi}\right)^{1/2}} \qquad 4.9$$

where a lattice unit.

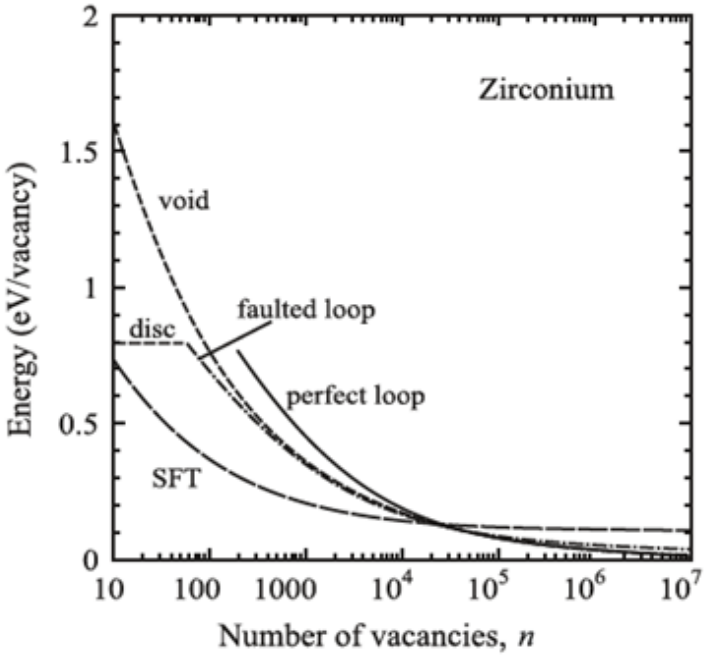

Figure 4.9: Formation energy for various vacancy cluster defects in zirconium as a function of the number of vacancies in the cluster [52]

5 Mathematical Description of Modelling Radiation Damage

5.1 Modeling Techniques

In multiscale modeling of nuclear reactor materials, one of the most challenging aspects is predicting the evolution of the microstructure over a period of time that affects the reactor's lifetime. In order to develop these models, it is necessary to take time scales ranging from picoseconds to years into account. An extensive range of kinetic processes leads to the microstructural evolution of irradiated materials. Using just one modeling technique, it is almost impossible to understand the mechanics and kinetics of the interaction of different types of defects with one another. This is because they are all under the influence of reactor conditions It is possible to calculate the initial penetration of energetic particles (with energies of keV or higher) into matter using different codes that treat the particles as moving along straight paths between collisions. Neutrons collide only with nuclei, and the collision probability can be calculated from nuclear reaction cross sections. Such neutronics calculations can be performed using Monte Carlo methods. Energetics of point defects and extended defects are determined by first principal calculations and MD. Kinetic process such as diffusion, clustering, and annihilation of defects by sinks are studied using techniques such as Kinetic Monte Carlo (KMC) and Rate Theory (RT) which can be seen in Figure 5.1. Techniques such as KMC and RT require input information about energetics of defects and behavior of small clusters using MD and ab initio calculations.

In this chapter, modeling techniques that have been used to describe the damage mechanism in the different phases are presented.

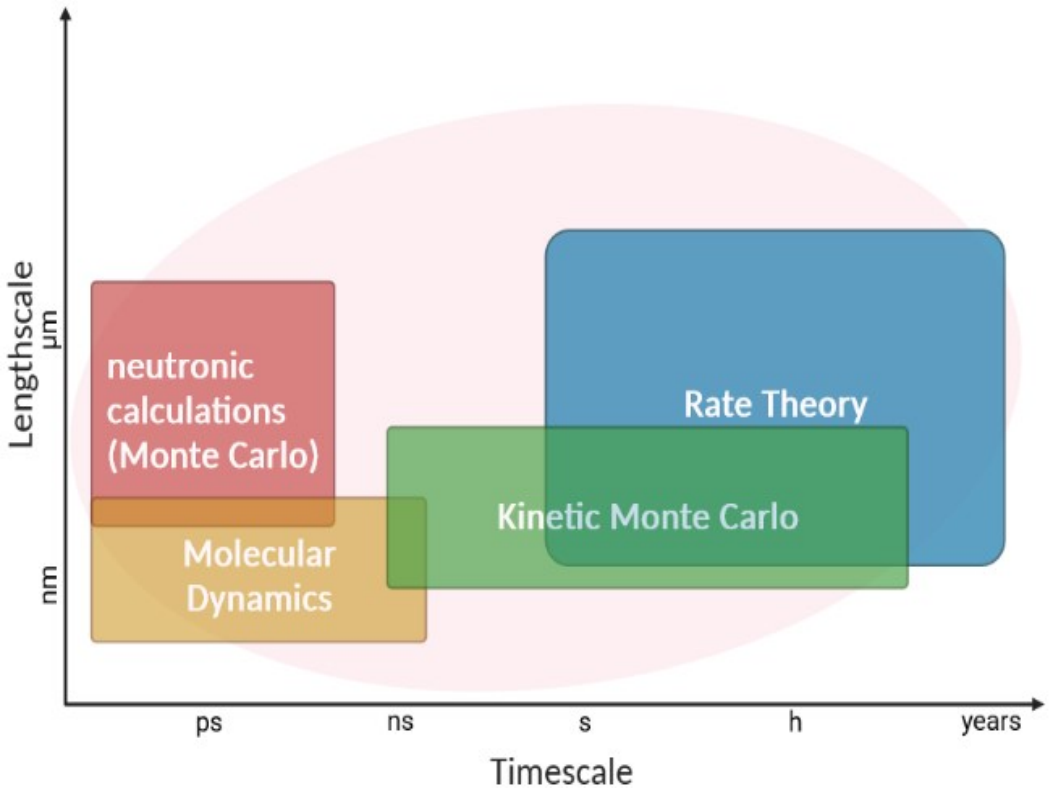

Figure 5.1: Multiscale modeling methods for radiation effects in materials

5.2 Neutronic Damage Calculations

The effect of neutron fields on fuel assemblies can be determined using Monte Carlo methods. It is essential to specify the neutron flux and spectrum in the fuel assemblies, as well as the local temperature values [138]. A Monte Carlo simulation code MCNP is used to determine these parameters [139,140]. Neutron irradiation releases lattice atoms (primary knock-on atoms: PKA), which generate cascade-like defects (interstitial atoms and vacancies) based on their kinetic energy. PKA spectrum calculations have been carried out using different methods and codes. The PKA spectrum is obtained by combining neutron radiation spectrum with nuclear recoil data using SPECTER [141] and SPECTRA-PKA [142,143] codes. Due to differences in data libraries, both codes achieve the same goal by using the same method. Using the following procedure, the primary knock-on atom's energy distribution is determined.

A displaced atom's probability (σ_D) depends on the incidence of neutrons, the cross section, and the primary recoil atom's energy distribution. Mathematically, this is expressed as [144]

$$\boldsymbol{\sigma_D(E) = \sum_i \sigma_i(E) \int_{T1}^{T2} K_i(E,T)v(T)dT} \quad 5.1$$

where E is the incident neutron energy, T is the recoil nucleus energy, $\sigma_i(E)$ is the nuclear cross section for channel i at energy $E, K_i(E,T)$ is neutron-atom energy transfer kernel for channel i and $v(T)$ is the secondary displacement function. The kernel K indicates the probability that a neutron energy E will generate a recoil atom with the energy T, also known as Primary Knock-on Atom (PKA).

Defining the neutron atom energy transfer kernel, $\kappa(\mathrm{E,T})$ is a crucial step in evaluating Equation 5.1. Each type of neutron interaction requires a different kernel. A collision between colliding particles in an elastic scattering event conserves their total kinetic energy in their center-of-mass frames. Neutrons transfer momentum to target nuclei, which recoil with an energy corresponding to their initial energy and the angle of deflection they experienced. Relativistic neutrons are usually scattered in this way.

The neutron energy transfer kernel is given as shown in Equation 5.2 [141].

$$\boldsymbol{\kappa(E,T)dt = \sum_l \frac{2l+1}{4U_1U_2E} a_l(E)P_l\left(1 - \frac{T}{4U_1U_2E}\right)} \quad 5.2$$

where:

$\mathrm{P_1}$ = Legendre polynomials

$\mathrm{U_i}$ = the mass ratio of the i particle as compared to the combined mass of the neutron and target nucleus atom, where $\mathrm{i} = 1$ for the neutron and $\mathrm{i} = 2$ for the target nucleus atom

$\mathrm{a_1(E)}$ = The energy-dependent coefficients taken from ENDF-V database [145].

Among the key terms in Equation 5.1, the secondary displacement function is the most uncertain because it requires an understanding of the nuclear stopping cross section of a recoiling atom as well as the energy required to displace the atom from

its lattice site [144]. A Norgett-Robinson-Torrens model is used to calculate the secondary displacement function. Unlike similar models, this model considers the fact that displacement does not exhibit a sharp cutoff value. In contrast, the partition between nuclear and electronic stopping varies smoothly with energy. Equation 5.3 is used to calculate the secondary displacement function [146].

$$\mathbf{v(T)} \cong \frac{\mathbf{0.8 * T_{dam}}}{\mathbf{2E_d}} \tag{5.3}$$

where:

T_{dam} = the damage energy or the nuclear stopping fraction

E_d = the displacement energy, or the threshold energy required to remove an atom from its lattice site. Recommended average displacement threshold energy for zirconium,40 eV, is used [147].

The damage energy is a function of the total energy of the primary knock-on atom that represents the amount of energy that is available to cause damage and can be calculated using Equation 5.4 [141].

$$\mathbf{T_{dam}} = \frac{\mathbf{E}}{\mathbf{(1+k_L g(\varepsilon))}} \tag{5.4}$$

where:

k_L = a correcting factor, see Equation 5.5

$g(\varepsilon)$ = a correcting factor, see Equation 5.6

$$\mathbf{k_L = 0.0876 * Z^{\frac{1}{6}}} \tag{5.5}$$

where:

Z = the atomic mass number

$$\mathbf{g(\varepsilon) = \varepsilon + 0.402\varepsilon^{\frac{3}{4}} + 3.40 * \varepsilon^{\frac{1}{6}}} \tag{5.6}$$

where:

ε = a property based on the interacting materials, see Equation 5.7

$$\boldsymbol{\varepsilon} = \frac{\mathbf{T[keV]}}{\mathbf{0.0869} * \mathbf{Z}^{\frac{\mathbf{2}}{\mathbf{3}}}} \qquad 5.7$$

5.3 Molecular Dynamics Method

As a result of PKA and lattice atoms, additional ones are liberated, resulting in further collisions and atoms being released. The result is the generation of interstitial atoms and vacancies. The initial damage caused by the energetic particles, so-called cascade damage, lasts only a few tens of picoseconds. Since the initial distribution of damage is crucial for later damage evolution, it must be accurately described. Modeling this initial stage of damage production has been very successful using MD simulations with empirical potentials. This model is capable of reaching time and length scales of nanoseconds and nanometers.

The MD simulation reproduces the physical movement of atoms and molecules by solving the many body interactions between them numerically by using classical Newton's equations [148,149].

The classical equation of motion is as following:

$$\mathbf{f_i} = \mathbf{m\ddot{r}_i} \tag{5.8}$$

where r_i is the position of atom i, f_i represents the force on atom i.

The r_i can be calculated using integration of Eq. 5.8. The force term f_i can be derived from atomic potential U:

$$\mathbf{f_i} = -\frac{\partial \mathbf{U}}{\partial \mathbf{r_i}} \tag{5.9}$$

The above two equations indicate two primary components in MD calculations: one is the numerical integration of force to derive r_i; another one is the force calculation from potential. Overall, atomic positions, velocity, and force information of one atom solely depend on atomic potential. This potential is the most crucial part in MD calculation that will be described in detail below.

5.3.1 Molecular Dynamics Procedure

The following flow chart illustrates the general procedure in Molecular Dynamics. An atomic coordinate is assigned to the crystal structure at the beginning of the process. A structure's geometry is optimized by minimizing its energy so that its equilibrium configuration has zero velocities in the final configuration. The lattice

parameters of this state correspond to the potential. This state is known as the minimum energy state. By assigning velocities to the atoms, the system can generate the appropriate temperature by vibrations of the atoms. This temperature allows the system to stabilize. Temperature rescale is applied until the required temperature is reached if it is not achieved or if it is highly fluctuating. To obtain trajectories at various time steps, various process parameters are applied to the system, such as strain, deformation, temperature, or pressure.

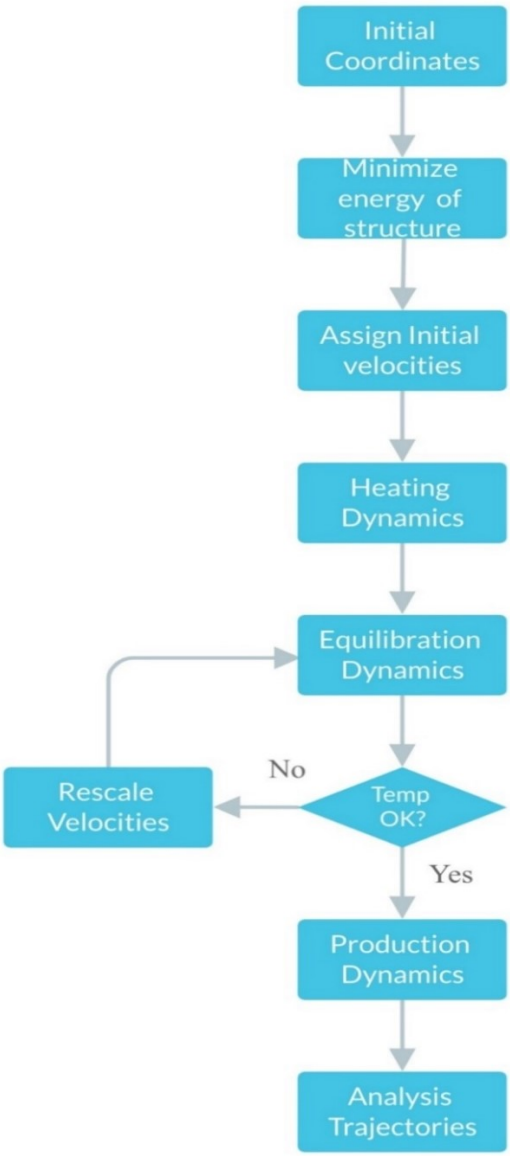

Figure 5.2: MD simulation procedure

5.3.2 . Parameters of MD Simulation

5.3.2.1 Algorithm

Various numerical methods have been developed to solve differential equations [150]. In the present MD simulations, 4th order Predictor-Corrector is applied [151]. Predication is conducted through Taylor expansion:

$$\begin{aligned} \mathbf{r(t+\delta t)} &= \mathbf{r(t)} + \mathbf{v(t)\delta t} + \tfrac{\mathbf{1}}{\mathbf{2}}\mathbf{\delta t^2 a(t)} + \tfrac{\mathbf{1}}{\mathbf{6}}\mathbf{\delta t^3 a'(t)} \\ \mathbf{v(t+\delta t)} &= \mathbf{v(t)} + \mathbf{a(t)\delta t} + \tfrac{\mathbf{1}}{\mathbf{2}}\mathbf{\delta t^2 a'(t)} \\ \mathbf{a(t+\delta t)} &= \mathbf{a(t)} + \mathbf{a'(t)\delta t} \\ \mathbf{a'(t+\delta t)} &= \mathbf{a'(t)} \end{aligned} \qquad 5.10$$

where r is position, v is velocity, a is velocity and δt represents the time-step.

The dynamic information of atomic interaction is maintained and extracted from the calculation of acceleration from potential energy. The correction will be carried out using the comparison between the acceleration estimated from the Taylor expansion and the acceleration derived from the potential.

$$\mathbf{correction} = \frac{\mathbf{F}}{\mathbf{m}} - \mathbf{a_{predicted}} \qquad 5.11$$

Eq.5.11 is employed to calculate the correction of Eq.10:

$$\begin{aligned} \mathbf{r(t+\delta\iota)} &= \mathbf{r(t+\delta\iota)} + \mathbf{correction} \times \mathbf{c_0} \\ \mathbf{v(t+\delta t)} &= \mathbf{v(t+\delta t)} + \mathbf{correction} \times \mathbf{c_1} \\ \mathbf{a(t+\delta t)} &= \mathbf{a(t+\delta t)} + \mathbf{correction} \times \mathbf{c_2} \\ \mathbf{a'(t+\delta t)} &= \mathbf{a'(t+\delta t)} + \mathbf{correction} \times \mathbf{c_3} \end{aligned} \qquad 5.12$$

In Eq.5.12, the recommended value of c_0, c_1, c_2 and c_3 are $1/6{,}5/6{,}1$ and $1/3$ respectively [151].

The correction step is normally iterated, and the initial corrected value can be applied to calculate a new acceleration; this new value can be compared again with the initial corrected acceleration to make a second correction until a satisfied error is reached.

5.3.2.2 Boundary conditions

A molecular dynamics simulation must take into account boundary conditions. Boundary conditions can be divided into four types [152]:

Periodic boundary conditions (p) - If surface properties are not involved in the simulation, periodic boundary conditions are typically implemented to reduce surface effects during property estimation. When a system consists of 1000 atoms, about half are on the outer faces. In periodic boundary conditions, when an atom leaves the simulation cubic, it will re-enter the cubic from the opposite side. For a cascade simulation, atomic collisions and thermal spikes may cross the system boundary if the computational cell is quite small; therefore, the cascade may interact with itself. Whenever a cross-boundary occurs, dampen the boundary atoms or replace the system with a significantly larger one in order to remove the heat. [153,154].

Surface, rigid, and flexible boundary conditions [155] prevent particles from entering the simulation box or leaving it, for example in a surface simulation. The rigid condition allows atoms or sides of the simulation to remain fixed. The flexible boundary allows atoms to move small amounts in response to forces exerted on the cell's perimeter.

5.3.2.3 Thermodynamic ensembles

NPT (Constant pressure and temperature)

The NPT ensemble is capable of controlling both pressure and temperature. Pressure and temperature are kept constant, allowing the unit cell volume to change. As a result of the use of this ensemble, the desired temperature and pressure can also be achieved during equilibration.

NVT (Constant volume and temperature)

The volume of the NVT ensemble is maintained constant throughout the run by controlling the temperature with direct temperature scaling. Most commonly, this ensemble is used during production runs to collect data on atom displacement at constant temperatures.

NVE Ensemble (Constant volume and energy)

During the initialization of this ensemble, total energy is conserved. It is always possible for energy to drift slightly due to rounding and truncation errors during the integration process.

5.3.2.4 Interatomic potential

It is crucial to choose the right potential in molecular dynamics simulations: a function of nuclei positions that represents the potential energy of the system when the atoms are arranged in a specific configuration. As the atoms are normally positioned relative to each other rather than at their absolute positions, this function is translationally and rotationally invariant. Due to metallic bonding, metals form strong interatomic bonds, which generate forces between atoms. Free valency electrons are produced by the ionic core, which is located inside the free valency electron sea. The result is an exponentially attractive force which is a potential function [148]. The potential function 'V' between two atoms i and j interacting at a distance r in a system of N atoms is written as the sum of pairwise interactions

$$\boldsymbol{V}(\boldsymbol{r_1}, \dots \dots \boldsymbol{r_N}) = \sum_i \sum_{j>i} \boldsymbol{\Phi}\left(\left|\boldsymbol{r_i} - \boldsymbol{r_j}\right|\right) \qquad 5.13$$

In Eq. 4.13, 'ϕ' represents the pair potential between atoms i and j as a function of their scalar distance. An electrostatic interaction, a Lennard-Jones potential, or a Morse potential interaction is one example of the basic interaction between nuclei. It is necessary, however, to have the potential in order to describe the behaviour of atoms in metals, which describe the interactions between nuclei and the electrons that surround them. Embedded atom methods (EAM) and modified embedded atom methods (MEAM) are commonly used for engineering applications in metals.

EAM is an interatomic potential developed by Daw et al [156] for metals. This method is one of the most accurate for crystal metal lattices. It has been applied to date to a variety of problems in pure metals and alloys. A single crystal metal lattice consists of positively charged nuclei embedded in a 'sea' of valence electrons that binds the nuclei together. Since the arrangement of the nuclei is periodic in all directions in the metal lattice, the inter-metallic bond is nondirectional [152], so the total energy of the system is evaluated by two factors; one is the interaction of every atom with local electron density of the entire system of atoms called embedding

energy and second is pairwise interactions created by electrostatic interactions between atoms. It can be written in the form of an equation.

$$\mathbf{E_{coh}} = \sum_{\mathbf{i}} \mathbf{G_i}\left(\sum_{\mathbf{j}\neq\mathbf{i}} \boldsymbol{\rho}_{\mathbf{j}}^{\mathbf{a}}\left(\mathbf{R_{ij}}\right)\right) + \frac{\mathbf{1}}{\mathbf{2}}\sum_{\mathbf{i,j(j}\neq\mathbf{i)}} \mathbf{U_{ij}}\left(\mathbf{R_{ij}}\right) \qquad 5.14$$

In Eq. 5.14, G is the embedding function, ρ^a is the spherically averaged atomic electron density and U is an electrostatic, two-atom interaction i and j at a distance R.

5.4 Kinetic Monte Carlo

When considering the cascade production interval (10s of ps), the continuous creation of point defects and clusters of these defects, their migration, additional clustering, and eventual dissolution represent a long-term evolution of the microstructure. As microstructural formation and evolution are statistical processes, Kinetic Monte Carlo (KMC) represents them well. KMC methods follow the kinetics of rare events or slow processes. As opposed to MD simulations where time scales can only be achieved in femtoseconds or seconds, KMC methods can reach time scales of seconds or hours. The right time and length scales allow for direct comparisons with experimental measurements. Knowing the transition rates between events is the basis of the KMC method. The transition rates between two states of a system can be computed by comparing energy barriers between them.

During the simulation, events can occur, whose probabilities of occurrence are expressed in terms of frequencies (in s^{-1}). From the set of all possible events i of each object n among the N objects in the system, each with a known rate of occurrence, $\Gamma_{n,i}$, a total rate, R, is computed [157]:

$$\boldsymbol{R} = \sum_{\boldsymbol{n,i}} \boldsymbol{\Gamma_{n,i}} \qquad 5.15$$

A Monte Carlo step is initiated by selecting an event from all the events by drawing a random number between 0 and R. The value of this number determines which event is selected. If more than one object can undergo the selected event, one is chosen at random. Once the event and the corresponding object are selected, the appropriate actions are performed to make that event occur, and the time is updated, by adding a time increment proportional to the inverse of R.

The associated time-step length δt and average time-step length Δt is given by:

$$\boldsymbol{\delta t = \frac{-\ln r}{R}\ \Delta t = \frac{1}{R}} \qquad 5.16$$

where r is a random number in $[0,1]$.

Numerous previous studies using object kinetic Monte Carlo (OKMC) techniques have investigated the long-term evolution of defects based on diffusivity data and simulation setups [[158–161]. By using the object kinetic Monte Carlo (OKMC) method, it is possible to study the kinetics of competing processes and isolate their effects on the microstructure of the object.

The OKMC model treats objects with defined centers of mass, which can be point defects or point defect clusters. Although atoms in regular lattice positions are not explicitly considered, objects can move within an underlying spatial grid that mimics the atomic lattice. An object can react against another (annihilation, aggregation, creation) with a frequency attached to each reaction [7].

5.4.1 OKMC Simulation Parameters

5.4.1.1 . Parametrization of reaction events

The parametrization describes some properties of the defects. The migration energies are associated with their attack frequencies for different jump directions. Jump, dissociation/emission, detrapping are considered as thermally activated processes, characterized by an activation energy $\mathrm{E_{a,n,i}}$ and an attempt frequency $v_{n,i}$. Their rates, for object n and event i are obtained as [157]:

$$\boldsymbol{\Gamma_{n,i} = v_{n,i}\exp\left\{-\frac{E_{a,n,i}}{kT}\right\}} \qquad 5.17$$

For the object jump, the activation energy is its migration energy, $\mathrm{E_m}$. For the emission from either a trap or an object, the most typical method is to take the activation energy E_a as the sum of the binding energy, E_b, of the escaping entity (e.g., that of a single vacancy or SIA from a cluster) and its migration energy, $\mathrm{E_m}$; $\mathrm{E_a = E_m + E_b}$.

Dissociation and emission events have an activation energy often taken to be equal to the sum of the migration energy E_m plus the binding energy between the emitted defect and a cluster of the size that remains after emission, E_b. The corresponding rate is [157]:

$$\boldsymbol{\Gamma_d = \nu_0 \exp\left(-\frac{E_m+E_b}{k_B T}\right)} \qquad 5.18$$

Regarding the reaction between defects, it is generally assumed that they are diffusion limited. That is, the reaction occurs as soon as the two objects are within a pre-defined capture radius, but no energy barrier is associated with the reaction. These events occur therefore only on the basis of geometrical considerations (overlap of reaction volumes) and do not participate in defining the progress of time.

In order to account for scattering anisotropy, directions parallel and perpendicular to the ⟨c⟩ direction are considered here. Table 5.1 and Table 5.2 identify and summarize, respectively, the simulation parameters available for the model. Objects of size n>1 are considered immobile. Although this assumption should have a significant impact on the microstructure, taking into account all mobilities still represents a challenge for OKMC simulations.

Table 5.1 details the parameter expressions used. The prefactor ν_n^{emis} is defined as the product between the prefactor $\nu_{n,\perp}$ and the number of sites available on the surface of the object. Each of the considered objects can emit a point defect of the same nature as the object. The activation energy for emission is defined as the sum of the binding energy and the migration energy (last hop theory). Finally, the recombination distances of the objects depend essentially on their morphologies (3D, loop ...).

Table 5.1: Expressions of OKMC simulation parameters

Parameters	
n	Size of the object in number of defects
$v_{n,\perp}$	Prefactor of the Arrhenius law characterizing the jumping frequency for the diffusion of objects of size n perpendicular to the c axis
$v_{n,\parallel}$	Prefactor of the Arrhenius law characterizing the jumping frequency for the diffusion of objects of size n parallel to the c axis
v_n^{emis}	Prefactor of the Arrhenius law characterizing the frequency of the jumping for the emission of a defect from a cluster of size n
$E_{n,\perp}^m$	Migration energy of objects of size n migrating in the directions perpendicular to the c-axis
$E_{n,\parallel}^m$	Migration energy of objects of size n migrating in directions parallel to the c axis
E_n^b	Binding energy between a point defect and a cluster of size n - 1
R_n	Physical radius of an object of size n

Table 5.2: Representation of available simulation parameters. The symbols ⊥ and ∥ indicate the directions perpendicular (base plane) and parallel to the direction (c), respectively.

n	$v_{n,\perp}$	$v_{n,\parallel}$	$E^m_{n,\perp}$	v^{emis}_n	$E^m_{n,\parallel}$	E^b_n	R_n
1	$v_{1,\perp}$	$v_{1,\parallel}$	$E^m_{1,\perp}$	v^{emis}_1	$E^m_{1,\parallel}$	E^b_1	R_1
-	-	-	-	-	$E^m_{1,\parallel}$	-	-
-	-	-	-	-	$E^m_{1,\parallel}$	-	-
-	=0 (immobility zone)			-	$E^m_{1,\parallel}$	-	-
-				-	$E^m_{1,\parallel}$	-	-
-				-	$E^m_{1,\parallel}$	-	-
-				-	$E^m_{1,\parallel}$	-	-
n				v^{emis}_n	$E^m_{1,\parallel}$	E^b_n	R_n

5.4.1.2 Implementation of cascade debris

Neutron irradiation is considered by inserting cascade debris as playing the role of defect source term. The debris represents the residual post-cascade defects. A cascade, which is a collection of objects along with their spatial distribution. To determine the insertion rate of cascades; Displacement per atom per cascade (*DPC*) is calculated as [162].

$$\mathbf{DPC} = \frac{\mathbf{v_{cas}}}{\mathbf{N_{at}}} \quad 5.19$$

Where v_{cas} is displacements per cascade (v_{cas} = 2x N_{fp} from MD simulations) and *Nat* is the number of atoms in the simulated volume. Since every PKA is responsible a single cascade event, DPCs were scaled using normalized fraction of recoils(f) at the PKA spectrum.

Accordingly, the cascade insertion rate is calculated with [162].

$$\mathbf{Rcas} = \mathbf{Dose\ rate}/\sum \boldsymbol{fDPC} \quad 5.20$$

5.5 Rate Theory

In response to thermal aging and irradiation, a material's mechanical and physical properties change due to the formation of clusters of point defects [163]. Understanding the different stages of cluster formation is essential to evaluating the changes that occur in the material. Based on the assumption of a random spatial distribution, rate theory can describe microstructure evolution in terms of cluster size distribution. In general, the term 'reaction rate theory' or 'rate equations' refers to solving continuum differential equations of defect densities to simulate their diffusion. From defect production in cascades to changes in macroscopic properties, the rate theory approach [138,164,165] has the advantage of covering a much wider time, spatial, and energy range.

Spatial and temporal correlations can be accounted for by KMC, but they cannot be accounted for by RT. In spite of this, its main limitation is the computational burden associated with the size of the simulation cell. The maximum dose and simulation cell size remain limited, even with modern computers [138]. According to Stoller et al [138], rate equations and KMCs each have advantages and limitations. Table 5.3 summarizes the major characteristics of these models.

Using rate theory, ordinary differential equations can be solved from the master equation. As a result, clusters of solute species such as point defects can be formed and evolved. The idea of RT is to replace a real system with a system that occurs continuously in time and space. This is assumed to be a uniform cluster distribution, in which all processes occur continuously.

Despite its computational efficiency, this method has some limitations. Radiation damage sources are averaged over time and space, and the microstructure is averaged spatially into an effective medium. Point defects and some cluster types are treated as irradiated in such rate equations.

Table 5.3: Comparison of reaction rate theory and object kinetic monte carlo methods

Treatment of Variable	Object Kinetic Monte Carlo	Rate Theory
Solution Method	Stochastic	Deterministic
Time	Inferred from possible processes	Explicit variable
Space	Full spatial dependence	Homogeneous effective medium
Defect production	Discrete in time and space	Time and space averaged
Sink strength	Inferred from fate of point defects	Explicit analytical expression
Defect of sink density	Computationally limited by simulation cell size	Essentially unlimited

Different approaches to solving differential equations for diffusion have been used under many names. Equation [52] provides the basis for RT modeling:

$$\frac{dC_j}{dt} = \sum_K w(k,j)C_k - \sum_K w(j,k)C_j + G_j - L_j \qquad 5.21$$

Where Cj is the concentration of cluster of type j, w(k,j) the transition rate per unit concentration of a cluster of type k to a cluster of type j, Gj the production rate of cluster of type j, and Lj is the loss rate of cluster of type j to all point defect sinks but point defect clusters.

These first and second terms represent the flux to and from the j cluster population. The third and fourth terms are production and sink terms, respectively. If j clusters

are mobile, they are produced in displacement cascades and lost to sinks. The rate coefficients of the kinetic reactions that participate in the flux control the first and second terms. By describing the rate coefficients, it is possible to derive both the physical production rate and the rate at which the defect clusters capture and emit point defects. Thermally activated motion of defects clusters, mutual impingement, and coalescence or annihilation reactions are just some of the processes that govern microstructure evolution. Additionally, nuclear transmutation and displacements or diffusion of preexisting impurities can result in microchemical changes.

6 Numerical Tools and Codes

6.1 Architecture of the Modelling Sequence

The architecture of the multiscale modelling sequence is sketched on Figure 6.1. The codes are accompanied by pre- and post-treatment scripts in order to link them up and transmit data. As seen in Figure 6.1, three steps are identified to modelling damage evolution in operating phase:

- the "primary damage" step treats the neutron spectrum to provide the PKA spectrum with the code SPECTER, see § 6.2.1. The essential inputs are the neutron Spectrum of fuel assemblies which is calculated by MCNP, local temperature and irradiation time. Another output is the determination of the dose rate. PKA spectrum will be divided to group average PKA energies and introduced to initiate a cascade simulation. The dose rate will be used in the defect cluster module when implementing neutron irradiation into the simulations.

- the "defect cascade" step mainly includes a molecular dynamics program, LAMMPS [166], see § 6.2.2., to simulate the evolution of the defect cascades for the average PKA energies. The raw outputs are then post-processed via OVITO [167] and MATLAB respectively , so as to that configuration of each cascade event is kept as a database regarding corresponding PKA spectrum. conducted via the LAMMPS module of the RWTH-HPC-Cluster. The required resources in terms of cores, memory, and time for submitting each simulation to the system were determined via Batch scripts. At the end of the simulation, LAMMPS outputs a text file containing the coordinates and energies of all particles in the simulation box, as well as any other parameters that were requested.

- the "defect cluster" step evaluates the long-term evolution of defect clusters and resulting radiation induced microstructures using KSOME [168] see § 6.2.4. Input parameters are introduced with databases. All possible reaction events that can occur in the simulation are specified in the Reaction event database. All jump rates regarding internal events (diffusion, disassociation etc.) are linked via Activated Event Database. Other essential parameters are introduced with Cascade Database and Capture Radius Database in which analytic expressions capture radii of defects. The size and density distribution of the defect clusters and thus the microstructure evaluation as a function of dose was carried for the desired irradiation time (years in case of operating conditions of a fuel assembly or hours in case of an experimental study).

At the “Post Processing” step, these raw outputs are then used in OVITO see § 6.2.3, which provides Wigner-Seitz modifier [169] to identify defects in the structure. In order to process simulations for each energy, a batch script was written and used in ovitos, a Python interpreter design to enable scripting of OVITO’s functions.

At long term evolution step, the python 3.8.3 language was used for theoretical model implementation. In detail, python library module (Scipy) is used to solve the simultaneous ordinary differential equation, i.e. master equation of the rate theory [170]. Generally, Scipy module is used to solve linear algebra, integration, special functions and image processing with efficient numerical routines.

6.2 Tools and Codes

6.2.1 SPECTER

SPECTER is a Fortran-based computer code developed by Lawrence R. Greenwood and Robert K. Smither at the Argonne National Laboratory in 1985 [141]. SPECTER is designed to use discretized neutron energies and fluxes in combination with catalogued interaction-specific displacement cross section data to generate a number of useful properties related to radiation damage including the displacement rate. SPECTER relies on the Binary Collision Approximation (BCA). It takes into account the elastic collisions as well as inelastic interactions and all

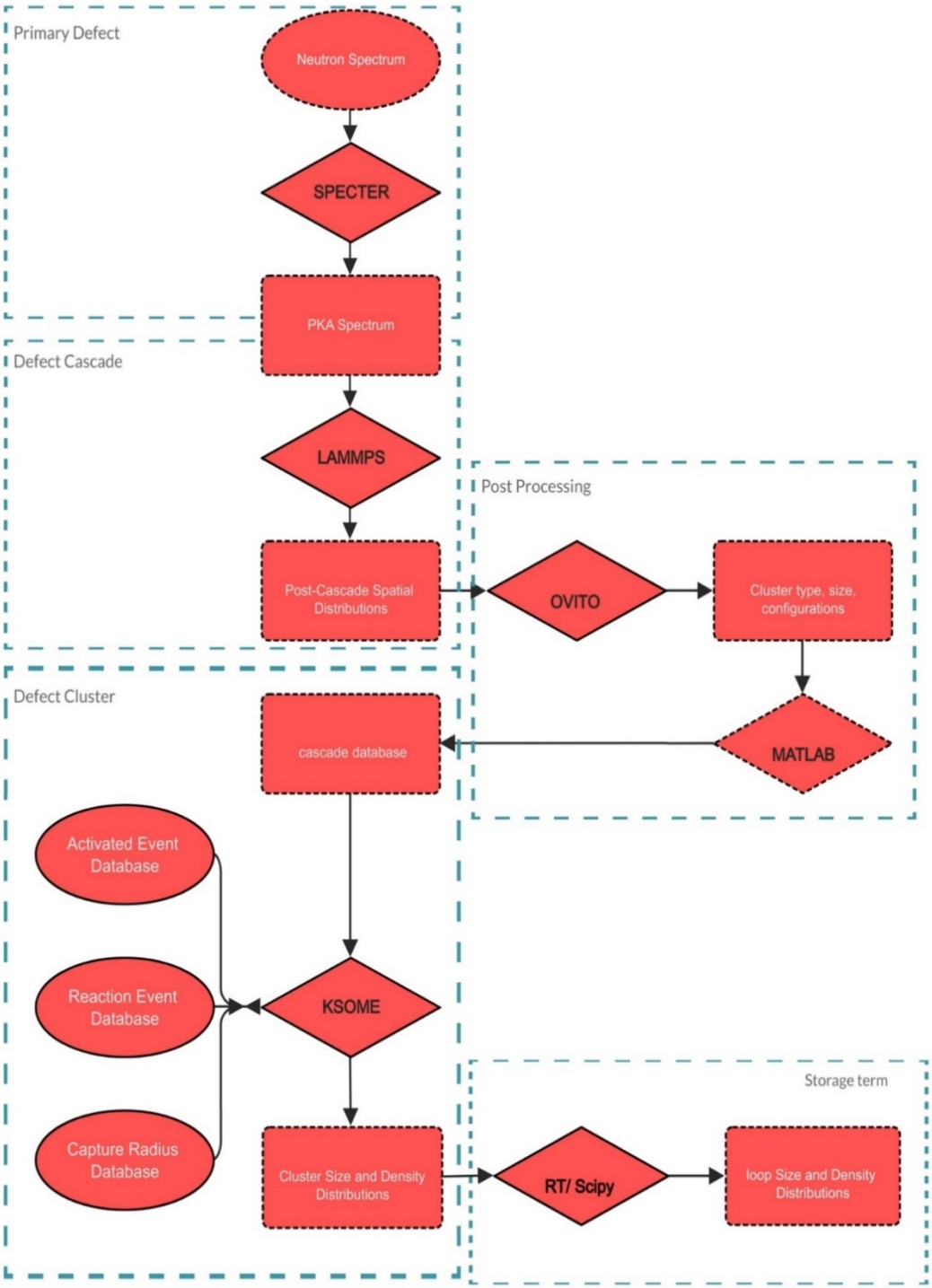

Figure 6.1: Multiscale modelling sequence

possible direct nuclear reactions, such as $(n,p),(n,\alpha),(n,2n)$ etc, between both kinds of particles. All these phenomena are characterized by differential neutron cross sections available from the Evaluated Nuclear Data File database (ENDF-V). ENDF data and their uncertainties can be obtained from the National Neutron Cross Section Center at Brookhaven National Laboratory (USA).

6.2.2 LAMMPS

This software is the most powerful MD software designed by Sandia National Laboratories, USA. LAMMPS is aimed for molecular dynamics which are governed by Newton's equations of motion. Earlier versions of LAMMPS were written in Fortran. The current version is written in C++ with MPI for parallel communication. LAMMPS has potentials for soft materials like (biomolecules, polymers) and solid-state materials (metals, semiconductors). This program enables us to perform simulations on computers with multiple processors in ways that significantly decreases the simulation time as the number of processors is increased [166].

A code file is needed to define the parameters for the material and simulation environment, and then give instructions on the type of simulated experiment to perform. A principal factor in between each calculation interval in which the force applied to each atom and velocities are calculated. The time steps are repeated until the chosen number of iterations is completed. In order to capture the fast motion of the atoms, a femtosecond (1015) time step is required. The procedure for writing an input script in LAMMPS is given through the following steps.

Step 1: Initialization

At the initial stage atomic positions and their respective lattice parameters are defined either by using FORTRAN program or by defining the lattice. LAMMPS contains various lattice structures such as fcc, hcp, square, diamond and also customized lattice parameters can be defined for complicated structures. The most common crystal structures and their lattice parameters can be obtained from literature.

Step 2: Potential

Potential defines the type of forces that are acting on neighboring atoms. The potential file must be defined properly so that the types of atoms are correctly assigned. Different potentials require different types of files to define the interaction between the atoms. LAMMPS contains various potentials for various elements, and they can be accessed on their website.

Step 3: Run and Timestep

Timestep command sets time step size for subsequent molecular dynamics simulations. Run command continues dynamics for a specified number of time steps.

Step 4: Boundary Conditions

The type of boundary conditions signifies the type of neighbors an atom possesses. A periodic boundary condition defines the same neighborhood for inner as well as outer atoms in all dimensions. A non-periodic in a particular dimension varies the type of neighborhood in that particular dimension.

Step 4: Computation

Computation command calculates various physical quantities like temperature, pressure mean square displacement and other parameters for a defined group of atoms. Quantities calculated by this command are instantaneous values i.e., the current information about a certain quantity is based on previously stored data. The computation obtained can be both for global and local group of atoms as defined in the program.

6.2.3 OVITO

The output or dump from LAMMPS is visualized using OVITO software. OVITO is a scientific data visualization and analysis software for large-scale atomistic simulations, in particular classical molecular dynamics (MD) [167]. OVITO is freely available under an opensource license for Windows, Linux and MacOS platforms. It is being developed by Alexander Stukowski at the Material Science Department at Darmstadt University of Technology, Germany. The type of analysis apart from visualization is the Bond Angle Analysis and Common Neighbor Analysis [171]. The Bond Angle Analysis which gives the type of bond formed

between two local neighbor atoms using Auckland-Jones bond angle method and also Common Neighbor Analysis (CNA) which shows type of crystal structure environment like FCC, BCC, and HCP etc.

6.2.4 KSOME

KSOME [168,172] is a flexible and computationally efficient lattice-based OKMC code to simulate the long-time scale evolution of a microstructure under irradiation. Patterned after the original FORTRAN code ALSOME, KSOME is significantly more sophisticated, faster, and flexible. Objects of interest include vacancies, self-interstitial atoms (SIA), interstitial impurities and clusters of these defects produced during irradiation. KSOME keeps track of the locations (more precisely their center of mass) of these objects (defects) in time. Objects or defects are characterized by their type, size, shape, position, and orientation.

In principle, the KSOME code also allows for the inclusion of extended defects such as dislocations and grain boundaries, which it presently treats as unsaturable sinks, such that any defect that is absorbed by a sink is removed from the simulation box. Free surfaces are treated as absorbing boundaries, which also act as sinks. KSOME does not have dedicated subroutines to deal with each individual type of defect, rather it is designed such that all the necessary information regarding the properties of defects such as type, size, location, orientation, anisotropy, and their diffusion–reaction processes, along with simulation parameters regarding the simulation box size, temperature, and boundary conditions, are provided via text-based input files. Correspondingly, as additional information is needed and available, KSOME can be used to carry out very detailed OKMC simulations with only minimal additional work required to modify the diffusion and reaction event databases. As with all KMC approaches, much valuable information about the evolutionary path of a given system can often be obtained by determining its sensitivity to the deliberate variation of input parameter values which is easily accomplished with KSOME.

6.2.5 RT/Scipy

Generally, Scipy module is used to solve linear algebra, integration, special functions and image processing with efficient numerical routines. Among the various modules in Scipy, the scipy.integrate.odient is numerical integrate a system

of ordinary differential equations in Scipy routines. From this system, the defect concentration could be integrated by numerical method. To adopt the scipy.integrate.odient, time step function should be defined. In scipy.integrate.odient, integration time step is defined as “array” in python. Hence in this study, time step was defined by using “for” statement. Interval of time was given as 0.25 (0.25, 0.50, 0.75…). The region of time was defined as the related phase time.

7 Method and Parametrization

7.1 Radiation in Microstructure Evolution After Operating Condition

7.1.1 Neutronic Damage Calculation

The procedure, which was followed in this section, is schematized in Figure 7.1. In order to see the primary effect of neutron field on fuel assemblies, the starting point is a full core simulation carried out by using Monte Carlo code MCNP to locate the fuel assemblies and extract the exact neutron-energy spectrum. Then SPECTER code treats the neutron spectrum to provide the PKA spectrum of fuel cladding material. The neutron spectrums are defined as 100 energy groups; all neutrons belonging to the same group are considered to have the same energy. SPECTER code employs the data set as the input to calculate displacement cross sections of Zr to make an analogy of Zircaloy. Generated displacement cross section per energy group is folded with fluxes of related energy group to calculate dose rate which is one of the crucial input parameters while investigating the microstructure evolution.

7.1.1.1 Input parameters

A normalized neutron spectrum in Figure 7.2 where a neutron spectrum for a fuel assembly of a 3.8 GW (gigawatts of thermal power) PWR reactor in Paluel, France was used as essential input to represent the operating conditions of an LWR. The spectrum is plotted as flux per unit lethargy, which simply means neutron energy times neutron flux. Total flux of the spectrum is 6.26×10^{13} n/cm^{2}s. To be able to investigate the effect of neutron field in experimental studies, an HFIR spectrum was also employed. Figure 7.3 shows the neutron spectrum at the core horizontal midplane with Oak Ridge HFIR operating at 85MW. Total flux of the spectrum is 5.10×10^{15} n/cm^{2}s.

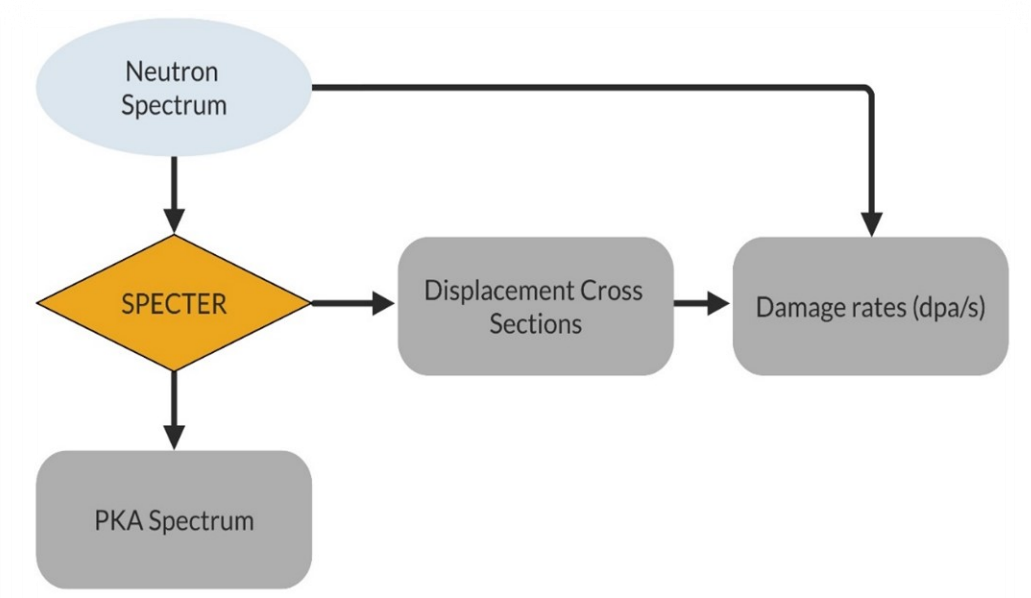

Figure 7.1: Determination of PKA spectrum

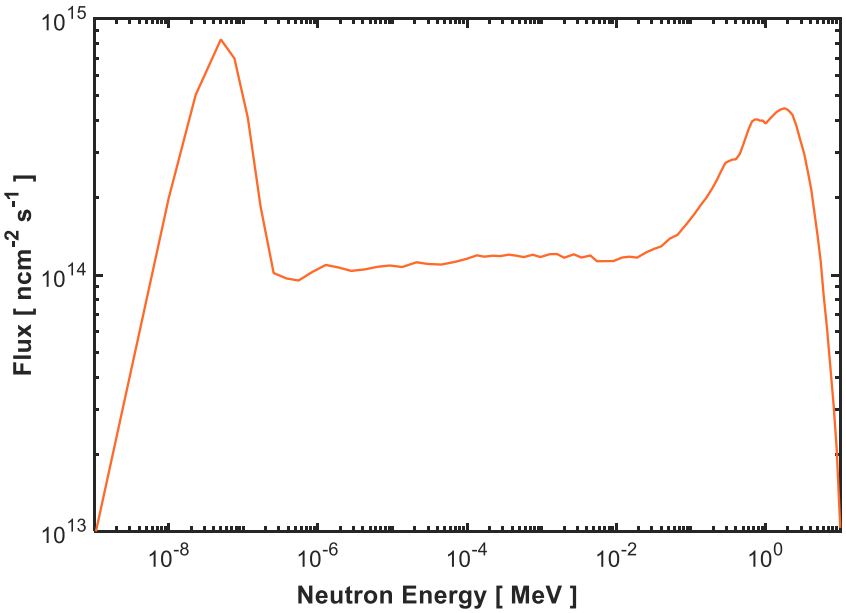

Figure 7.2: (709 groups) average neutron spectrum in the fuel assembly of a PWR (a fuel assembly of a 3.8 GW LWR-P4 reactor in Paluel, France)

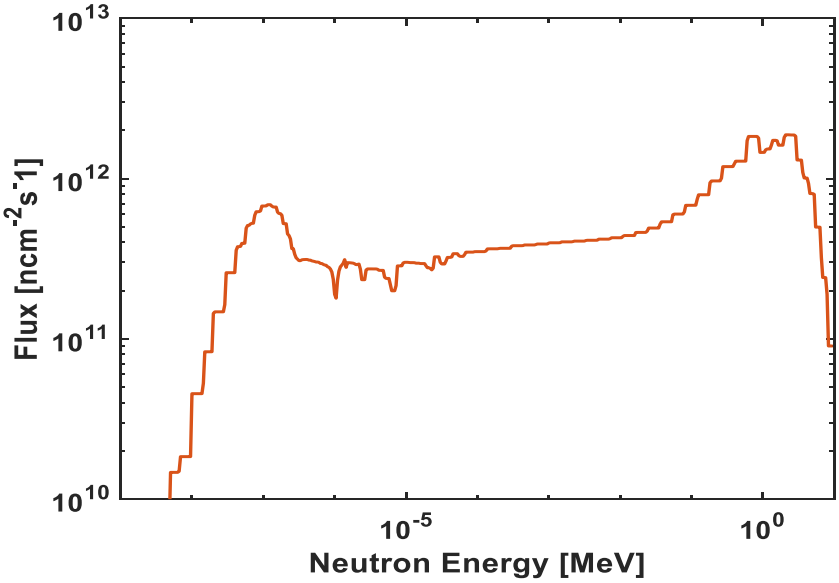

Figure 7.3: (100 groups) average neutron spectrum at the core horizontal midplane with Oak Ridge HFIR operating at 85MW

7.1.2 MD simulation of Defect Cascades

The procedure that was followed in this section can be seen in Figure 7.4, which diagrammatizes how it was accomplished. Generation of defect cascade by a Primary Knock-On Atom (PKA) and obtaining primary damage defect configuration via Molecular Dynamics method was undertaken. Since the morphology of the primary radiation damage is an important factor in determining the subsequent thermal evolution of defects, obtaining correct predictions of the structure of cascade debris was intended.

Regarding different PKA energies, direction and irradiation temperature, mass simulations are conducted, and the outputs are spatial distributions of defect cascades evolved. These raw outputs are then used in OVITO which provides Wigner-Seitz modifier to identify defects in the structure. In order to process simulations for each energy, a batch script was written and used in ovitos, a Python interpreter design to enable scripting of OVITO's functions. The batch script does the following:

1. Using imported data, it performs a Wigner-Seitz Analysis. At this step, the data of initial configuration (belongs to the initial state) is compared with

the data of final configuration belongs to the final state) to find the interstitials and nearest neighbors to the vacancies in the crystal. Since the atoms are vibrating around their lattice position the atom displaced greater than 1 Å was regarded as “displaced” atom.

2. The analysis outputs are exported to a text file. Simulation id, number and coordinates of vacancy and interstitials are the information that is kept in the text file.

3. The configuration of each cluster (coordinates of center of mass) was kept with size and type configurations and rewritten to the cascade files where they belong. This procedure was performed by MATLAB.

The configuration of each cascade event is kept as a database regarding corresponding PKA spectrum.

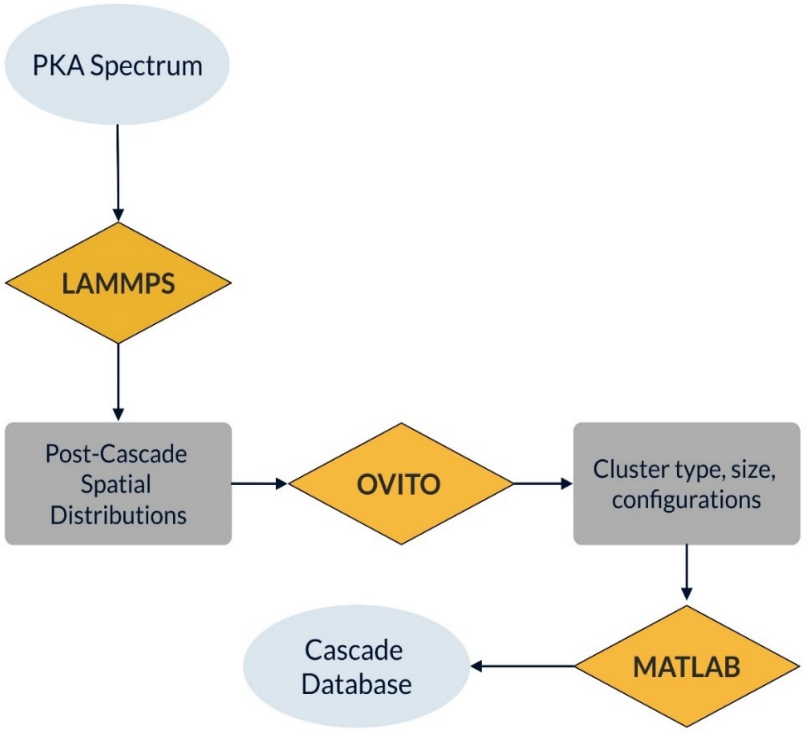

Figure 7.4: Determination of defect cascade

7.1.2.1 Selection of interatomic potential

The first thing that should be done when setting up a molecular dynamic simulation is verifying the potential. In this work, the embedded atom method (EAM) #3 potential for hcp Zr developed by Mendelev and Ackland [173] was used. Generally, atomic cascades and irradiation simulations require the use of the repulsive ZBL potential or similar. Since the potential is already in a screened coulomb potential form at short distance which can reliably model high-energy collisions, ZBL potential was not connected. Since this potential is part of the openKIM potential library [174], it has been subject to the standard potential tests. The result for 0° K lattice parameters and the cohesive energy for the hcp structure are shown in Table 7.1. To determine the lattice constants and the cohesive energy for non-zero temperature, an energy minimization study with 6400 atoms is performed. During simulations, NPT ensemble was used to equilibrate the simulation to temperatures of 0, 10, 300, 600° K and a pressure of 0 bar. As Table 7.1 shows the lattice constant c increases with increasing temperature while the lattice constantly decreases at low temperatures and increases as temperatures increase again.

Table 7.1: Calculated Lattice Parameters with (EAM) #3 potential

Mendelev 2007 v3	**a [Å]**	**c [Å]**	**Cohesive Energy [eV/atom]**
0°K (openKiM)	3.234	5.168	6.635
0°K (calculated)	3.234	5.168	6.635
10°K (calculated)	3.234	5.168	6.633
300°K (calculated)	3.230	5.176	6.595
600°K (calculated)	3.234	5.184	6.554

7.1.3 OKMC Simulation of Defect Cluster

Long-term evolution of defect clusters and radiation induced microstructures is simulated using KSOME OKMC code for simulating long-time scale evolution of a microstructure.

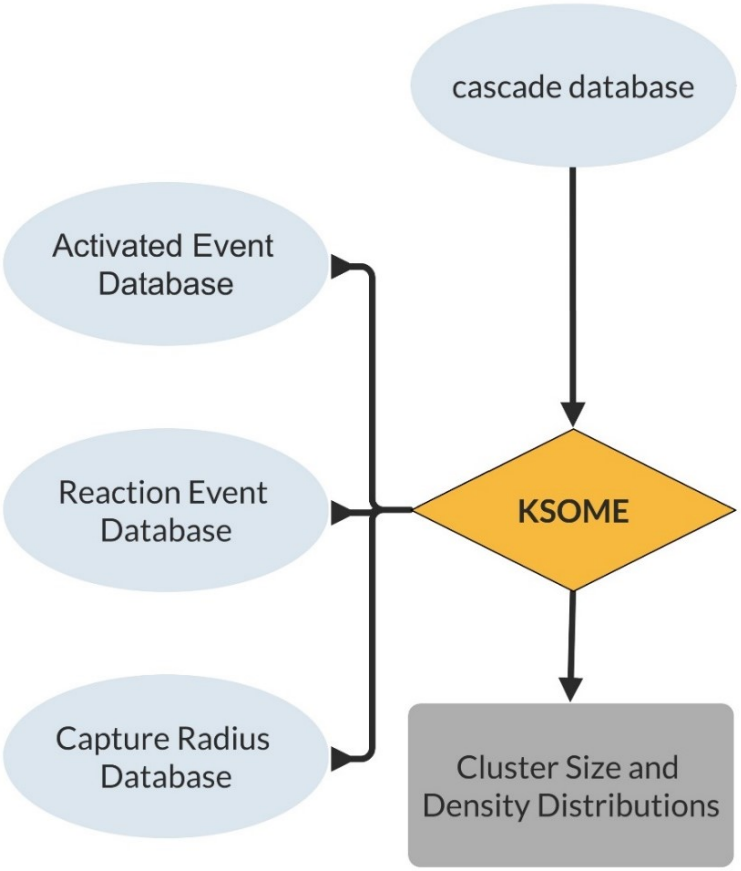

Figure 7.5: Simulation of defect clusters

Input parameters are introduced with databases. All possible reaction events that can occur in the simulation are specified in the Reaction Event Database. All jump rates regarding internal events (diffusion, disassociation etc.) are linked via Activated Event Database. Other essential parameters are introduced with cascade database Capture Radius Database in which analytic expressions for capture radii of defects are carried. The size and density distribution of the defect clusters and thus the microstructure evaluation as a function of dose was carried for the desired

irradiation time (years in case of operating conditions of a fuel assembly or hours in case of an experimental study). Figure 7.5 diagrammatizes defect cluster simulations procedure.

There have been two parameterizations developed: a so-called "reference" parameterization based on our most recent calculations and simulation results from the literature, and an "optimized" parameterization based on experimental results. The detailed description of the model used as well as the assumptions taken and their translation into model parameters will be discussed here.

7.1.3.1 Simulated volume and modelled defects

The model is carried out to examine damage accumulations in polycrystalline bulk zirconium in which simulated volume is located at the center of a spherical grain. Modeled defects are directional depending on the cubic grid based on the hcp lattice. The following approach is used to describe diffusion anisotropy phenomena in simulated volumes. The hcp simulation cell is considered to be a stack of 2D triangular lattices with a_0 along the basal plane and c/2 along the c-axis. Within a given “D-plane, if x and y are the integer coordinates of an object on the square lattice then the corresponding coordinates in the triangular lattice are given as

$$x_{real} = a_0\left(x + \frac{y}{2}\right)$$

$$y_{real} = a_0\left(\frac{\sqrt{3}}{2}y\right) \qquad 7.1$$

For a microstructure evolution simulation of Zircaloy, the following defect types are modeled:

1. Point defects (vacancies and self-interstitials), interstitial clusters and vacancy clusters are considered.

2. all SIA clusters are assumed to be <a> loops, and the merging of two SIA clusters results immediately in the formation of a single larger <a> loop. SIA clusters can diffuse 3D corresponding to the 6 equivalent directions in the basal plane. SIA clusters larger than size 20 were constrained to diffuse in 1D since <a> loops tend to align in rows parallel to the basal plane [175].

3. Since <a> loops can be also formed by vacancy clusters; same assumption is valid for vacancy clusters. But in order to define vacancy loops with c component, vacancy clusters can diffuse 3D regardless of their size. Significantly, the diameter of the <c> loops observed in experiments, are all larger than 10 nm, which is much larger than the diameter of the <a> loops [63,68,176]. Taking this into consideration, it is assumed that loops form when vacancy clusters collapse at 400 vacancies.

Impurities are not treated discretely but in order to produce experimentally comparable results for validation purposes, the following is applied :Nominal composition of Zircaloy-4 of the experimental reference [73] can be seen in Table 3.1. The highest amount of alloying elements is Tin which acts as a good trap for interstitials and for vacancies [83]. From ab inito calculations it is known that in Zr −Sn alloys Sn additions are able to localize vacancy clusters nearby playing a role of traps for vacancy clusters. Accordingly, to implement the effect of alloying element on damage accumulation, Sn is not treated discretely but in terms of concentration. Immobile Small interstitial clusters (<4) are randomly distributed and defined as traps for vacancy clusters in accordance with the concentration (1.14 % atomic) of Sn.

7.1.3.2 Considered events

The simulation contains several internal and external events with a certain probability defined by the frequency of occurrence. Figure 7.6 presents the events considered. The defects can be subjected to 4 types of internal events described below:

i- The defects can jump to one of the neighboring sites. The mobility of the defect (e.g., interstitial or vacancy cluster) is governed by hoping rates.

ii- Two defects can recombine. Recombination results in a larger defect if they are of the same type (vacancy or interstitial). When they are of different types (vacancy and interstitial), recombination results in a smaller defect of the same type as the defect. Finally, when the defect is different in type but the same in size, they annihilate one another.

iii- The defects can dissociate or emit by the emission of a vacancy or interstitial.

iv- The defects can be trapped by defects or grain boundaries.

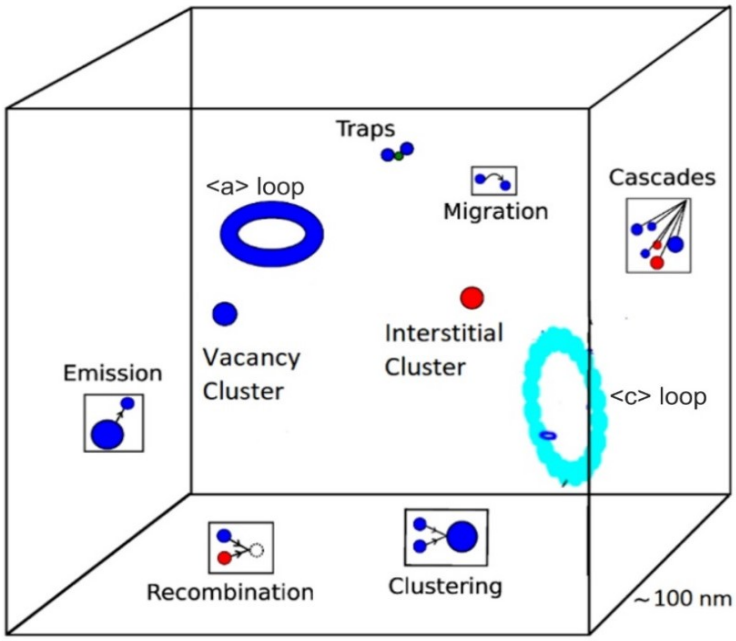

Figure 7.6: Internal and external events involved in the model

The external event in our model is insertion of the cascade debris. The cascade debris is selected randomly from the database and inserted into the simulation cell at random positions at a rate corresponding to a particular dose rate. The cascade database contains 3000 cascade events at PKA energies between 1-65 keV at temperatures 573°K, 630°K, 673°K. During a simulation in order to mimic the PKA spectrum associated with a given reactor, cascade insertion rate was calculated using normalized fraction of PKAs (f) at the PKA spectrum.

7.1.3.3 Kinetic parameters

The following parameters are used in this work: pre-exponential attempt frequency Va; interstitial and vacancy migration energies, the values of the defect binding energies and other related kinetic parameters were taken from references in Table

7.2. The migration/diffusion rates of clusters vary with cluster size (n). In OKMC simulations defects are treated as point objects with a capture radius or reaction distance. This is the distance at which a defect interacts with other defects. If the capture radii of two defects overlap, then defects are allowed to coalesce or recombine depending on their type. Also, when a defect emits from a cluster it is placed outside this capture radius. Capture radius is a function of type and size of a defect and the formula were obtained from Ref. [177]. Due to lack of specific information about lattice distortion associated with the type and shape of a defect, it is assumed that the medium is homogenous and continuous, and that the interaction radius of the defects involved are isotropic. The detailed descriptions of all other kinetic parameters used in the present simulation are provided in Table 7.2.

Table 7.2: Kinetic Parameters

Parameter	**Vacancy**	**Interstitial**
$V_a \perp$ [s^{-1}]	5.62 x 10^{13} [[178]	3.35 x 10^{11} [179]
$V_a \parallel$ [s^{-1}]	7.82 x 10^{13} [180]	7.49 x 10^{11} [179]
$V_n^{emission}$ [s^{-1}]	$V_n^{emission} = V_a \perp$ x $n^{2/3}$ [177]	$V_n^{emission} = V_a \perp$ x $n^{1/2}$ [176]
$E^{migration} \perp$ [eV]	0.55 [180]	0.23 [180]
$E^{migration} \parallel$ [eV]	0.66 [180]	0.26 [180]
$E_n^{emission}$ [eV]	$E_n^{emission} = E_n^{binding} + E_{migration} \perp$	
Capture Radius R	<a> loop $(\frac{n3V_{at}}{4\pi})^{\frac{1}{3}}$ [177] <c> loop $(\frac{na^2\sqrt{3}}{4\pi})^{\frac{1}{2}}$ [177]	
Recombination radius [Å]	5 [46]	5 [46]

The hoping rates were adjusted accordingly to keep the diffusivities the same as in an hcp lattice. Then the vacancy diffusivity (D in $Å/s$) is given as

$$\boldsymbol{D = \frac{1}{6} z l^2 \Gamma} \qquad 7.2$$

where z and l number of nearest neighbors and hop length, respectively. The diffusivities along the c-axis ($D_{\|}$) and along the basal plane ($D_{\perp}$) are

$$\boldsymbol{D_{\|} = \frac{3}{4} c^2 \Gamma_{\|}} \quad 7.3$$

$$\boldsymbol{D_{\perp} = \frac{1}{2} a_0{}^2 (3\Gamma_{\perp} + \Gamma_{\|})} \quad 7.4$$

where, $\Gamma_{\perp}$ is hoping rate along the six individual directions along the basal plane and $\Gamma_{\|}$ is hoping rate along the two directions along the c-axis.

7.2 Radiation Induced Microstructure Evolution in Storage Phase

It is indeed possible to use cluster dynamics models to compute the recovery of loops during a heat treatment by choosing the production rate of point defects and point defect clusters (source term) equals to zero with the condition of that initial microstructure has to be in good agreement with the TEM observations of the as-irradiated microstructure [181] From that point, application of rate equations for the storage period (our variable is temperature and parameters related to it) may bring an explanation. The rate equation model assumes that the mechanisms take place homogeneously in the material whereas defects creation in displacement cascade during irradiation is heterogeneous [138]. On the contrary, thermal process occurs homogeneously inside the crystal grains and is therefore better suited to be modelled by the rate theory model.

Storage case is described by reducing some terms on the model. With respect to temperature conditions of all phases of procedure, all related parameters are updated. Then the effect of resulted defect concentrations on macroscopic behavior is assessed in terms of yield strength and elongation.

Accordingly, for describing long-term conditions following assumption was made:

Phase 0: Discharge-wet storage: 5 years, 50° C

Phase 1: Drying process: 110h, 250° C

Phase 2: First years of dry storage: 10 years, 300° C

Phase 3: End of licensing: 40 years, 200° C

Phase 4: Desired period: 60 years, 150° C

7.2.1 Model Description of Defect Evolution

The anisotropic model [182] is used by taking into account the effect of the orientation of the loops with respect to the <a> and <c> axis into the efficiency factor for absorption of point defects by loops. The system is seen on basal plane as a gas of clusters that can be either vacancies or interstitials within a single crystal grain of the polycrystalline metal. However, the mechanical interactions between the grains are neglected in this model. The dislocation loop sink strength was time dependent while dislocation line and grain boundary are constant. The original model of Choi [183] is described as below.

For single crystal

$$\frac{dC_{sv}}{dt} = K_o - K_{iv}C_iC_v - \rho_{ilp}Z^v_{ilp}C_vD_v - \rho_{vlb}Z^v_{vlb}C_vD_v - \rho_{dp}Z^v_{dp}C_vD_v - \rho_{db}Z^v_{db}C_vD_v \quad 7.5$$

$$\frac{dC_{si}}{dt} = K_o - K_{iv}C_iC_v - \rho_{ilp}Z^i_{ilp}C_iD_i - \rho_{vlb}Z^v_{vlb}C_iD_i - \rho_{dp}Z^i_{dp}C_iD_i - \rho_{db}Z^i_{db}C_iD_i \quad 7.6$$

$$\rho = \rho_{dp} + \rho_{db} + 2\pi r_v N_v + 2\pi r_i N_i \quad 7.7$$

$$r_v = \sqrt{(S_v/\pi b N_v)} \quad 7.8$$

$$\dot{S}_v = 2\pi r_v N_v (D_v C_v - D_i C_i) \quad 7.9$$

Where Ko is defect generation rate. Kiv is recombination rate which mean vacancy and SIA are combined. ρilp, ρdp, ρvlb, ρdb are each defect sink density. The bias factor is also referred to as capture efficient factor because this factor physically determines how many defects are absorbed to the sink density. $Zilpi$ and $Zilpv$ are SIA and vacancy bias factor of SIA loop, $Zdpi$ and $Zdpv$ are SIA and vacancy bias factor of dislocation line, $Zvlbi$ and $Zvlbv$ are SIA and vacancy bias factor of vacancy loop, $Zdbi$ and $Zdbv$ are SIA and vacancy bias factor of dislocation line.

Csi and Csv are defect concentration of SIA and vacancy in single crystal matrix, Di and Dv are diffusion coefficient in the matrix. ρ is about to total dislocation loop and line density. The dislocation line is assumed to be constant; dislocation loop is assumed time dependent parameter. The rv and ri are dislocation loop radius of vacancy and interstitial and Nv and Ni are dislocation loop number density of vacancy and SIA. For polycrystal

$$\frac{dC_{pv}}{dt} = \frac{dC_{sv}}{dt} - k_{gp}^2 Z_{gp}^v C_v D_v - k_{gp}^2 Z_{gb}^v C_v D_v \quad 7.10$$

$$\frac{dC_{pi}}{dt} = \frac{dC_{si}}{dt} - k_{gp}^2 Z_{gp}^i C_i D_i - k_{gb}^2 Z_{gb}^i C_i D_i \quad 7.11$$

$$k_{gb}^2 = 6 \times \sqrt{\rho} \div d_{gb} \quad 7.12$$

where Cpi and Cpv is defect concentration of SIA and vacancy in polycrystalline matrix. k_{gp}^2 and k_{gp}^2 are grain boundary sink strength. Z_{gp}^i and Z_{gp}^v are SIA and vacancy bias factor of grain boundary in prism. Z_{gb}^i and Z_{gb}^v are SIA and vacancy bias factor of grain boundary in basal plane.

7.2.2 Simplifications for the Storage Case

To describe storage conditions and regarding the type of defects which has been obtained from OKMC, some terms are needed to simplify. Accordingly, defect generation rate and dislocation line dependent terms are removed. In order to give initial values for the time dependent integration, cluster densities are transformed into corresponding point defect densities while calculating sink strengths. After operating phase, resulted defect structures in simulated cell are presented in Table 7.3.

Since c loops were not observed at the fluence reached in 2 years operation, the sink strength of this parameter is given as zero. A detailed list of parameters can be seen in Table 7.4.

Table 7.3: Defect Size and Densities After 2 Years Operation

	Cluster Density (object density)(m^{-3})	Point Defect Equivalent(m^{-3})	Loop Number Density(m^{-3})	Loop Size(nm)
Vacancy	4.88×10^{23}	9.76×10^{25}	3.05×10^{22}	11.25
Interstitial	8.45×10^{21}	4.22×10^{23}	5.274×10^{19}	1.96

Table 7.4: Parameter List

Parameters				323K (Wet storage)	523K (Drying process)	573K (The first 10 years at dry storage)	473K (40 years at dry storage)	423K (60 years at dry storage)
Diffusion coefficient of vacancy $\overline{D} = (D_{\parallel}^2 D_{\perp})^{1/3}$ **[184]** $\overline{D_v} exp(\frac{-0.9eV}{k_b T})$	**Basal plane**	$D_{\perp}$ [$cm^2 s^{-1}$]	8.16×10^{-9} [181]	5.93×10^{-23}	1.39×10^{-17}	7.94×10^{-17}	1.64×10^{-18}	1.24×10^{-19}
	Prism plane	$D_{\parallel}$ [$cm^2 s^{-1}$]	5.87×10^{-9} [181]					
Diffusion coefficient of interstitial $\overline{D_i} exp(\frac{-0.1eV}{k_b T})$	**Basal plane**	$D_{\perp}$ [$cm^2 s^{-1}$]	4.7×10^{-6} [138]	1.06×10^{-7}	4.19×10^{-7}	5.09×10^{-7}	3.32×10^{-7}	2.48×10^{-7}
	Prism plane	$D_{\parallel}$ [$cm^2 s^{-1}$]	3.5×10^{-6} [138]					
Burgers vector			b [cm^{-2}]	3.23×10^{-8}				
Defect generation rate			G [$dpas^{-1}$]	0				
Recombination radius			r_{iv} [cm]	10^{-7} [185]				
Sink Strength	**<a> SIA loop**		ρilp [cm^{-2}]	6.49×10^{7}	$2\pi r_i N_i$			
	<a> V loop		ρvlp [cm^{-2}]	2.15×10^{11}	$2\pi r_v N_v$			
	<c> V loop		ρvlb [cm^{-2}]	-	$2\pi r_v N_v$			
	<a> dislocation line		ρdp [cm^{-2}]	-				7.25×10^{6} [186]
	<c> dislocation line		ρdb [cm^{-2}]	-				2.25×10^{6} [186]
	<a> GB		$k_{GB}/2$ [cm^{-2}]	$6\sqrt{\rho/d_{gb}}$				
	<c> GB		$k_{GB}/2$ [cm^{-2}]	$6\sqrt{\rho/d_{gb}}$				
Bias Factor	**<a> SIA loop**		Zilp	1.56				
	<a> V loop		Zvlp	0.586				
	<c> V loop		Zvlb	0.586				
	<a> dislocation line		Zidp	1.56				
	<c> dislocation line		Zidb	0.586				
	<a> GB		Zigb	1.56				
	<c> GB		Zvgb	0.586				

8 Results

8.1 Results of Multiscale Simulations

8.1.1 Primary Defects (SPECTER)

The calculations lead to the following results. the PKA spectrum (number of PKAs expressed as a function of PKA's recoil energy) in which PKAs are classified and counted with respect to energy groups. Data of normalized PKA spectrum for the PWR generated by SPECTER is shown in Figure 8.1. The evaluated time period is 2 years. The average PKA energy of the total spectrum is 9.49 keV. The contribution of low energy recoils to the total displacement damage is almost negligible when compared to the contribution of higher energy recoils (due to higher energy neutrons) to the total displacement damage.

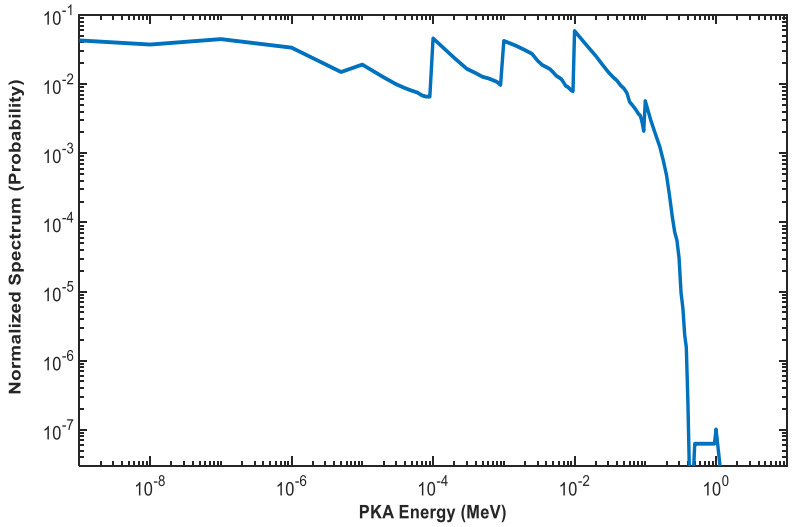

Figure 8.1: (100 groups) The normalized PKA spectra for the PWR case

The effect of Irradiation time on PKA spectrum was evaluated through the calculations with the HFIR spectrum for 477h, 2806.5h and 9916.6h. The evaluated time are dependent on the experimental conditions of the related study which will be the subject of the further evaluations (see section 6). Figure 8.2 shows the

normalized PKA spectrums for the HIFR case as a function of time. It is clear that changing the total fluence has no effect on the PKA spectrum.

Table 8.1: Calculated parameters from SPECTER

	Fluence [n/cm^2]	**Displacement per Atom [dpa]**	**Average PKA Energy [keV]**
2yrs at PWR	3.89 x 10^{21}	1.99	9.49
477h at HFIR	8.77 x 10^{21}	1.76	4.20
2806.5h at HFIR	5.15 x 10^{22}	10.3	4.20
9916.6h at HFIR	1.82 x 10^{23}	36.5	4.20

Effect of the total PKA energy averages of each case is given in Table 8.1. The average PKA energy also does not alter. As a result, the PKA spectrum is not affected by irradiation time.

Damage calculation was performed for dose rate which is an important factor in the next steps. Damage in terms of dpa is also given in Table 8.1. When PWR and HFIR cases are considered together, it is clearly seen that the most effective factor in the damage is total flux.

For the subsequent calculations, all the PKAs belonging to the same group are considered as dissipating the same energy, i.e., the middle group energy. PKA spectrum will be divided to group average PKA energies and introduced to initiate a cascade simulation.

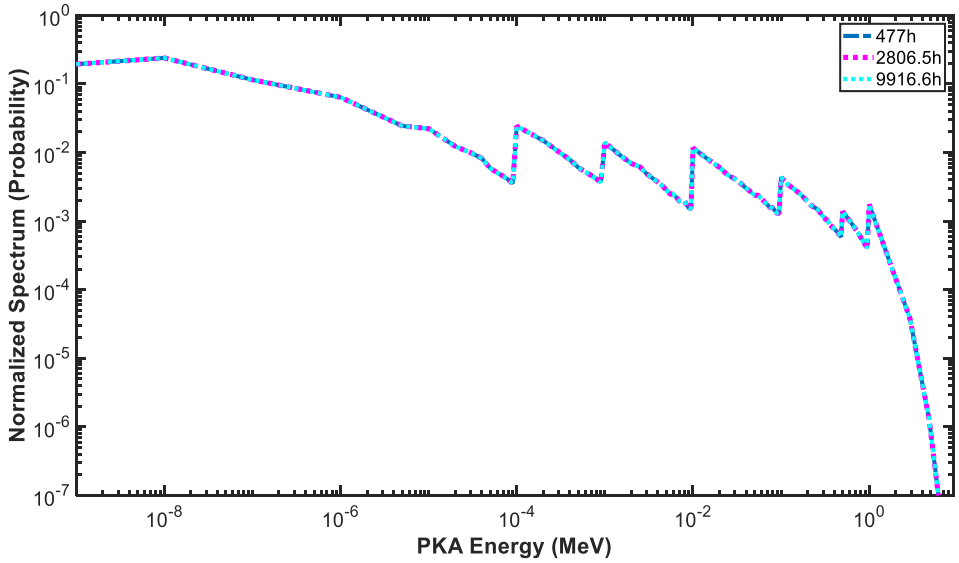

Figure 8.2: (100 groups) The normalized PKA spectrums at different irradiation time for the HFIR cases

8.1.2 Defect Cascade (MD)

Hcp unit cells are generated under periodic boundary conditions in x, y, and z directions. Before initiating the displacement cascade, the system is equilibrated in an NPT ensemble for 2 picoseconds (ps). Then, the displacement cascade is launched in an NVE ensemble for 50 ps, enough time for the system to reach thermal equilibrium. The outermost atomic layer is used as thermostat in order to extract heat produced by the displacement cascade: the temperature of the outermost atomic layer is rescaled to a constant temperature. To obtain average results dependence on simulated time from different cascades under the same conditions, a different strategy of timestep setting is applied during the displacement cascades simulations. The timestep must be carefully monitored in order to keep the total energy constant. It is usually taken to be of the order of 10^{-17} s and can be increased to 10^{-15} s during the cooling down of the cascade [120]. Regarding this, the timestep is set as 0.01, 0.1 and 1 fs in the range of 0.1ps, 1ps steps and 50 ps after the PKA was generated, atoms in the system will not move more than 0.05 Å in one step.

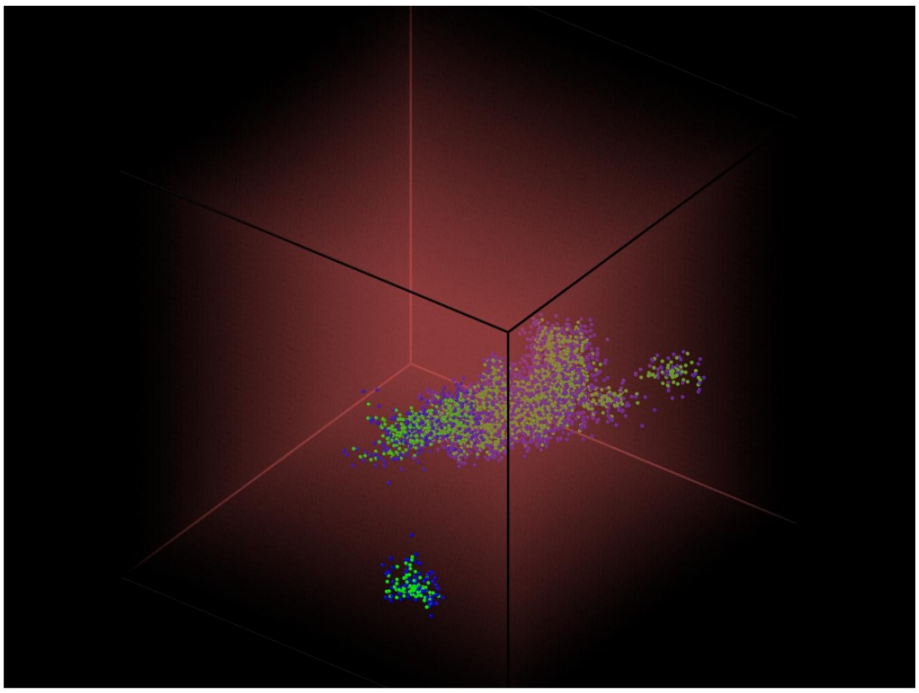

Figure 8.3: Cascade spatial distribution for a 20 keV PKA in Zirconium at 0.78 ps

One atom is randomly chosen from a 3 Å-thick spherical shell located at the center of the box as the PKA, and according to PKA energy, velocity is given toward the center to initiate a displacement cascade. Simulation boxes are arranged for related PKA energies. Cascades are visually inspected to check for self-interference; in addition, test runs were performed with larger boxes to make sure the number of defects seen was representative of a cascade in an infinite medium. Since the PKA is launched in random direction and secondary cascades can take any random direction, the simulation box size is taken to be around 2.5 times the expected range of the PKA. The expected range is found by initial scoping runs. As the PKA was randomly chosen and its velocity direction was also random, sometimes the PKA could pass through a boundary and re-enter the box from the opposite side, which made the final configuration quite unreasonable as presented Figure 8.3. To avoid this case, if an energetic particle reached the border regions, that simulation was abandoned.

8.1.2.1 Time evolution and spatial distribution of cascades

During cascade simulations, vacancies and interstitials are created in equal numbers and the number of point defects increases sharply until a peak value is reached. Cascade configurations during peak time are presented in Figure 8.4 for different PKA energies. A great deal of the Frenkel pairs which were seen after peak times (After Heat Spike), and vacancies are more likely to be created near the center of the cascades, however, interstitials tend to distribute around the outer regions of the displacement spikes. For 5 keV, energy of PKA is limited so that no cascade branches out. the cascade keeps compact at the peak damage of 5keV PKA. The sub cascade formation can be seen clearly for 22 keV PKA. At the cascade configuration of 65keV PKA, connected fragments into separated parts during the peak time are prominent.

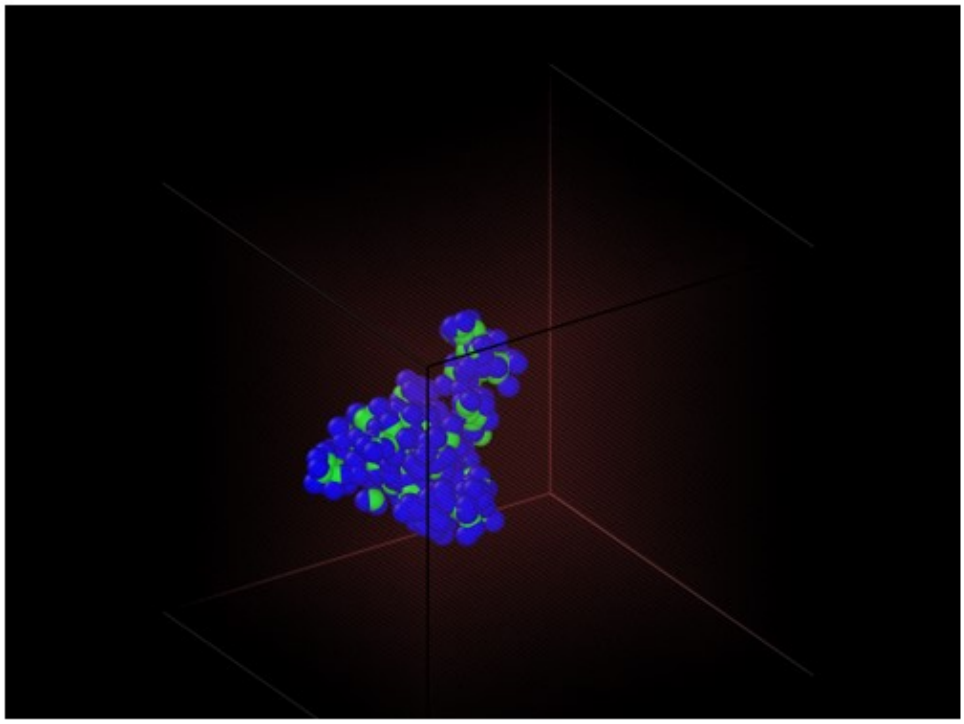

Simulation Box size [Å3]			Pka Energy	Number of	@
x	y	z	[keV]	Frenkel Pair	
517.44	518.05	518.39	5	84	0.6 ps

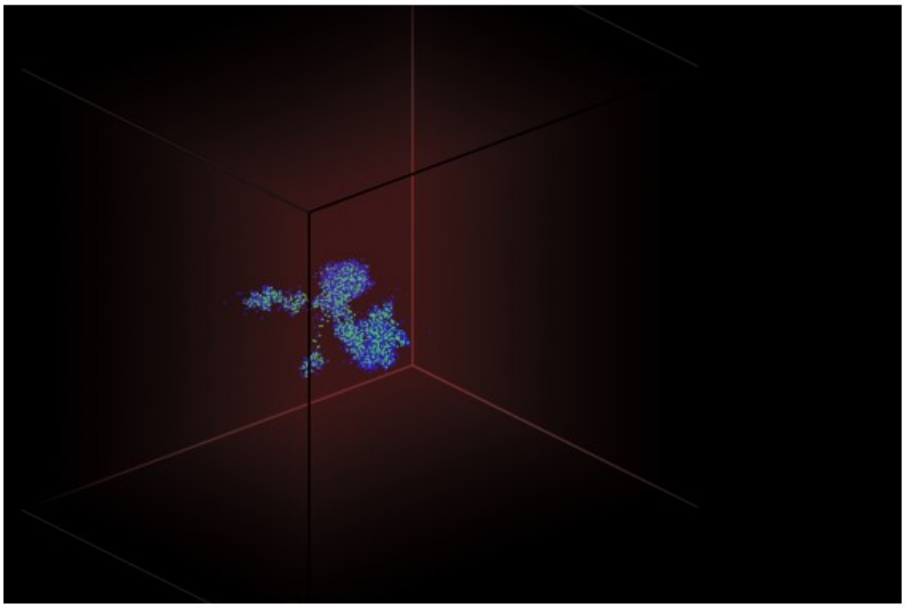

Simulation Box size [Å3]			Pka Energy	Number of Frenkel Pair	@
x	y	z	[keV]		
679.14	679.94	680.38	22	428	1.2 ps

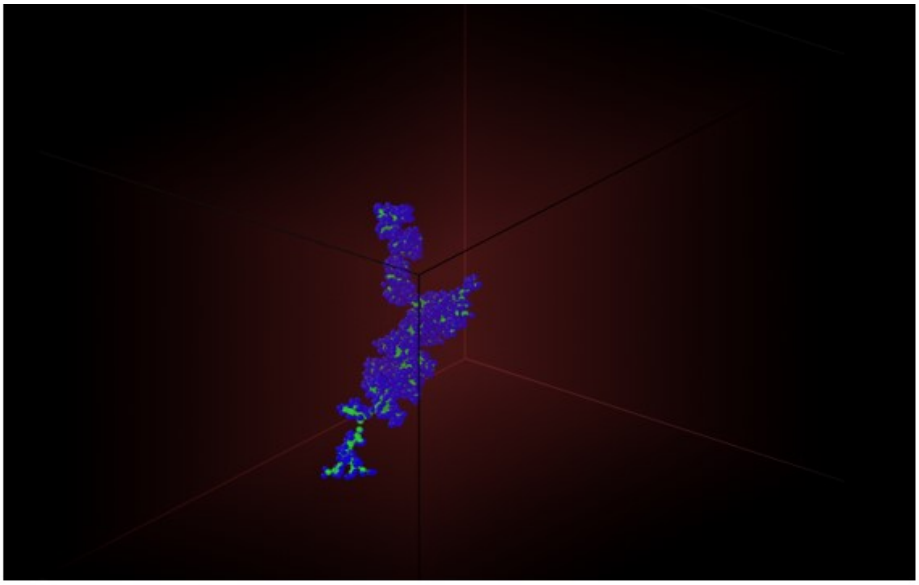

Simulation Box size [Å3]			Pka Energy	Number of Frenkel Pair	@
x	y	z	[keV]		
906.59	907.18	906.59	65	1204	2.1 ps

Figure 8.4: Cascade configuration after thermal spike for the cascades at different PKA energies(vacancies and interstitials are presented with green and blue respectively)

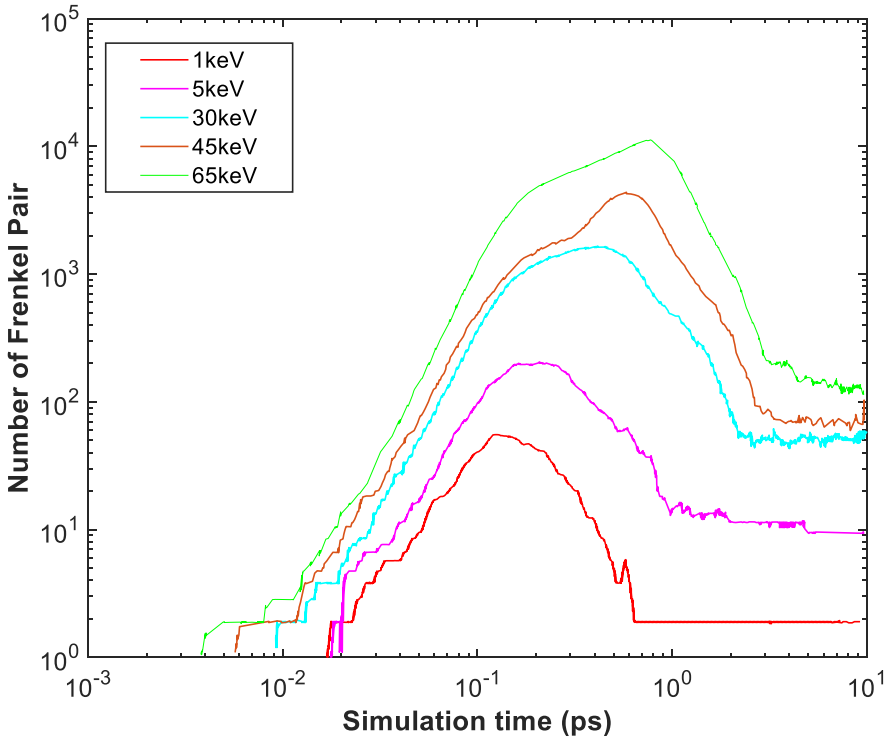

Figure 8.5: Time evolution of defects formed during displacement cascades

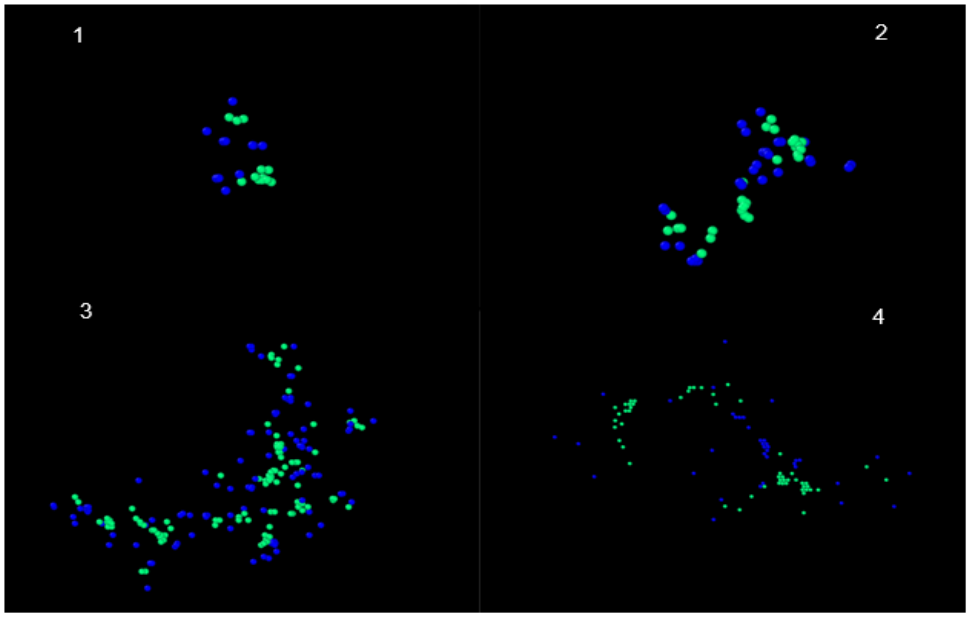

Figure 8.6: Stable defect configurations at 573°K in (1) with 12fp for 5 keV PKA, (2) with 38 fp for 22 keV PKA, (3) with 78 fp for 45 keV PKA and (4) with 112 fp for 65 keV

Depending on the PKA energy, the peak occurs at a time in the range of 0.1 to 1 ps. This evolution is illustrated in Figure 8.5 for a range of PKA energies, where the number of vacancies is shown as a function of time. Many vacancy-interstitial pairs are in quite proximity at the time of peak disorder. An essentially thermal process of in-cascade recombination of these close pairs takes place as they lose their kinetic energy. This leads to a reduction in the number of defects until a quasi-steady-state value is reached after about 5 to 10 ps. Finally, a stage is reached where the remaining point defects are sufficiently well separated that further recombination is unlikely on the time scale (a few hundred ps) accessible by MD. The spatial distributions of these surviving defects, which are also called stable defects, are given in Figure 8.6 for different energies.

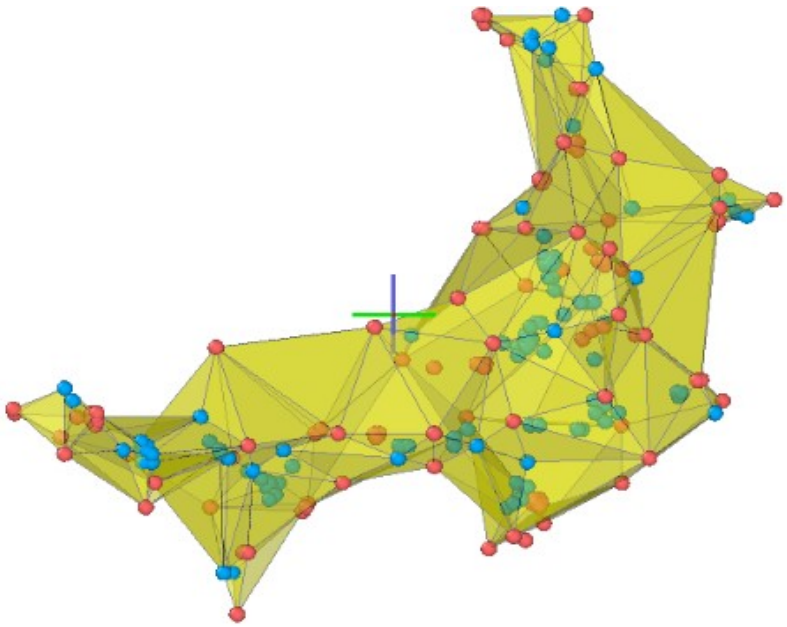

Figure 8.7: Vacancies (in blue) and interstitials (in red) obtained after the cascade relaxation of a 65.7 keV Zr PKA (at 50 ps) using the Wigner-Seitz module: the yellow surfaces represents the cascade overlay using the MD “Construct Surface Mesh” module, the black lines represent the convex-hull of the cascade.

In order to provide more detail on characteristics of cascade configuration, another procedure can be involved. To determine the cascade sizes, displaced atoms were displayed using Wigner- Seitz module of OVITO. To fit the cascade shape, the “Construct surface mesh” [187] module of OVITO was then used. After determining the convex hull of the displaced atoms which can be seen at Fig 8.7. This module removes parts of the convex hull using a probe radius. The probe

radius r_p equals to the nearest neighbor atom separation (r_p =3.2 Å). Regarding the probe radius, the surface areas and volumes of cascades were calculated and presented at Table 8.2.

Table 8.2: Average number of frenkel pairs at different temperatures, maximum values of cascade surface area and volume per PKA energy

E_{PKA} (keV)	N_{fp} (300K)	N_{fp} (630K)	Surface area max (nm^2)	Volume max (nm^3)
1.07	4.04	3.52	8.65	65.45
1.77	5.63	4.91	10.20	86.16
2.17	6.42	5.62	38.40	99.02
2.86	7.67	6.74	61.80	127.22
4.42	10.5	8.99	94.60	192.19
5.61	12	10.52	176.45	314.79
6.09	12.306	11.11	183.54	342.42
8.65	15.44	14.01	243.60	429.36
10.5	17.22	15.92	285.57	523.60
12.6	18.35	18.80	302.34	700.72
15.4	26.02	23.13	356.52	913.86
17.6	29.8	26.546	382.50	1007.99
22.7	38.4	34.50	336.00	1838.78

E_{PKA} (keV)	N_{fp} (300K)	N_{fp} (630K)	Surface area max (nm^2)	Volume max (nm^3)
26.9	43.9	41.11	406.70	1875.31
29.7	51.1	45.52	607.30	2144.66
33.9	58.6	52.18	684.56	2049.59
37.2	62.7	57.42	804.70	1957.37
42	72	65.08	946.05	3053.63
45.6	77.9	70.83	1106.50	3501.39
48.5	80.8	75.48	1430.46	5575.28
52.8	87.8	82.39	1745.30	7256.34
54.7	92.4	85.45	1832.57	7420.69
58.3	98.8	91.26	1892.30	8499.43
60	101.16	94.00	2017.43	9202.77
65.7	109.42	103.22	2306.12	11008.44

8.1.2.2 Stable defect formation statistics

It has been known that number of stable Frenkel pair has a simple power function with cascade energy,

$$N_{FP} = A(E_{MD})^B$$

where E_{MD} is referred to as PKA energy. To obtain statistically significant results, 60 parallel cascade events were evaluated per PKA energy. This is illustrated in

Figure 8.8 where the values of number of Frenkel pair obtained in cascade simulations at 300 °K, 573 °K and 673 °K are plotted as a function of PKA energy. At each energy, the data point is an average of 60 cascades, and the error bars indicate the standard error of the mean.

Table 8.3: The coefficients of the empirical power law formula in hcp-Zr at various temperatures

A (keV)	**B**	**E_{PKA} (keV)**	**T(K)**	**Potentials**	**Reference**
4.19	0.79	~20	100	Finis-Sinclair(F-S)	[188,189]
4.57	0.74	~20	100	Many-body InteratomicPotential	[190]
3.61	0.76	~20	600	Many-body InteratomicPotential	[190]
5.62	0.66	0.5-15	300	EAM-2	[191]
3.83	0.63	1-10	300	EAM-3	[192]
1.6	1	10-80	300	EAM-3	
3.91	0.65	1-10	300	EAM-3	**Calculated**
1.6	1.01	10-65	300	EAM-3	

By the least-square method, the number of stable Frenkel pairs calculated from 1 keV to 65 keV at 300 °K were fitted by the power function. The data points can be separated into two parts with different fitting parameters. Table 8.3 shows the fitting values of A and B for hcp-Zr at different temperatures using various potentials. The fitted values of A and B are 3.91 and 0.65 in the 1-10 keV range while they are 1.60 and 1.01 in the 10-65 keV range, respectively. According to Wooding et al. [188], A and B for metallic materials always range from 4.5 to 6 and from 0.7 to 0.8,

respectively. Gao et al. [190] gave A to range between 4 and 8 and B between 0.7 and 0.8, respectively. In this work, for that energy range(~20keV) A and B are slightly small from those ranges. The other evaluation can be made on chosen interatomic potentials. In present work, temperature and selected interatomic potential present a consistency with Ref [192] and as result, A and B values for both range (1-10 and 10-65 keV) are in good agreement.

The effect of irradiation temperature is shown in Figure 8.9, which compares the defect survival fractions obtained from simulations at 300, 573, and 630°K. A given amount of kinetic energy tends to produce a given number of stable point defects; this simple observation is embedded in the NRT model, i.e., the number of predicted defects is linear in the ratio of the energy available to the energy per defect. the defect survival fraction at 300 °K is always somewhat greater than at either of the two higher temperatures. The fact that defect survival at 573 °K and 630 °K is lower than at 300 °K suggests that the 300 K results may be somewhat biased toward lower survival values by the PKA-induced heating.

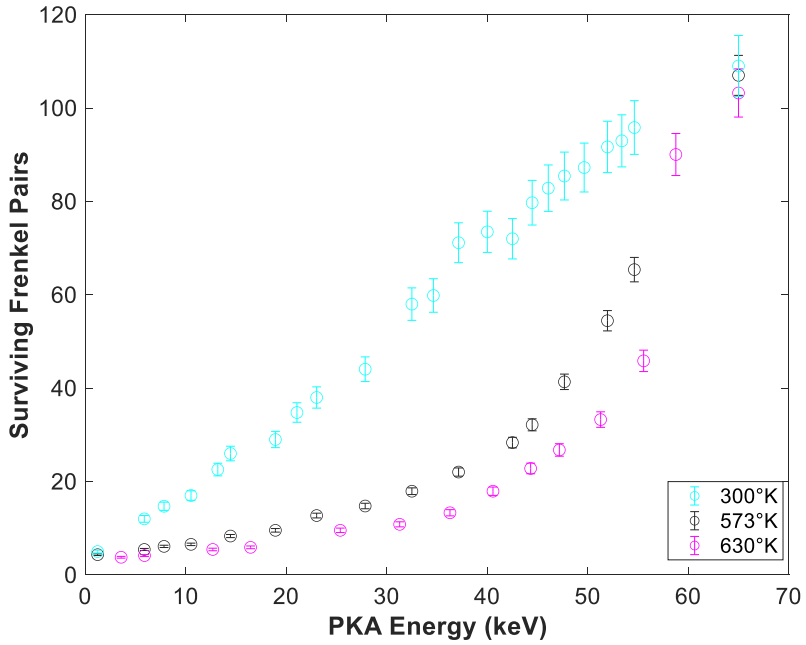

Figure 8.8: Stable point defect formation as a function of PKA energy in cascade simulations

The dependence of in-cascade interstitial clustering on cascade energy is shown in Figure 8.10 for a simulation temperature of 300°K, 573°K and 630°K, where the

average number of interstitials in clusters of size two or larger at each energy has been divided by the total number of surviving interstitials. The data points and error bars in Figure 7.9 indicate the mean and standard error at each PKA energy.

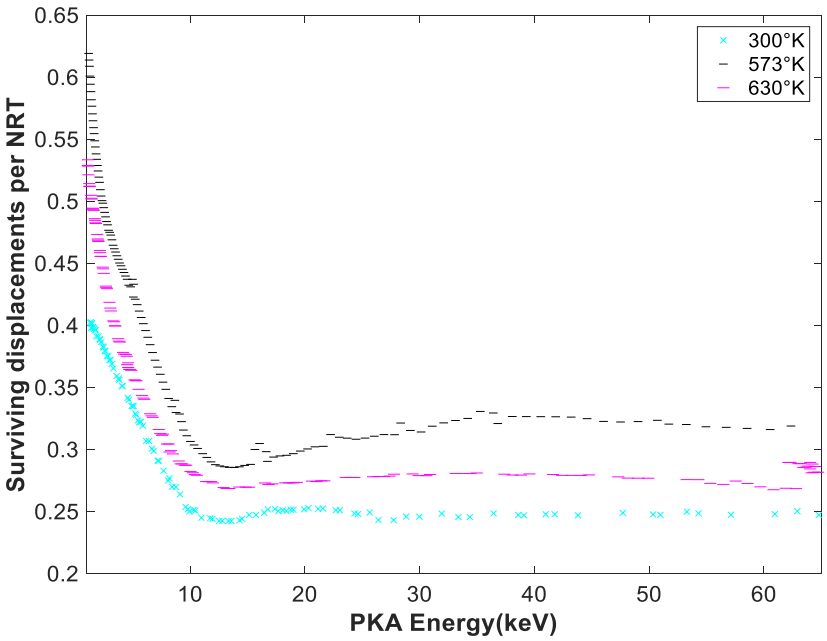

Figure 8.9: Temperature dependence of stable defect formation in cascade simulations: Ratio of simulated point defects to NRT displacements

The error bars can be used to make two significant comments. First, the relative scatter is much higher at lower energies, which is similar to the case of defect survival shown in Figure 8.10. Second, comparing again with Figure 8.10, the standard errors about the mean for interstitial clustering are greater at each energy than they are for defect survival. The fact that the interstitial clustering fraction exhibits greater variability between cascades at a given energy than does defect survival is essentially related to the variety of defect configurations that are possible. At the lowest energies, where relatively few defects are created, some cascades produce no interstitial clusters, and this is primarily responsible for the larger error bars at these energies. There is a trend toward greater clustering with increasing temperature at higher energies.

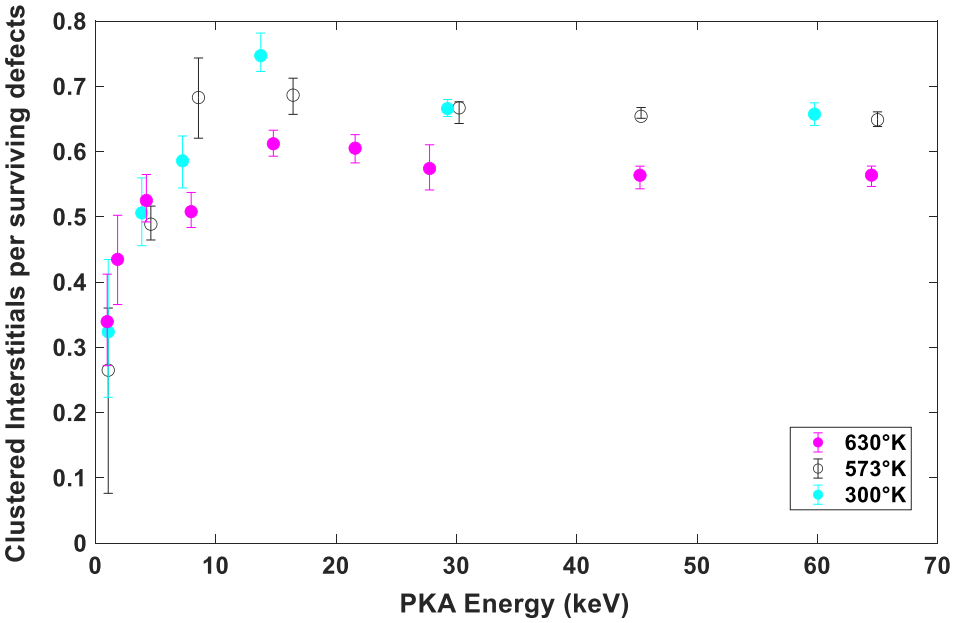

Figure 8.10: Fraction of surviving interstitials relative to the total number of point defects created at different temperatures

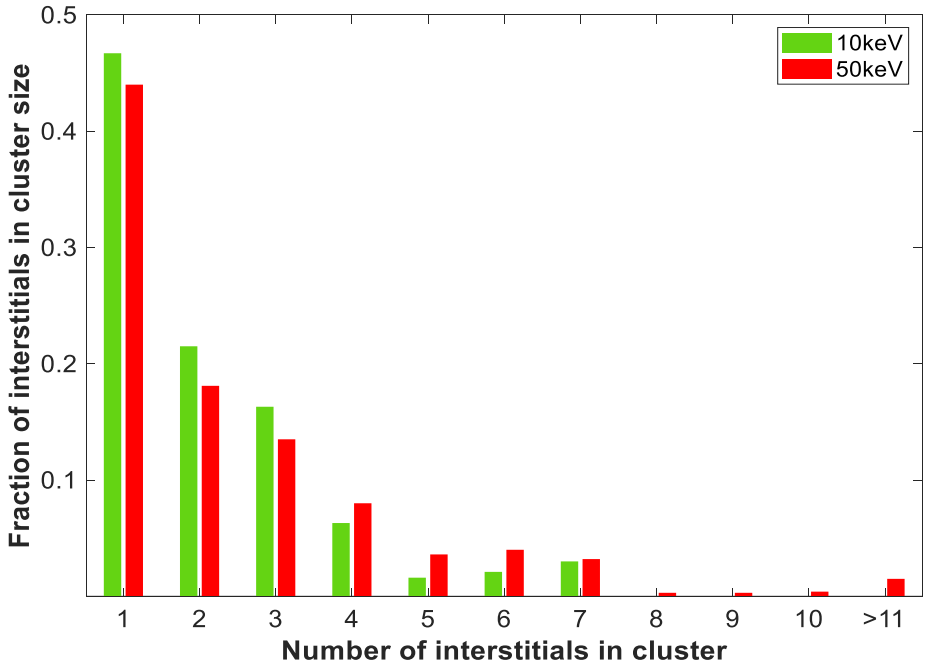

Figure 8.11: Fractional size distributions of interstitial clusters formed directly within the cascade, comparison of 10 and 50 keV cascades at 630°K

The interstitial cluster size distributions exhibit a consistent dependence on cascade energy as shown in Figure 8.11 (where a size of 1 denotes the single interstitial), where the size distributions from 10 and 50 keV are included. All interstitial clusters larger than size 10 are combined into a single class in the histograms. The interstitial cluster size distribution shifts to larger sizes as the PKA energy increases. Fractional vacancy cluster size distributions are shown in Figure 8.12, for which the 4-nn clustering criterion was used. Figure 8.12 illustrates that the vacancy cluster size distribution shifts to larger sizes as the cascade energy increases from 10 to 50 keV. This is similar to the change shown for interstitial clusters in Figure 8.11. There is a corresponding reduction in the fraction of single vacancies.

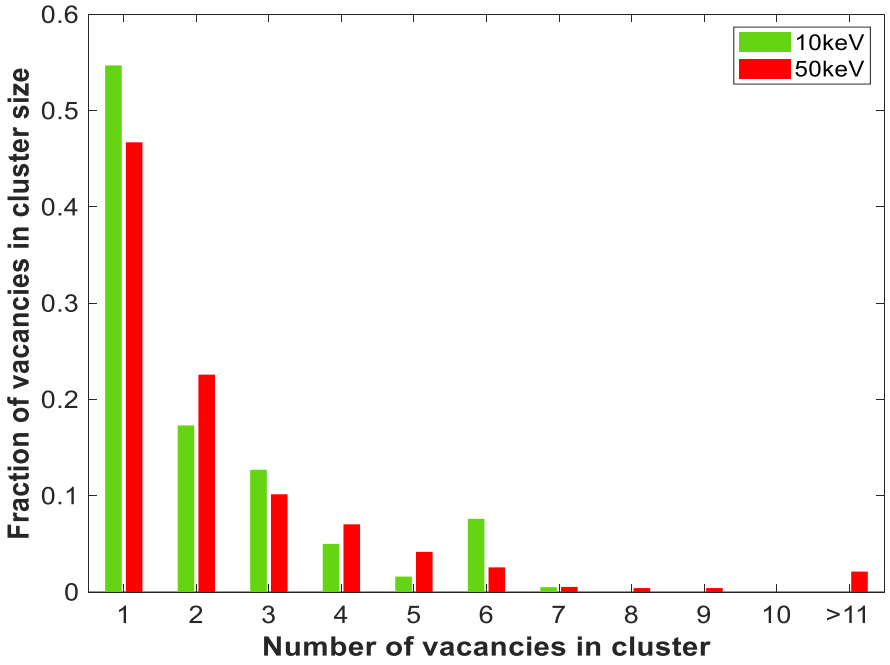

Figure 8.12: Fractional size distributions of vacancy clusters formed directly within the cascade, comparison of 10 and 50 keV cascades at 630°K

8.1.3 Defect Cluster (KMC)

8.1.3.1 Result of test simulation

A test simulation was performed to test the success of defect type parametrization**.** Simulated time is 10^6 s at the temperature 630 °K. The simulation box (a non-cubic

block of Zirconium atoms with dimensions 97.2 x 98.5 x 99.1 nm^3 (lattice parameter a=3.24 Å)). 1000 cascade events at PKA energies between 1-65 keV created using MD simulations, was used to carry out this simulation. Damage accumulation was simulated using the material and irradiation conditions in Table 8.4.

Table 8.4: Simulation parameters of the test simulation

Simulation Parameters		
Temperature	630	°K
Dose rate	$7x10^{-6}$	dpa/s
Grain Size	16	µm
	Vacancy	**Interstitial**
$\bar{\mathbf{D}}$ $[Å\mathbf{s^{-1}}]$	$1.2 x10^{10}$	$7.11 x10^{10}$

Figure 8.13 shows the spatial distribution of defect clusters at a dose of 7dpa. <a> type vacancy clusters are presented with blue loops. <a> type vacancy clusters are shown in the form of spherical red objects. <c> type vacancy clusters can be seen with cyan loops which locate along vertical axis of the <a> type vacancy clusters. At the reached dose, all modelled defect types can be observed. For the simplicity in visualization, all clusters with the size (<20-point defects) were removed from distribution.

8.1.3.2 Defect cluster evolution

Simulated time for operation condition of the fuel element is 2 years. Operating temperature 630 °K. The effect of finite grain size was introduced by adopting finite periodic boundary (FBC)conditions in all three directions. The simulation box (a non-cubic block of Zirconium atoms with dimensions 97.2 x 98.5 x 99.1 nm^3 (lattice parameter a=3.24 Å)) is assumed to be at the center of a spherical grain. Damage accumulation is simulated using the material and irradiation conditions in Table 8.5. The dose rate has already been calculated using SPECTER code

regarding operating conditions. For the dose rate 3.2 x10^{-8} dpa/s, the cascade insertion rate was calculated as 0.0274 cascade per second. 2000 cascade events at PKA energies between 1-65 keV created using MD simulations, was used to carry out this simulation. The volume was set as 9.48x10^{-22} m^3.

Table 8.5: Simulation parameters used in this study

Simulation Parameters			
Temperature		630	°K
Flux		6.26 x10^{17}	n/m^2s, E≥1MeV
Fluence		3.89 x10^{25}	n/m^2
Dose rate		3.19 x10^{8}	dpa/s
Grain Size		16	μm
		Vacancy	**Interstitial**
1.14%Sn	$D_{\parallel}$ [$Å s^{-1}$]	5.87 x10^{9}	5.54 x10^{10}
	$D_{\perp}$[$Å s^{-1}$]	5.06 x10^{10}	1.17 x10^{11}
Pure	$\bar{D}$ [$Å s^{-1}$]	1.2 x10^{10}	7.11 x10^{10}

Time evolution of clusters containing different number of interstitials and vacancies were recorded during simulation. A model which has relatively pore definition in terms of kinetic parameters (diffusion coefficients have no directional dependency), has been performed for pure zirconium. In this section this model was presented as pure-Zr model for comparison with 1.14 % Sn model which is fully parametrized.

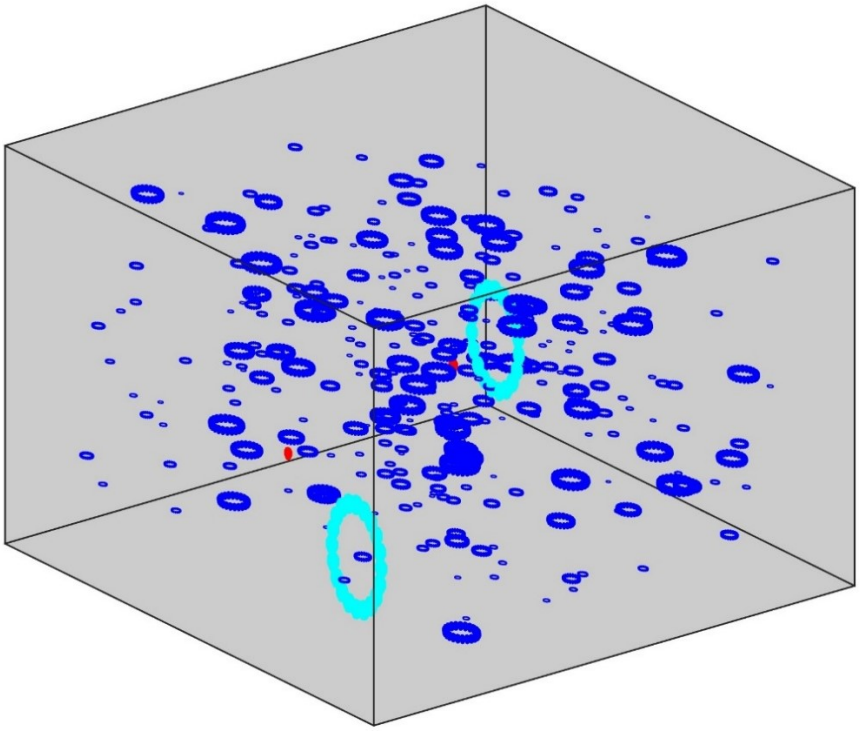

Figure 8.13: The spatial distribution of defect clusters at a dose of 7 dpa. <a> type interstitial clusters are red spheres, <c> type vacancy clusters are cyan loops and <a> type vacancy clusters are blue loops.

The number density of vacancy clusters of Zirconium and Zirconium (1.14% atomic Sn) models are presented in Figure 8.14.a and the number density of interstitial clusters is shown in Fig 8.14.b. During the initial stages of irradiation, a large fraction of the SIAs is absorbed at grain boundaries leading to a significant increase in the density of vacancy clusters. After increasing imparted cascades, an increasing fraction of the SIAs recombine with vacancies resulting in a gradual decrease of the damage (vacancy) accumulation rate. The effect of alloying element concentration can also be seen clearly in Fig 8.14. Immobile interstitial clusters in the initial model increase recombination and cause a decrease in the resulting number density of vacancy clusters. On the other hand, a significant increase in the number density of interstitial clusters is observed. From here, it would not be an inappropriate comment to say that the trap effect is seen for interstitial clusters at the same time as the alloy concentration added to the model.

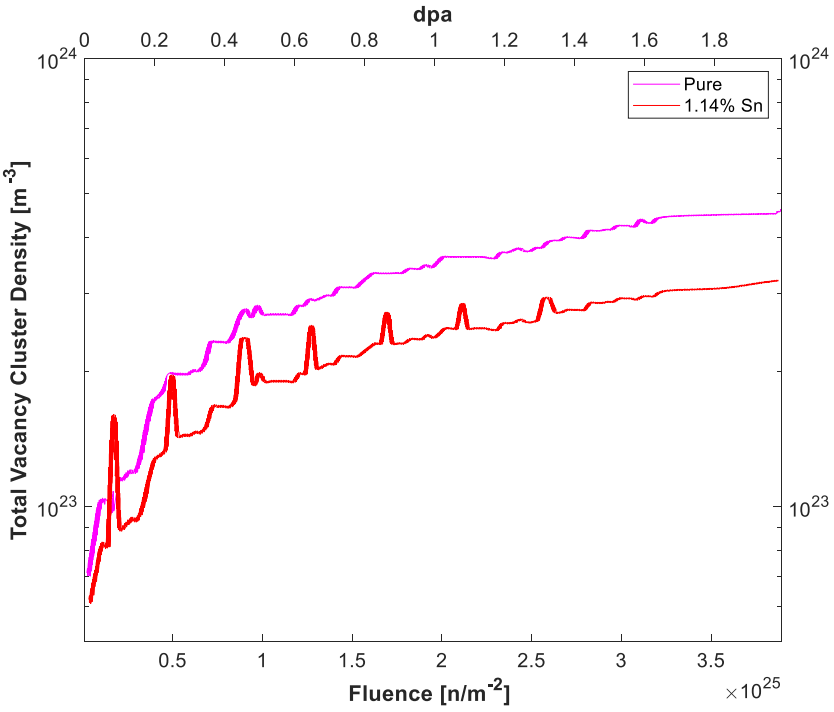

(a)

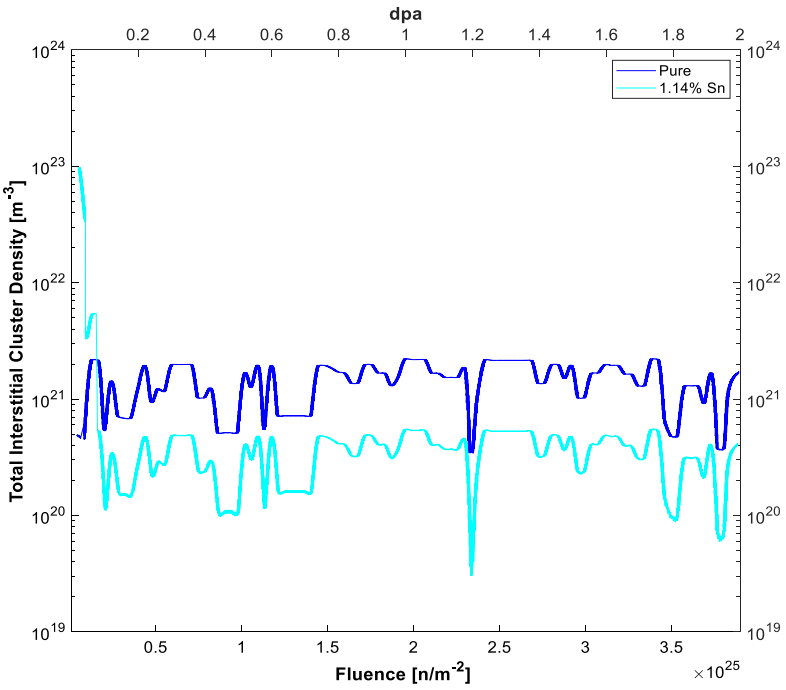

(b)

Figure 8.14: Total number density of defect clusters versus dpa (fluence)

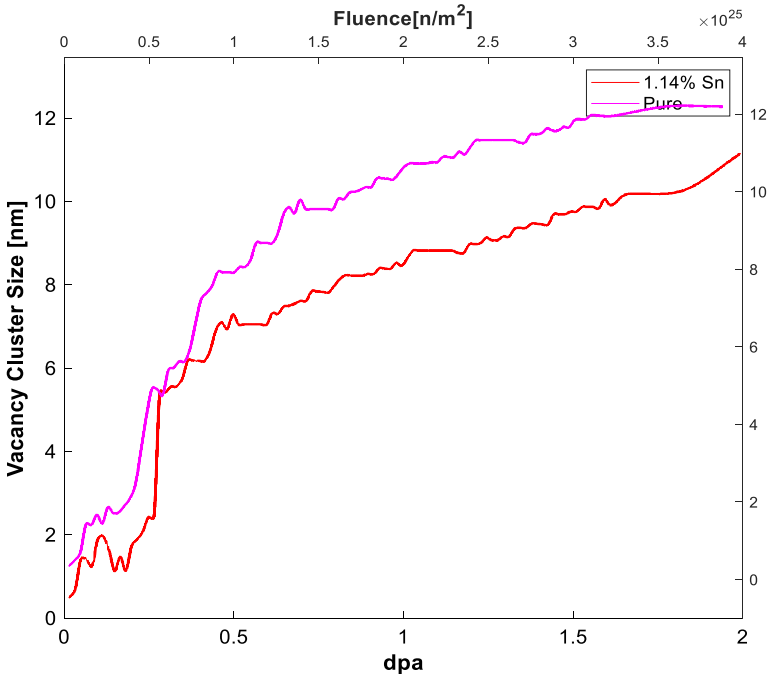

(a)

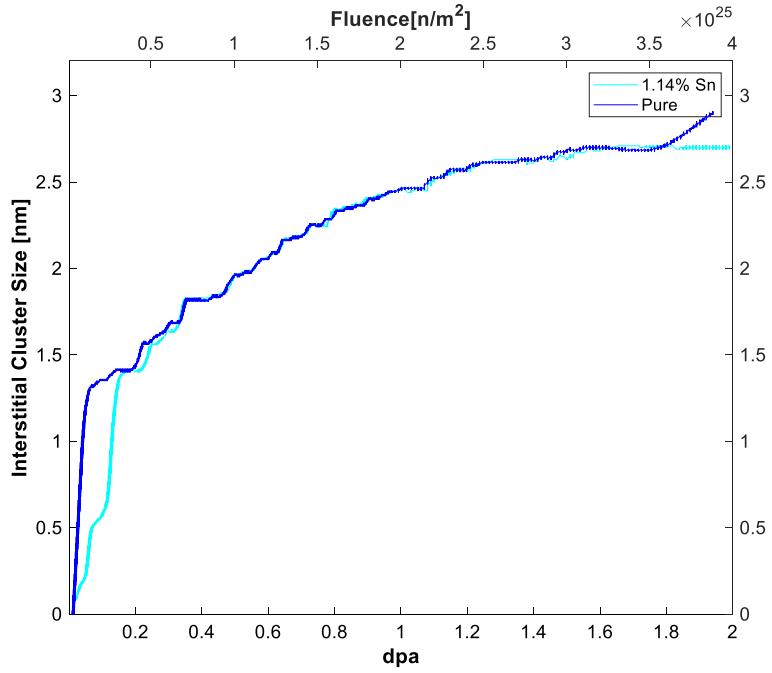

(b)

Figure 8.15: Average cluster sizes versus dpa (fluence)

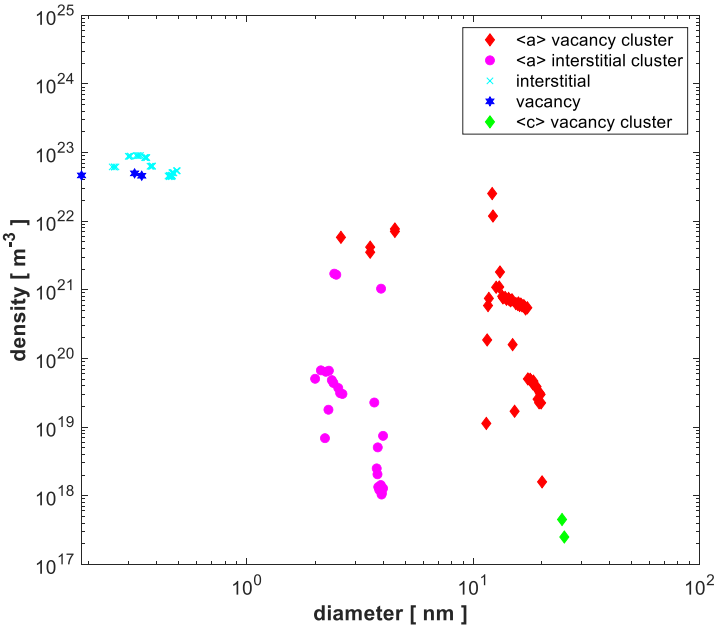

(a)

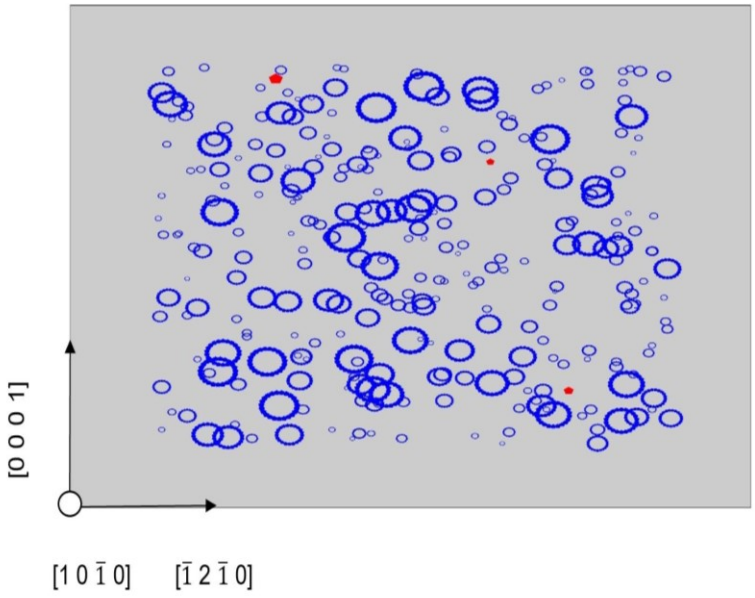

(b)

Figure 8.16: a: Size and density distribution of microstructures, b: configurations (where blue loops are <a> type vacancy clusters and red spheres are <a> type interstitial clusters for the pure Zr model regarding defect type at 1.99 dpa

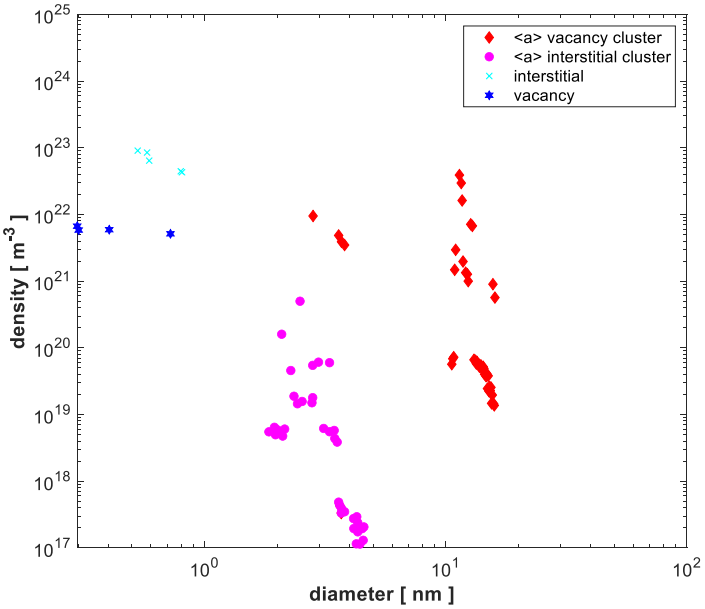

(a)

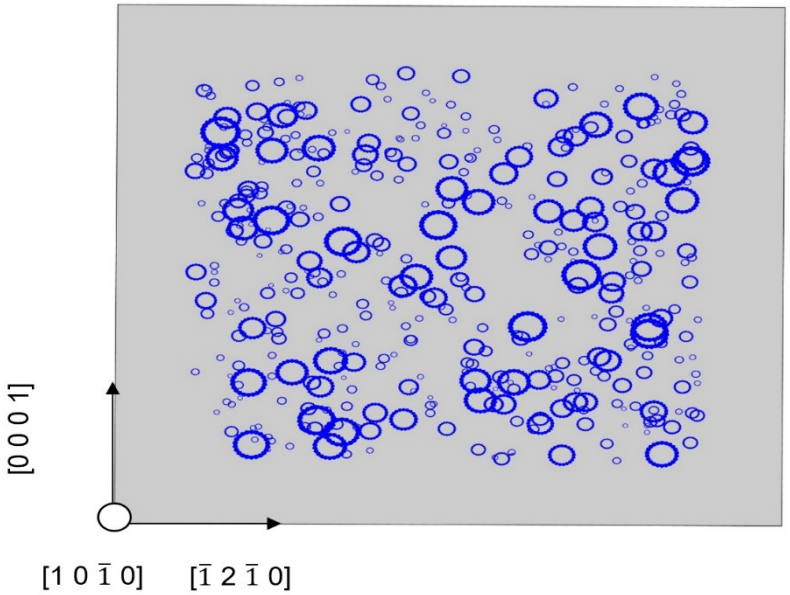

(b)

Figure 8.17: a: Size and density distribution of microstructures, b: configurations (where blue loops are <a> type vacancy clusters and red spheres are <a> type interstitial clusters for the 1.14%Sn-Zr model regarding defect type at 1.99 dpa

Diameter of clusters were calculated from the equation: $R = a\,(\frac{n}{\sqrt{2\pi}})^{1/2}$, where n and a are the number of vacancies or interstitials in the cluster and lattice constant (a_{Zr} = 0.324 nm) respectively. Figures 8.15 shows the average vacancy and SIA cluster diameter as a function of dose. In vacancy Increasing concentrations of vacancy clusters resulted with larger cluster sizes. while average SIA clusters size was ~2nm. This finding is physically meaningful because SIA clusters diffuse extremely fast and reach the grain boundaries very quickly. Production of larger defect clusters results in a lower fraction of diffusing defect species, which in turn results in a lower surviving damage as seen in Fig 8.15.a.

Regarding the individual defect types, cluster density distributions at reached fluence were evaluated for both models which can be seen in Figure 8.16 and 8.17. <a> type vacancy clusters are the dominant defects in the simulation for the pure Zr model. <c> type vacancy clusters are present in very low density (3×10^{17}) with an average diameter of about 25 nm. The low density of the <c> type can be compared to the relatively high emission capacity of the vacancy type <a> loops due to their low binding energy. The emitted vacancies are then redistributed in the system. Interstitial clusters can be seen in relatively low density and with the low sizes in Fig 8.16.a. Figure 8.16.b and 8.17.b show the configuration of vacancy and interstitial clusters at the fluence of 3.86 x 10^{25} (1.99 dpa) n/m^2. The typical characteristics of the microstructure are similar; number of accumulated clusters along (0001) plane is lower than the ($(11\bar{2}0)$) due to the directional diffusion anisotropy. The cluster size increases with increasing dose, and that the spatial ordering of bigger clusters (>2nm) along ($(11\bar{2}0)$) planes becomes clearer. A closer look at the projections reveals that relatively bigger clusters have the tendency of ordering along ($(11\bar{2}0)$) plane.

As presented in Figure 8.17.a, <c> type vacancy clusters do not occur in the simulation for 1.14% Sn. <c> loop formation has been defined as directionally and size dependent in the system. At the level of reached fluence (3.86 x 10^{25} n/m^2), <c> loop formation (> 10nm clusters in (0001) plane) was not observed (with the density of 10^{14} m^{-3}). Interstitial clusters are also in relatively low density (below 10^{21} m^{-3}). Considering the simulated volume size (~10^{21} m^{-3}), it doesn`t appear in the volume. This can be clearly seen in Fig 8.17.b.

8.2 Results of Rate Theory Modelling

8.2.1 Wet Storage (Phase 0)

The evolution of interstitial and vacancy concentrations during wet storage is given in Figure 8.18. When the bulk diffusion mechanism is operative, loop growth or shrinkage occurs by diffusion of point defects to and from the loops via the matrix. Due to the high mobility of self-interstitial atoms (SIA) they disappear rapidly. Because of the high formation energy of SIA, the contribution of SIA diffusion is believed to remain negligible. In addition, due to their high formation energy the SIA cannot be emitted from loops. Consequently, changes on loop densities are only controlled by the vacancy diffusion. The fluctuations seen on SIA distribution are because of the emission of SIA by vacancy loops due to the high formation energy of the interstitial. The problem here is that the rate equations are discrete equations. This problem may be removed using continuous equations like Fokker–Planck type equations. As can be seen in Fig 8.18, no change has been observed on <a> loop density and size during Phase 0.

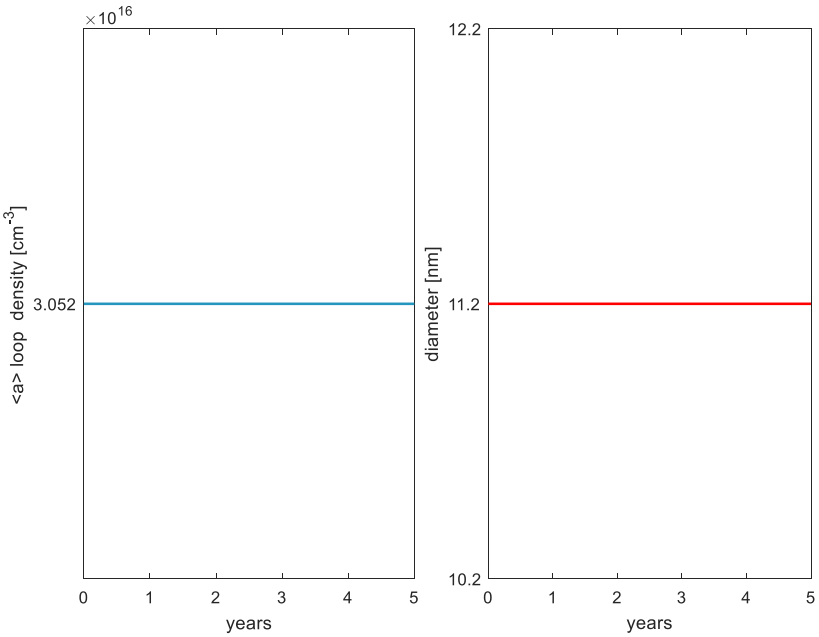

Figure 8.18: Defect concentration and sizes on phase 0

8.2.2 Drying Process (Phase 1)

Figure 8.19 shows the evolution of vacancy concentration during Phase 1. A decrease can be seen in the density of vacancy clusters after 10 h in the drying process. The reason for this change is that the diffusion rate at 350°C is ~106 times higher than the rate at 50°C. Therefore, vacancies have higher mobility; they absorbed from loops easier. This causes an increase in loop sizes. More precisely in Fig 8.19, it is observed that the loop density decreases while the loop size increases.

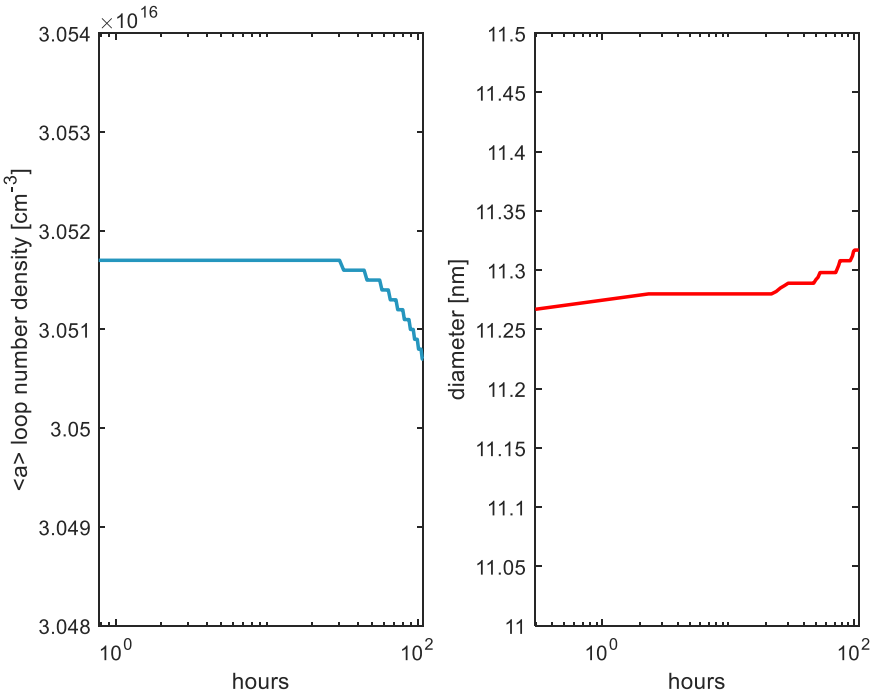

Figure 8.19: Defect concentration and sizes on phase 1

8.2.3 The First 10 Years at Dry Storage (Phase 2)

The design temperature of this phase was 300°C. The diffusion rate of vacancies has the highest value in all phases. Therefore, a significantly higher annealing in defect concentration is expected and can be seen in Figure 8.20. Tendency to grow on loops shows itself clearly in Phase 2. However, regarding the time (110h) and the trend of decrease of Phase 1, more annealing on loop densities would have been

expected. From that point, it wouldn't be wrong to say that grain boundary effect on defect annealing is more predominant in the longer term.

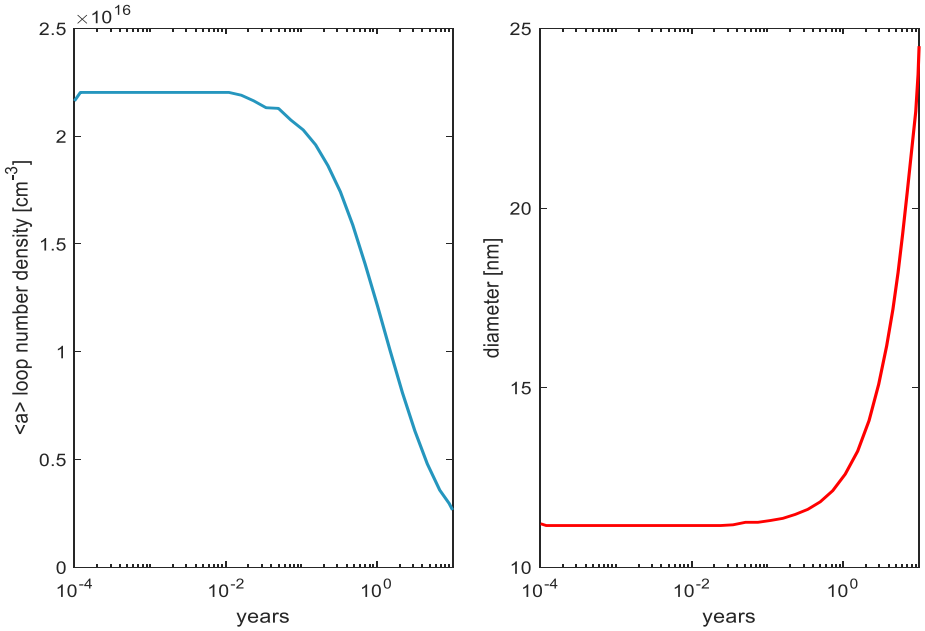

Figure 8.20: Defect concentration and sizes on phase 2

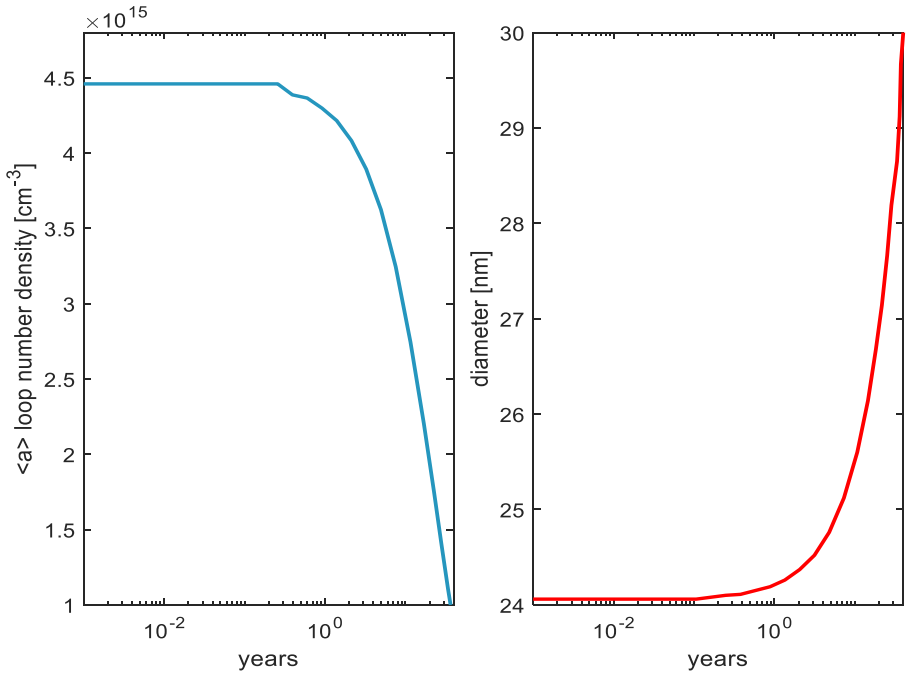

Figure 8.21: Defect concentration and sizes on phase 3

8.2.4 40 Years at Storage (Phase 3)

Figure 8.21 shows the evolution of defect concentrations and sizes at 200 °C for 30 years. After Phase 3, the concentration of loops decreases from 4.46 x 10^{15} to 7.8 x 10^{14} cm^{-3}. Respectively, the average size of loops raises to 30 nm.

8.2.5 60 Years at Dry Storage (Phase 4)

The design temperature of this phase was 150°C. The diffusion rate of vacancies is relatively low and but yet a significant decrease in vacancy densities, which can be seen in Fig 8.22, is observed. In parallel, the decrease on the loop concentration is very low. The reason for that is because the modeled time in Phase 2 is 60 years. Like it can be seen in Phase 2, absorption by grain boundaries effect is effective mechanism.

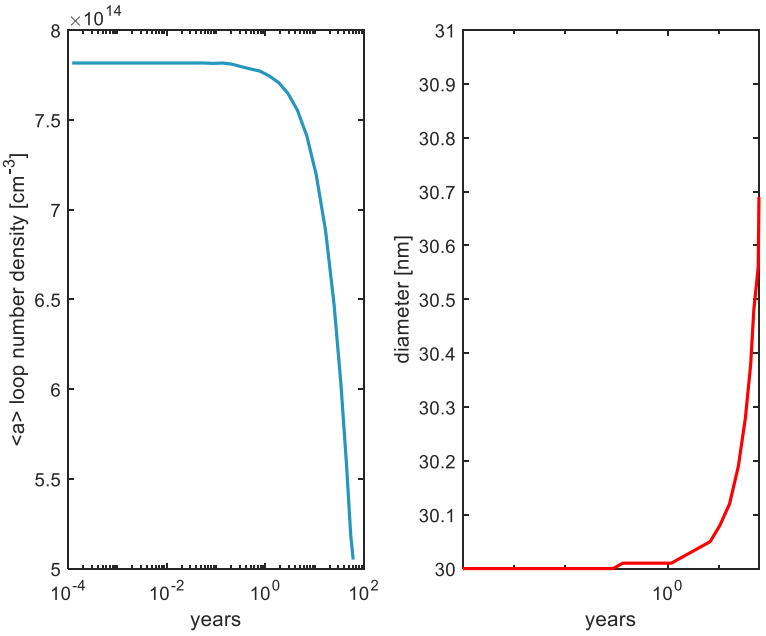

Figure 8.22: Defect concentration and sizes on phase 4

9 Macroscopic Effects of Radiation Induced Microstructures

9.1 Method

During the irradiation the creation and the evolution of the point defect (PD) induced changes in the microstructure at various scales: PD concentrations are increased (mainly vacancies, but also interstitials while at lower concentrations), clustering of PD leads to formation of dislocations loops that may interact during their growth, leading to a dense dislocation network and PD diffusing to the sinks. These changes in microstructure induce significant evolution of the properties of the material under irradiation.

The major effects in mechanical properties to be considered are restricted to the effects induced by the changes in microstructure resulting from PD clustering. The basic mechanisms of radiation hardening are related to the formation of several types of PD clusters that act as pinning centers for the dislocations. The consequence is an increase in yield strength with irradiation dose.

Another effect caused by irradiation-induced microstructural changes is dimensional instability. During irradiation, zirconium alloys behave differently from most other engineering alloys in that they resist swelling. Although they do not swell, they do exhibit anisotropic dimensional changes in the absence of an applied stress or volume change under irradiation that depend on their microstructures; this process is called irradiation growth.

These macroscopic effects can be established through the distribution of defect clusters (density and size distribution) related to the phenomena under consideration. Knowing the distribution of the PD clusters obtained after irradiation the contribution of all these clusters to the reduction of mobility of the dislocations can be computed.

In the following two sections, simplified analytical and numerical approaches for the estimation of the hardening and growth phenomena are evaluated.

9.1.1 Analytic Model of Hardening

Following the classical dislocation theory, any crystallographic defect along the glide plane of a dislocation induces a force to the dislocation, reducing its mobility. The increase in shear strength is given by the following relationship:

$$\boldsymbol{\Delta\tau = \frac{\alpha\mu b}{L}} \qquad 9.1$$

where μ is the shear modulus of the crystal, b is the Burgers vector of the dislocation, and L is the average distance between obstacles along the gliding plane. α is defined as the strength of the obstacle, always lower than 1, but with actual value depending on the obstacle types.

The internal structure of the clusters is considered by the so-called obstacle strength. The average obstacle distance, on the other hand, results from the cluster concentration. The resistance that a planar arrangement of obstacles presents to the sliding of a single of a single step dislocation was first considered by Orowan [193] as can be seen in Fig. 9.1.

In the case of small loops and small clusters, the increase in yield strength is thus given by the following relation:

$$\boldsymbol{\Delta\sigma_Y = M\alpha\mu b(d\rho_L)^{1/2}} \qquad 9.2$$

and in the case of a dislocation forest:

$$\boldsymbol{\Delta\sigma_Y = M\alpha\mu b(\rho_\perp)^{1/2}} \qquad 9.3$$

In these expressions M is the so-called Taylor factor that links the shear strength on a given glide plane of a single crystal τ, to the yield strength of polycrystals ($M \approx 3$ for alloys of interest [194].

The strengths of each type of PD clusters differ according mostly to their sizes. For large voids or precipitates, the strength α is close to 1 and there are considered as strong obstacles. Medium strength obstacles correspond to Frank loops in fcc alloys

or fine loops in bcc and dispersion phases ($\alpha \approx 0.3 - 0.4$), while dislocations and very small loops and clusters are considered as weak barriers for the dislocations ($\alpha \approx 0.12 - 0.22$). An increase in yield strength can be explained, and the results follow, at least qualitatively, the actual behavior of the cladding material after irradiation.

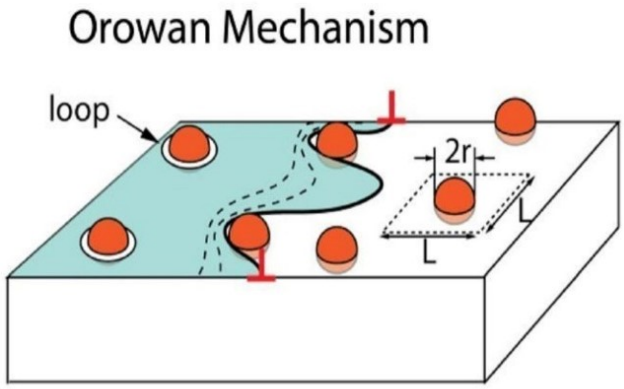

Figure 9.1: Orowan mechanism

9.1.2 Analytic Model of Growth

Irradiation growth occurs only in anisotropic materials because the defect diffusion coefficient is different between the basal plane and the prism plane [186], Self-interstitial atom (SIA) shows much more this tendency, i.e., high diffusion coefficient in basal plane and low diffusion coefficient in prism plain [183,186,195]. Even though the stresses in the thermal spike may all be compressive (depending on the temperature in the thermal spike), the driving force in terms of work done when the loops form from a super-saturated solid solution would favor <c> loops on basal plane (0001) and <a> loops on prism planes {1010}, see Figure 9.2.

Golubov et al. [182] developed a growth prediction model which was based on the recently updated Radiation Damage Theory. According to this model, the irradiation growth strain rate was calculated using the dislocation climb mechanism.

$$\frac{d\varepsilon}{dt} = \rho b \mathcal{V} \quad (9.4)$$

where ε is the elongation (cm), ρ is the dislocation density (cm^{-2}), b is the Burgers vector (cm), $\mathcal{V}$ is the dislocation velocity ($cm^{-2}\ s^{-1}$),

D_i and D_v are the interstitial and vacancy diffusion coefficients, respectively.

$$\mathcal{V} = \frac{1}{b}(D_i C_i - D_v C_v) \quad (9.5)$$

These phenomena occur in one direction. However, irradiation growth occurs in various directions. Therefore, this general equation is limited to the calculation of each sink strain.

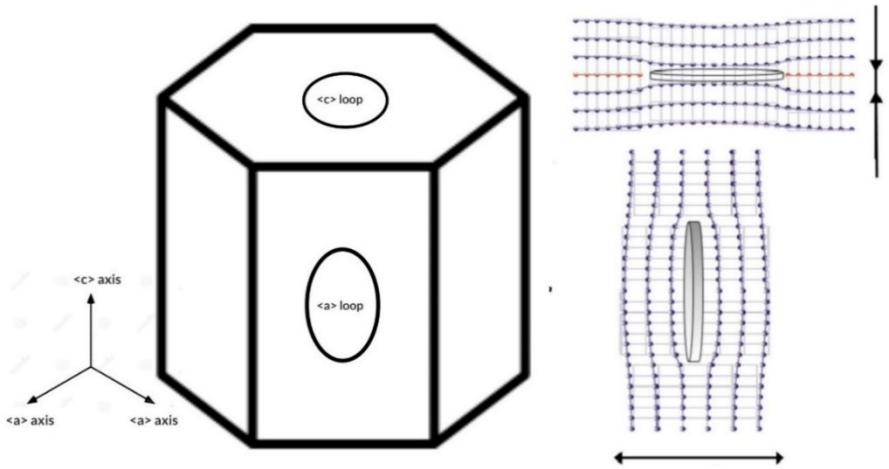

Figure 9.2: Left: Schematic showing irradiation growth in Zr. Right: <c> loops form on basal (0001) planes and <a> loops form on {1010} planes

In single crystal, it is assumed that dislocation loops are only sinks that contribute to growth. the growth strain induced by dislocation loops in the prism plane:

$$\frac{d\varepsilon^a}{dt} = A_{al}\rho_{al}(D_i C_i - D_v C_v) \quad (9.6)$$

A_{al} average strain factor for <a> loop

ρ_{al} sink strength for <a> loop

Ci: interstitial cluster density in the prism plane

Cv: vacancy cluster density in the prism plane.

The growth strain induced by dislocation loops in the basal plane:

$$\frac{d\varepsilon^c}{dt} = \boldsymbol{A_{vl}\rho_{vl}(D_vC_v - D_iC_i)} \quad 9.7$$

A_{vl} average strain factor for <c> loop

ρ_{vl} sink strength for <c> loop

Ci: interstitial cluster density in the basal plane

Cv: vacancy cluster density in the basal plane.

In polycrystalline, grain boundary sink and orientation (texture) must be considered in growth equation. The growth equation which contains of grain boundary effect is expressed by:

$$\frac{d\varepsilon_a^{gp}}{dt} = \boldsymbol{A_{gp}\rho_{gp}(D_iC_i - D_vC_v)} \quad 9.8$$

$$\frac{d\varepsilon_c^{gb}}{dt} = \boldsymbol{A_{gb}\rho_{gb}(D_iC_i - D_vC_v)} \quad 9.9$$

$$\frac{d\varepsilon^d}{dt} = \boldsymbol{G_{poly}x}\left(\frac{d\varepsilon^a}{dt} + \frac{d\varepsilon_a^{gp}}{dt}\right) \quad 9.10$$

A_{gp} is the average strain factors for grain boundaries in the prism of single grain

ρ_{vl} sink strength for <c> loop

Ci: interstitial cluster density captured in grain boundaries

Cv: vacancy cluster density captured in grain boundaries

where ε^d is irradiation growth strain in the direction of interest of polycrystal; and ε_a^{gp} is the irradiation growth strain induced by grain boundaries in the prism of single grain; A_{gp} is the average strain factors for grain boundaries in the prism of single grain. In tradition, anisotropy factor was simply calculated by F factor (G_{poly} = 1 − 3F). However, recent studies reported that irradiation growth of polycrystal could not be simply calculated by simple anisotropy factor because the difference of each grain orientation induced the grain interaction. Therefore, grain-interaction could make a change of irradiation growth depending upon specimen texture.

9.2 Results

The work to calculate macroscopic effect of radiation-induced clusters can be divided into two categories: The change in material properties in terms of yield strength is determined and dimensional instability is considered by calculation of irradiation growth strain.

9.2.1 Change in Yield Strength

Determination of yield strength change is performed by employing Orowan correlation. To consider the effect of individual defect types, a hardening calculation will be performed using different approaches. The first assumption accepts that all defect clusters (vacancy and interstitials) are obstacles that increase hardening. The second approach assumes that irradiation hardening is due to only <a> loops. The third and final assumption includes the <c> loop effect on hardening increase, as shown in Table 9.1. Parameters used for all assumptions are given in Table 9.2. a1 a2 and a3 are used to describe the strength of the individual barriers. For barriers that are too hard to be penetrated and can only be overcome by dislocation bow (Orowan hardening), a = 1 [52]. For softer barriers that can be cut by the dislocation, a < 1. Values of a for dislocation loops have been reported to range from 0.25 to 0.5 [52] with the value of a = 0.25 being more typical in some cases [73].

Table 9.1: Employed analytic correlations

1st assumption	$\Delta\sigma_y = \alpha M G b \sqrt{D_{avg} N D_{avg}}$
2nd assumption	$\Delta\sigma_y = \alpha M G b \sqrt{\sum_{i=bins} D_{<\alpha>} N D_{<a>}}$
3rd assumption	$\Delta\sigma_y = \sqrt{(\alpha_{<\alpha>} M G b_{<\alpha>} \sqrt{D_{<\alpha>} N D_{<\alpha>}})^2 + (\alpha_{<c>} M G b_{<c>} \sqrt{D_{<c>} N D_{<c>}})^2}$
4th assumption	$\Delta\sigma_y = \alpha_{<\alpha>} M G b_{<\alpha>} \sqrt{D_{<\alpha>} N D_{<\alpha>}} + \alpha_{<c>} M G b_{<c>} \sqrt{D_{<c>} N D_{<c>}}$

Table 9.2: Parameters for yield strength calculation

α_1	0.25
α_2	1
α_3	0.39
G	32.3 GPA
$b_{<a>}$	3.23 A
$b_{<c>}$	5.15 A
M	2

The yield strength change was calculated, shown in Figure 9.3, using four assumptions. For the pure zirconium model, by considering defect densities as soft barriers for dislocation motion (a1= 0.25) the yield strength increase ranges from 102 to 373 MPa for 4 different assumptions.

.

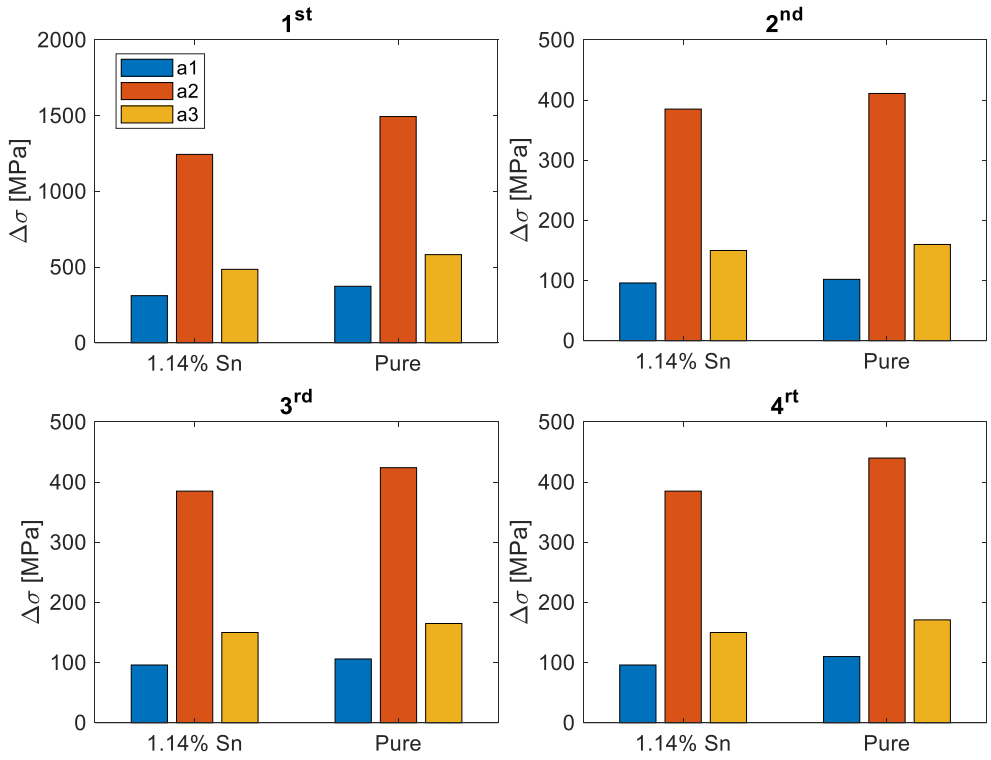

Figure 9.3: Change in yield strength with different assumptions

If <a> loops only cause the increase in hardening, the yield strength change is 102 MPa. Regarding the 3rd assumption, the <c> loop contribution to increase in hardening is 3.9%. The 4th assumption estimates this contribution as 7.8%. For a=1 (a2), the change in yield strength is between 411 and 1494 MPa. Since the 4th assumption includes a linear addition of the <a> and <c> loop strengthening, it may be considered as the maximum extent of calculated irradiation hardening contribution due to the combined effects of <a> and <c> loop hardening.

For 1.14% Sn model, yield strength increases between 96and 385MPa when it is assumed that <a> loops contribute to yield increase (3rd assumption). Since the density (1 x 10^{14}) c loops is very low in this model, the last three assumption calculate similar results. If the <a> dislocation loops are treated as rigid barriers by assigning a = 1(a_2) as is generally done with voids, change in yield strength for all assumptions is 3 times higher than a=0.25. But this is expected since loops may not be hardly impenetrable obstacles, yield strength change determined for <a> loop is between 96 and 385 MPa.

It has been possible to establish empirical correlations for some properties; the most used ones are:

$$\Delta\boldsymbol{\sigma_{YS}} = \mathbf{3}\Delta\mathbf{H} \qquad [185] \quad 9.11$$

$$\Delta\boldsymbol{\sigma_{YS}} \approx \Delta\boldsymbol{\sigma_{US}} \qquad [28] \quad 9.12$$

where $\Delta\sigma_{YS}$, ΔH, $\Delta\sigma_{US}$ are respectively increase of yield strength, hardness, and ultimate strength. Accordingly, the effect of defect density on yield strength variation was calculated in terms of hardness and ultimate tensile strength. The calculated yield strength variation (assuming a=0.25(a_3) and assumption 3) is presented in Figure 9.4 as a function of hardness of pure Zr and fluence for UTS increase. At a dose rate of 1.99 dpa, the ultimate tensile strength increased by 106 MPA and hardness by 35 kgmm^{-2}. For the 1.14 Sn model, the UTS and hardness values are 96 MPa and 32 kgmm^{-2} respectively in Figure 9.5. A rapid increase is observed in both models after the dose rate of 3 x10^{24}.

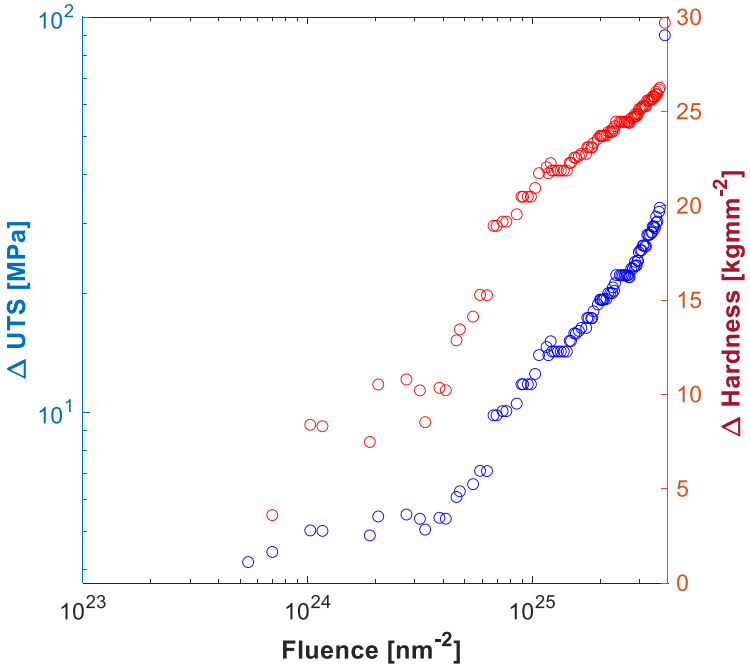

Figure 9.4: Ultimate tensile strength and hardness equivalent of the change in yield strength for the model pure Zr

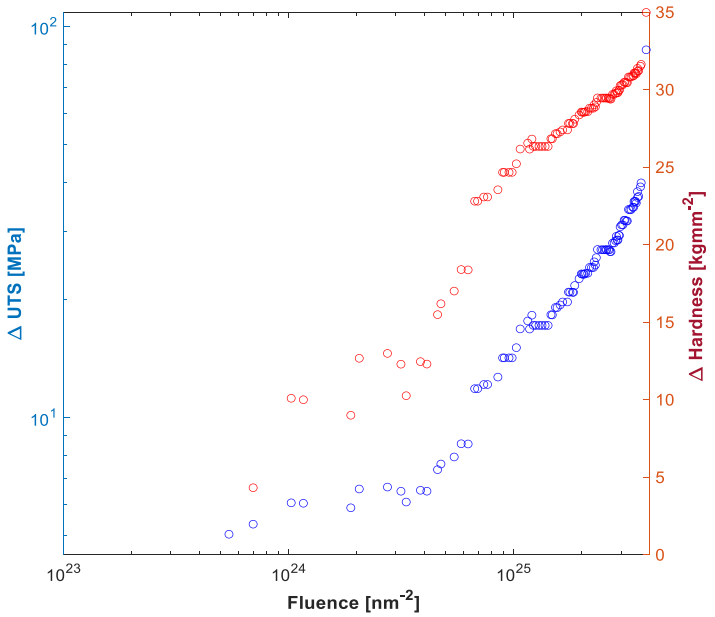

Figure 9.5: Ultimate tensile strength and hardness equivalent of the change in yield strength for the model 1.14% Sn- Zr

9.2.2 Dimensional Instability

In this section Simulated defect densities evaluated in terms of elongation. For this purpose, growth strain for both models at the reached dose was calculated. The calculation is performed using an analytical model of dislocation climb mechanism.

9.2.2.1 Parametrization

Several assumptions have been made to establish growth calculation as following:

Defect diffusion takes place anisotropically which means different diffusion parameters are implemented on basal and prism planes. Diffusion coefficients of vacancy (Dv) and interstitial (Di)at 630K was taken from Ref. [196] and [186]. Each sink is characterized by <a> and <c> axis because the origin of irradiation growth was assumed to be the DAD phenomenon. The dislocation loop sink strength (ρ) equation follow Golubov paper [182]. Also because of DAD effect on the sink strength, each sink is separated by two terms by axis direction.

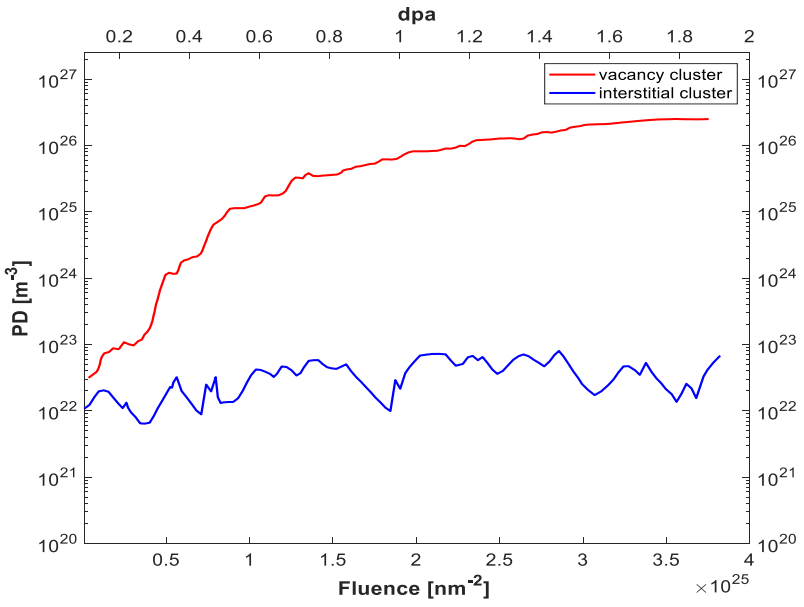

(a)

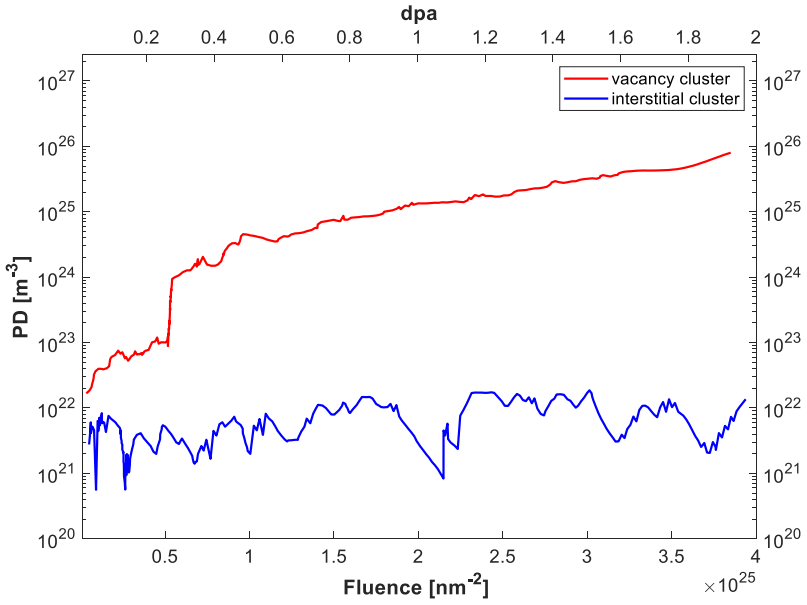

(b)

Figure 9.6: Point defect equivalents of total cluster densities in (a) for pure Zr model, (b) for 1.14%Sn-Zr model

The rv and ri are dislocation loop radius of vacancy and interstitial and Nv and Ni are dislocation loop number density of vacancy and SIA. And average strain factor (A) is growth strain proportional with <a> axis and <c> axis elongation. These parameters were taken from [195] can be seen in Table 9.3. The magnitude of the Burgers vectors for <a> loops is taken to be the same as <c> loops. Detailed parameter list can be seen in Table 9.3.

In order to implement in analytical model, Cluster densities of both models were calculated as their point defect equivalent densities. Figure 9.6a and 9.6.b provide point defect (Pd) densities as a function of fluence for Zr and 1.14% Sn models, respectively.

Table 9.3: Input parameters of the growth strain calculation

Diffusion coefficient[cm^2s^{-1}]	**Basal plane**	**Prism plane**	
Vacancy $\overline{D_v}exp\,(-\frac{0.9eV}{k_bT})$	8.16 x 10^{-9} [182]	5.87 x 10^{-9} [182]	
	5.08 x 10^{-16}	3.65 x 10^{-16}	
Interstitial $\overline{D_i}$=exp($-\frac{0.1eV}{k_bT}$)	4.7 x 10^{-6} [195]	3.5 x 10^{-6} [195]	
	7.44 x 10^{-7}	5.54 x 10^{-7}	
Burgers vector b[cm^{-2}]	3.23 × 10^{-8} [184]		
		Zr	Zr4
Sink strength ρ [cm^{-2}] $2\pi rN$	<a> SIA loop	3.27 x 10^9	4.34 x10^8
	<a> V loop	1.78 x 10^{12}	1.26x10^{12}
	<c> V loop	3.56 x 10^6	4.52 x 10^5
Average strain factor	<a> SIA loop	$Ailp$ Constant	0.5
	<a> V loop	$Avlp$ Constant	0.5
	<c> V loop	$Avlb$ Constant	1

9.2.2.2 Results of growth strain calculation

A distribution map of growth strain for the Zirconium pure model is presented in Fig 9.7. Since the growth calculation was performed directionally dependent, the distributions are provided as basal and prism plane. Accordingly, elongation in axial direction at 1.99 dpa (~3.89 x 10^{25} n/m^2) is 0.0098 %.

A uniform increase is seen in small doses. After the fluence value of 8 x 10 ^{24} n/m^{2,} elevation increases rapidly. The elongation at 1.99dpa (~3.89 x 10 ^{25} n/m^{2}) is 0.0113 % at <c> axis. In the result obtained, it is thought that the size of the defect diameters (25.2 nm) obtained in the c axis is effective, although the densities (4.7 x10^{17}) are very low. The elongation at 1.99dpa (~3.89 x 10 ^{25} n/m^{2}) is 0.0113 % at <c> axis. In the result obtained, it is thought that the size of the defect diameters (25.2 nm) obtained in the c axis is effective, although the densities (4.7 x10^{17} m^{-3}) are very low.

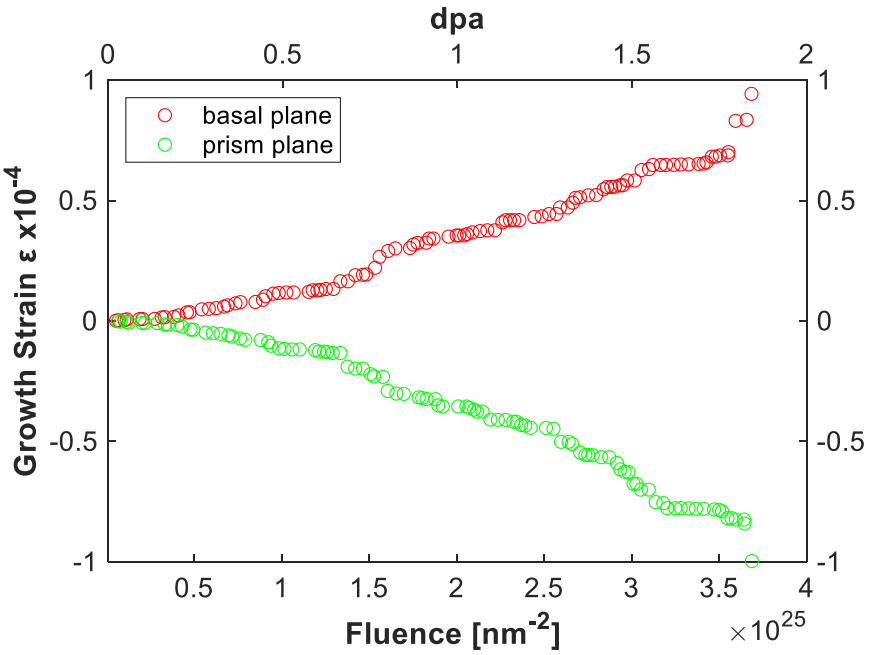

Figure 9.7: Irradiation growth as a function of fluence for pure Zr model

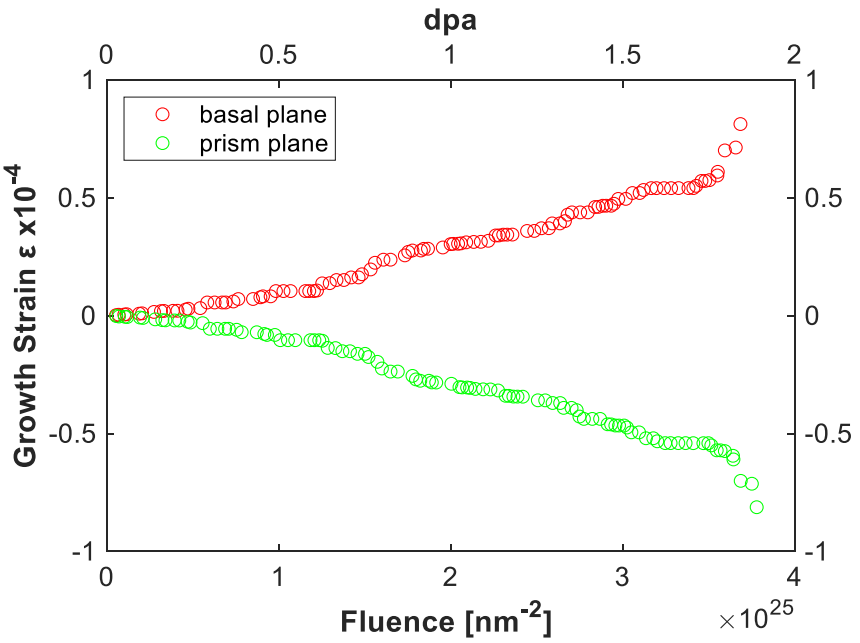

Figure 9.8: Irradiation growth as a function of fluence for 1.14%Sn-Zr model

The distribution map of growth strain calculated for the defect densities of 1.14%Sn-Zr can be seen in Fig 9.8. Elongation in axial direction at the reached fluence is 0.0083%. In this model, the effect could not be observed because the c loop concentration was too low ($>10^{14}$ m^{-3}) in the value obtained in the prism plane.

As a result, it can be said that the dominant factor in the growth trend is defect density as well as defect size. For different textures (i.e., annealed, cold work Zircaloy) the growth calculation contains differences. However, since the study aims to show the macroscopic effect of defect densities obtained with the multiscale model in terms of growth, the texture effect is not included in this section.

9.2.3 Macroscopic Behaviour on Storage Period

The aim of this section is to demonstrate the effect of the distributions obtained by rate theory modeling on macroscopic behavior. Using the above correlations, the hardening effect of the defect densities along all phases was evaluated. Obstacle densities and sizes are simulated loop densities and sizes. The change in yield strength was realized with the parameters in Table 9.4 by employing Assumption 3.

Several assumptions have been made to establish growth calculation as following:

Diffusion coefficients of vacancy (Dv) and interstitial (Di) were taken from Table 7.4. Each sink is characterized by <a> and <c> axis because the origin of irradiation growth was assumed to be the DAD phenomenon. The dislocation loop sink strength (ρ) equation follow Golubov paper [182]. Also because of DAD effect on the sink strength, each sink is separated by two terms by axis direction. The rv and ri are dislocation loop radius of vacancy and interstitial and Nv and Ni are dislocation loop number density of vacancy and SIA. And average strain factor (A) is growth strain proportional with <a> axis and <c> axis elongation. These parameters were taken from [195] can be seen in Table 9.5. The magnitude of the Burgers vectors for <a> loops is taken to be the same as <c> loops.

Table 9.4: Parameters for yield strength calculation

$\boldsymbol{\alpha_1}$	0.25
G	32.3 GPa
$\boldsymbol{b_{<a>}}$	3.23 A
$\boldsymbol{b_{<c>}}$	5.15 A
M	2

Figure 9.9 presents the rate theory resulted loop distributions in terms of yield strength and growth strain as a function of time. Right after discharge, the increase in yield strength of cladding material is 96 MPa. During storage period, annealing of defect densities causes a recovery on hardening which can be seen in Figure 9.9. After a period of 40 years, yield strength increment is roughly 25 MPa.

The resulting defect concentrations of storage period were implemented in the reduced version of the growth model. Growth strain at the beginning of storage was calculated as 0.01%. During the drying process, the growth strain was almost 6 times higher but in dry storage phase the growth strain decreased dramatically and recovered in the first 10 years at dry storage.

Table 9.5: Average Strain Factors

All storage phases			
Average strain factor	<a> SIA loop	*Ailp* Constant	0.5
	<a> V loop	*Avlp* Constant	0.5
	<c> V loop	*Avlb* Constant	1

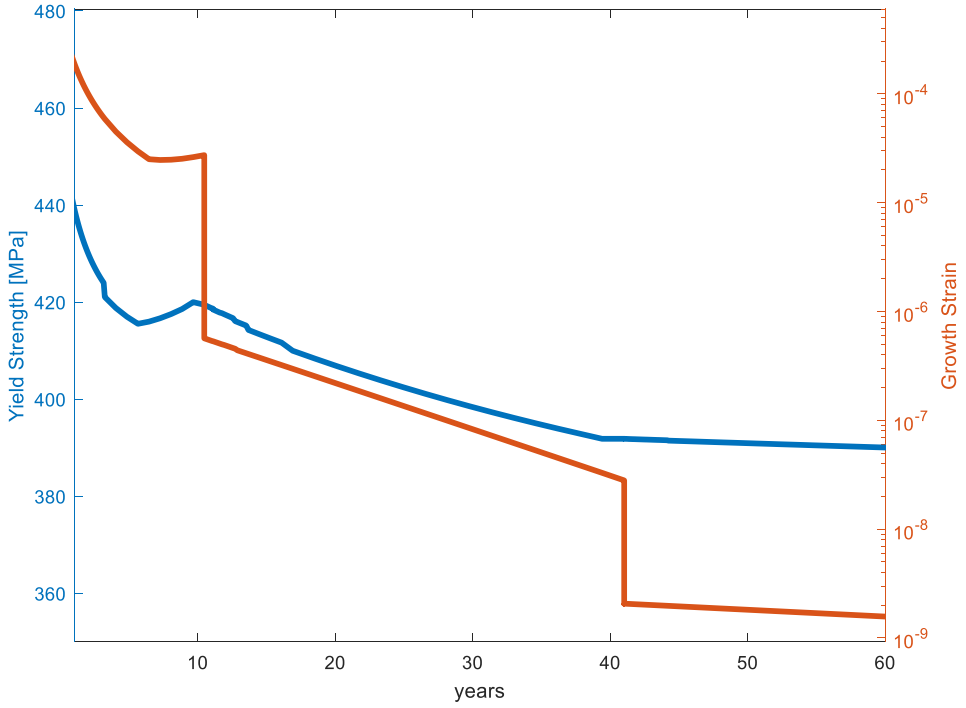

Figure 9.9: Time evolution of yield strength and growth strain during storage phases

10 The Effect of Variables

10.1 Effect of Temperature

As mentioned in introduction, main objective was developing a multi scale model to simulate radiation induced microstructure evolution in cladding material. Chapter 8 shows that this objective was achieved. It is now necessary to verify the quality of simulations. This can be done by measuring sensitivity to input parameters. In this section, the multiscale model is considered in terms of sensitivity to temperature, dose rate and alloy content and effect of these parameters is evaluated.

The multiscale model was run to simulate irradiation induced microstructure evolution on the cladding material at 3 temperatures: T = 573, 623, 673°K. The effect of finite grain size was introduced by adopting finite periodic boundary (FBC)conditions in all three directions. Damage accumulation was simulated using the Pure-Zr model and parametrized with the conditions in Table 10.1. The simulation box (a non-cubic block of Zirconium atoms with dimensions 97.2 x 98.5 x 99.1 nm^3 (lattice parameter a=3.24 Å)) is assumed to be at the center of a spherical grain. The simulations performed using a neutron spectrum at the core horizontal midplane with Oak Ridge HFIR operating at 85MW($\Phi_{E>1MeV} = 5 \times 10^{15} n \cdot cm^{-2} \cdot s^{-1}$) with a dose up to 0.1dpa (at a fluence of 5.48 x 10^{23} n/m^2). The list of kinetic parameters used in the present simulations and the description of the models can be found in Chapter 7. To insert the cascades corresponding to the HFIR PKA spectrum into the simulation box, the same procedure is used as described in Chapter 7, i.e., a new database of cascades of different PKA energies such that the fraction of cascades of a given PKA energy corresponds to the normalized fraction of recoils at the corresponding energy in the PKA spectrum. 1000 cascade events for each temperature at PKA energies between 1-65 keV created using MD simulations, was used to carry out this simulation.

Table 10.1: Simulation parameters

Simulation Parameters			
Flux		5 x10 ^{19}	n/m^{2}s, E≥ 1MeV
Dose rate		10 $^{-7}$	dpa/s
Grain Size		4	μm
		Vacancy	**Interstitial**
573°K	$D_{\parallel}$ [Ås^{-1}]	1.79 x10 ^{9}	3.44 x10 ^{10}
	$D_{\perp}$[Ås^{-1}]	1.84 x10 ^{10}	7.63 x10 ^{10}
623 °K	$D_{\parallel}$ [Ås^{-1}]	5.87 x10 ^{9}	5.54 x10 ^{10}
	$D_{\perp}$[Ås^{-1}]	5.06 x10 ^{10}	1.17 x10 ^{11}
673°K	$D_{\parallel}$ [Ås^{-1}]	1.28×10^{10}	7.53×10^{10}
	$D_{\perp}$[Ås^{-1}]	9.70×10^{10}	1.54×10^{11}

Figure 10.1a and b shows the density and size evolution of <a> type vacancy clusters which was chosen so as to show difference clearly since these are the most dominant defect type. The number density of the vacancy clusters increases as the irradiation temperature decreases. On the contrary, size of clusters increases with increasing temperature. Since increasing temperature increases defect mobility, it promotes recombination between defects and the tendency to agglomerate into large clusters, thus the results are consistent from the physical point of view. The simulated irradiation induced increases of yield strength are plotted versus the dose in Figure 10.1c. It can be noticed that the hardening increases as the irradiation temperature decreases, which shows that the model is sensitive to irradiation temperature. While the yield strength increase at the highest temperature value is expected to be the highest, the relatively highest increase at 0.1 dpa is observed at 623 °K. This is due to the superposition method used in the analytic correlation employed in the yield strength evolution. Figure 10.1d shows the axial elongation

correspondence of the simulated defect densities. At the dose value reached, the highest elongation is observed at 673°K with increasing temperature.

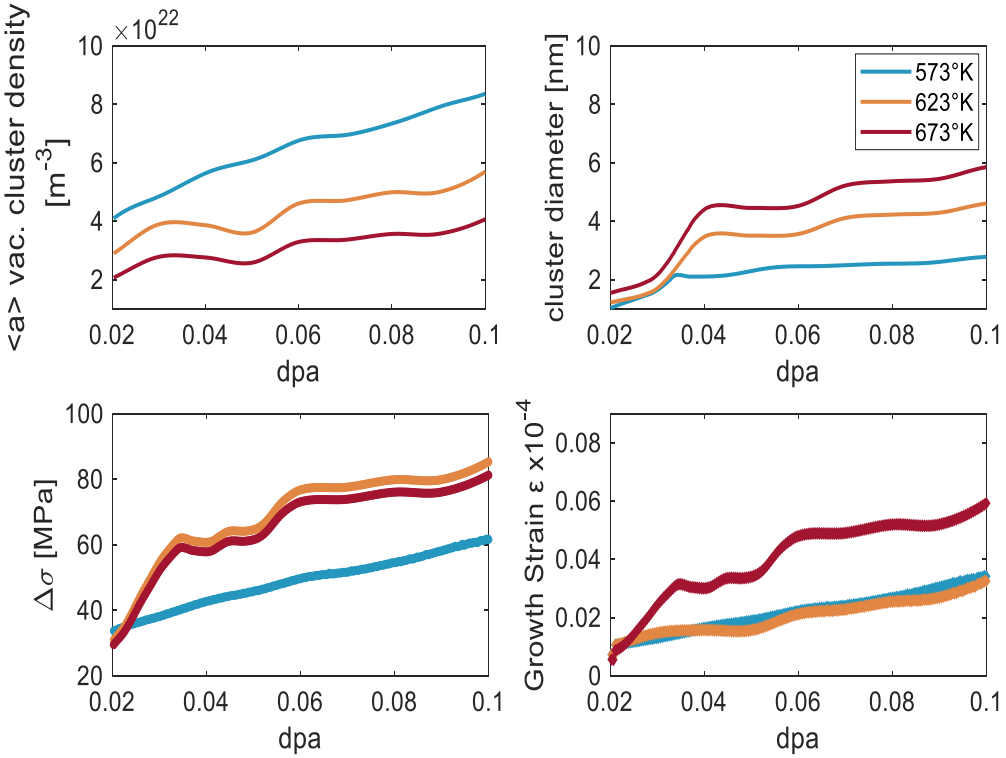

Figure 10.1: a: Total <a> type vacancy cluster densities, b. average cluster diameters, c. change in yield strength and d. growth strain (axial elongation) of the multiscale simulations at different temperatures as a function of dpa

10.2 Effect of Alloy Content

The multiscale model was run to simulate irradiation induced microstructure evolution on cladding material (Zr) containing 0%, 0.5% and 1.14% Sn. The effect of finite grain size was introduced by adopting finite periodic boundary (FBC)conditions in all three directions. To implement the effect of alloying element on damage accumulation, Sn is not treated discretely but in terms of concentration. Immobile Small interstitial clusters (<4) are randomly distributed and defined as traps for vacancy clusters in accordance with the concentration of 0, 0.5 and 1.14 % atomic of Sn. Parametrization conditions of three simulations are presented in Table 10.2. The simulation box (a non-cubic block of Zirconium atoms with

dimensions 194.4 x 197 x 198.2 nm^3 (lattice parameter a=3.24 Å)) is assumed to be at the center of a spherical grain. Three simulations were performed using a normalized neutron spectrum of a fuel assembly of a 3.8 GW LWR-P4 reactor in Paluel ($\Phi_{E>1MeV} = 6.26 \times 10^{13} n \cdot cm^{-2} \cdot s^{-1}$) with a dose up to 1 dpa (at a fluence of 5 x 10 ^{24} n/m^2).Irradiation temperature was taken as 630 °K. The list of kinetic parameters used in the present simulations and the description of the models can be found in Chapter 7. To insert the cascades corresponding to the PWR PKA spectrum into the simulation box, the same procedure is used as described in Chapter 7. 1000 cascade events for each alloy content at PKA energies between 1-65 keV created using MD simulations, was used to carry out this simulation.

Table 10.2: Simulation parameters

Simulation Parameters		
Temperature	630	°K
Flux	6.26 x10 ^{17}	n/m^2s, E≥1MeV
Dose rate	10^{-6}	dpa/s
Grain Size	4	μm
	Vacancy	**Interstitial**
$D_{\parallel}$ [$Å s^{-1}$]	5.87 x10 ^{9}	5.54 x10 ^{10}
$D_{\perp}$[$Å s^{-1}$]	5.06 x10 ^{10}	1.17 x10 ^{11}

Figure 10.2a and b show the evolution of <a> type vacancy cluster densities and cluster radius as a function of dose. The number densities are getting decrease with increasing alloy content. The SIA clusters (containing 4 SIAs), which were implemented in the model in the initial state to mimic the Sn content, recombine with vacancy clusters, resulting in a lower number of clusters as the alloy content increases. Since Sn content suppresses the defect density, the comparison with the experimental results shows that this effect is implemented in accordance with the experimental results. Likewise, increasing the amount of recombination decreases

the number of agglomerated clusters in large clusters and as a result, the cluster size relatively decreases as the alloy content increases. The simulated irradiation induced increases of yield strength are plotted versus the dose in Figure 10.2c. It can be shown that the hardening decreases with the Sn content, which shows that the multiscale model is sensitive to the alloy content. Figure 10.2d shows the elongation correspondence of the simulations. With increasing alloy content, growth strain slightly decreases.

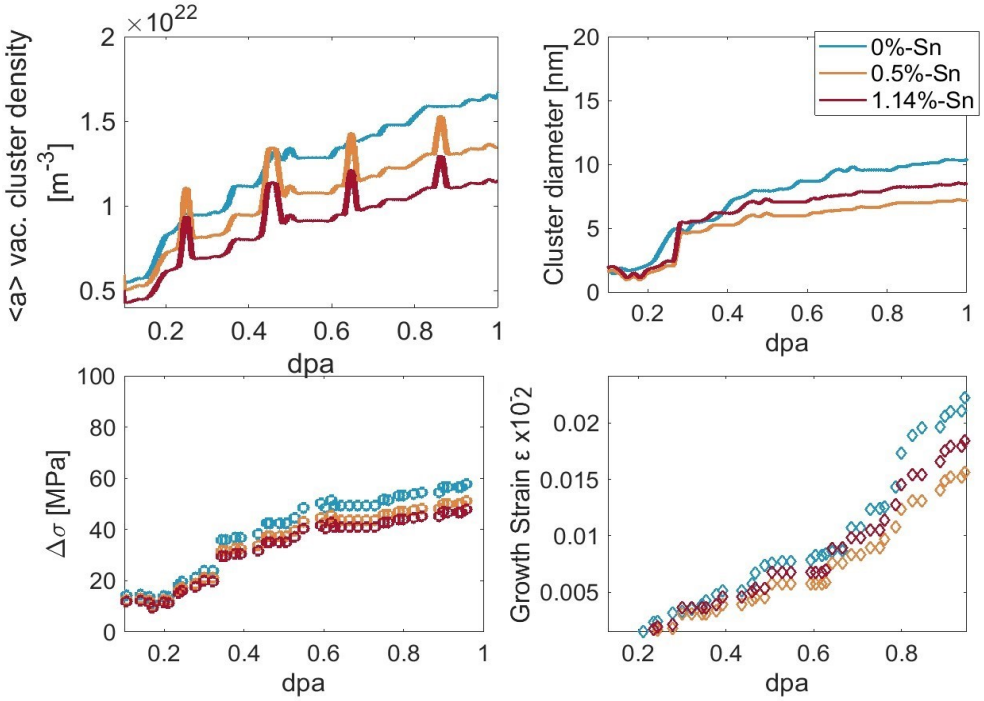

Figure 10.2: a: Total <a> type vacancy cluster densities, b. average cluster diameters, c. change in yield strength and d. growth strain (axial elongation) of the multiscale simulations with different alloy contents as a function of dpa

10.3 Effect of Dose Rate

The multiscale model was run to simulate irradiation induced microstructure evolution on cladding material (Zr) with three dose rates: 10^{-6}, 10^{-7} and 10^{-8} dpa/s. The effect of finite grain size was introduced by adopting finite periodic boundary (FBC)conditions in all three directions. Damage accumulation was simulated using the Pure-Zr model and parametrized with the conditions in Table 10.3. The simulations performed using a neutron spectrum at the core horizontal midplane

with Oak Ridge HFIR operating at 85MW($\Phi_{E>1MeV} = 5 \times 10^{15} n \cdot cm^{-2} \cdot s^{-1}$) with a dose up to 1dpa. The irradiation temperature was taken as 630 °K. The simulation box (a non-cubic block of Zirconium atoms with dimensions 194.4 x 197 x 198.2 nm^3 (lattice parameter a=3.24 Å)) is assumed to be at the center of a spherical grain. The list of kinetic parameters used in the present simulations and the description of the models can be found in Chapter 7. 1000 cascade events for each alloy content at PKA energies between 1-65 keV corresponding to the HFIR PKA spectrum created using MD simulations, was used to carry out this simulation.

Table 10.3: Simulation parameters

Simulation Parameters		
Temperature	630	°K
Flux	5 x10 ^{19}	n/m^2s, E≥ 1MeV
Grain Size	4	μm
	Vacancy	**Interstitial**
$D_{\parallel}$ [$Å s^{-1}$]	5.87 x10 ^{9}	5.54 x10 ^{10}
$D_{\perp}$[$Å s^{-1}$]	5.06 x10 ^{10}	1.17 x10 ^{11}

Number density of vacancy clusters and cluster size as a function of dose are presented in Figure 10.3a and b, respectively. It can be observed that the multiscale model is sensitive to the dose rate: amount of vacancy clusters increases as the dose rate increases. It can also be observed that the dose rate dependence tends to decrease with decreasing dose rate. With the decreasing dose rate, the size of clusters is getting bigger. It shows that the decreasing dose rate causes an increase in agglomeration of clusters. This finding also explains the decrease in number density with decreasing dose rate. The simulated irradiation-induced increases of yield strength are plotted versus the dose in Figure 10.3c. At dose rate 10^{-6} and 10^{-7} the increase in hardening is nearly the same. The increase in hardening caused by the simulation result with a dose rate of 10^{-8} shows that there is a slight increase in

hardening as the dose rate decreases. Figure 10.3d shows the elongation correspondence of simulations. The elongation caused by 3 different dose rates shows a similar trend. The minor change seen between the dose rates 10^{-8} and 10^{-6} (0.023 to 0.027 %) indicates that the results are sensitive to the dose rate.

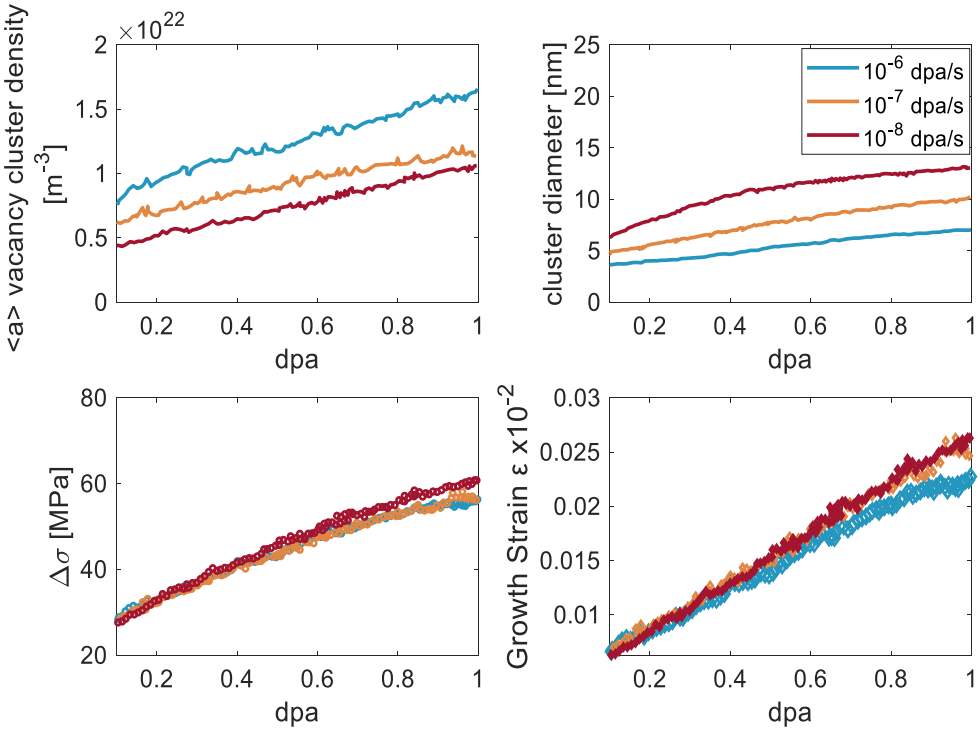

Figure 10.3: a: Total <a> type vacancy cluster densities, b. average cluster diameters, c. change in yield strength and d. growth strain (axial elongation) of the multiscale simulations at different dose rates as a function of dpa

Regarding the individual defect types, cluster density distributions at reached fluence were evaluated for three dose rates which can be seen in Figure 10.4 and 10.5 and 10.6. The following was observed when all dose rates were considered: <a> type vacancy clusters are the dominant defects in all simulations. In <a> type vac clusters, there was a relative decrease in defect diameters as the dose rate increased. in terms of number density, the decrease in dose rate resulted in a higher number of defects.

The low density of the <c> type can be compared to the relatively high emission capacity of the vacancy type <a> loops due to their low binding energy. The emitted vacancies are then redistributed in the system. Interstitial clusters can be seen in relatively low density and with low sizes. The typical characteristics of the

microstructure are similar; number of accumulated clusters along (0001) plane is lower than the ((11$\bar{2}$0)) due to the directional diffusion anisotropy. The cluster size increases with increasing dose, and that the spatial ordering of bigger clusters (>2nm) along ((11$\bar{2}$0)) planes becomes clearer. A closer look at the projections reveals that relatively bigger clusters have the tendency of ordering along ((11$\bar{2}$0)) plane. In the <c>-type vacancy clusters, a decrease in dose rate from 10^{-6} to 10^{-7} leads to a decrease in diameter and a significant increase in density. A decrease in dose rate from 10^{-7} to 10^{-8} leads to a significant increase in diameter and a decrease in defect density. Considering each simulation, it is seen that the number of defects formed leads to a decrease in defect density and an increase in defect diameter as the decrease in dose rate becomes significant. <a>type Interstitial clusters agglomerate into groups smaller in diameter than <a> vacancy type clusters due to their high defect mobility. In this type of cluster, it is observed that the average diameter increases as the dose rate decreases.

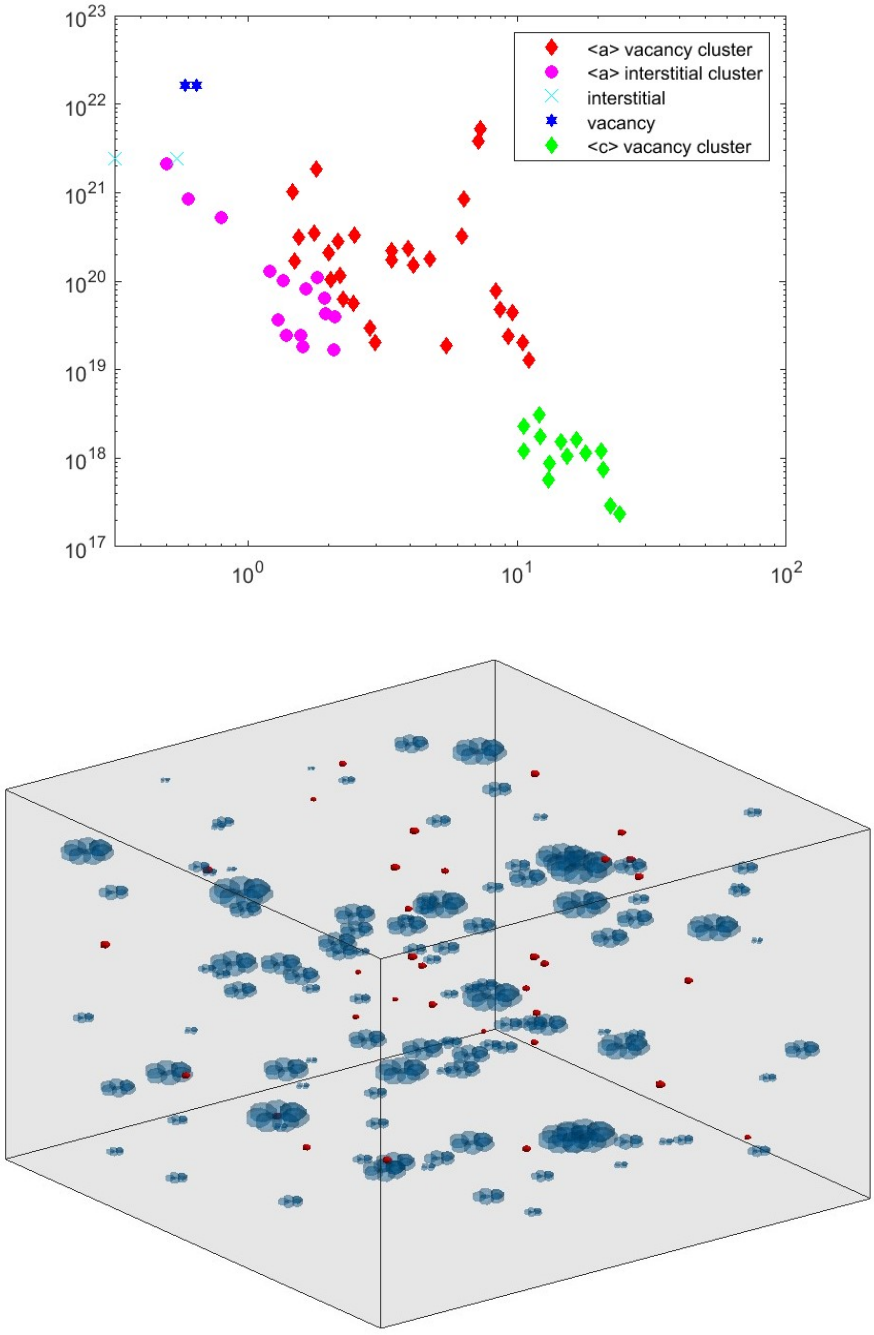

Figure 10.4: a: size and density distribution of microstructures, b: configurations (blue cluster are <a> type vacancy clusters and red spheres are <a> interstitial clusters for the pure Zr model with respect to defect type at dose rate 10^{-6} dpa/s

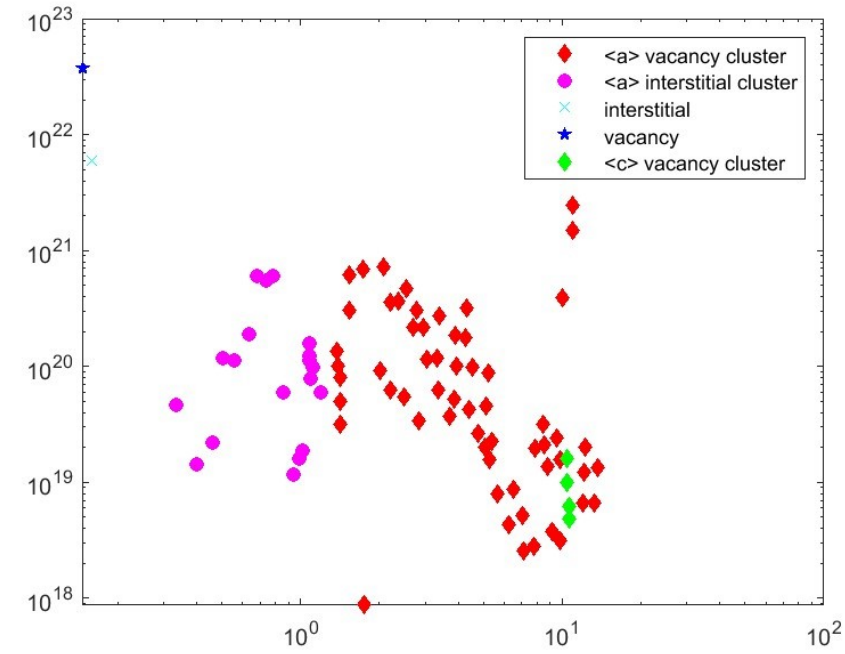

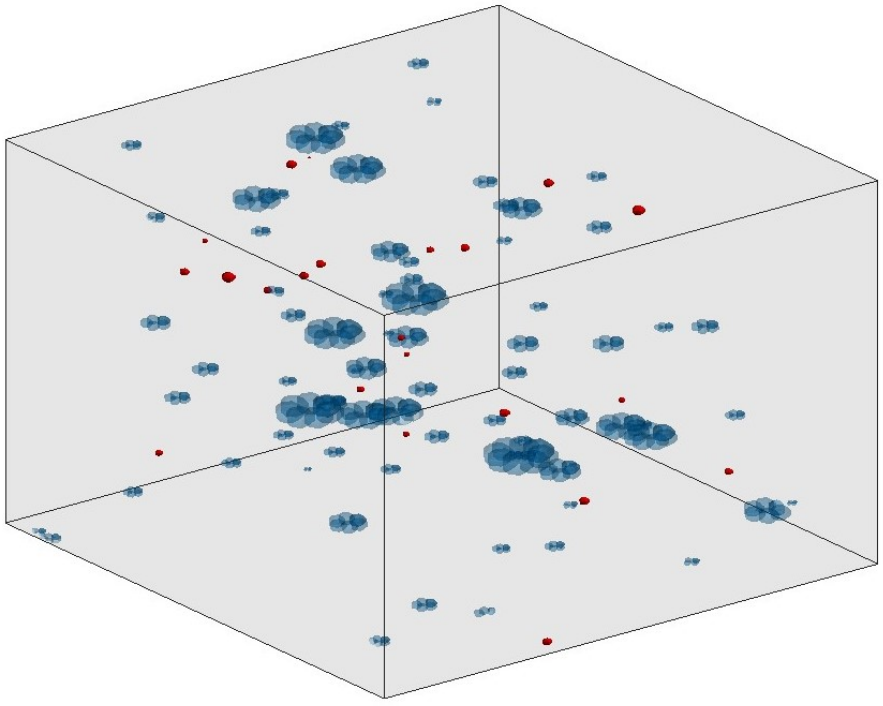

Figure 10.5: a: size and density distribution of microstructures, b: configurations (blue cluster are <a> type vacancy clusters and red spheres are <a> interstitial clusters for the pure Zr model with respect to defect type at dose rate 10^{-7} dpa/s

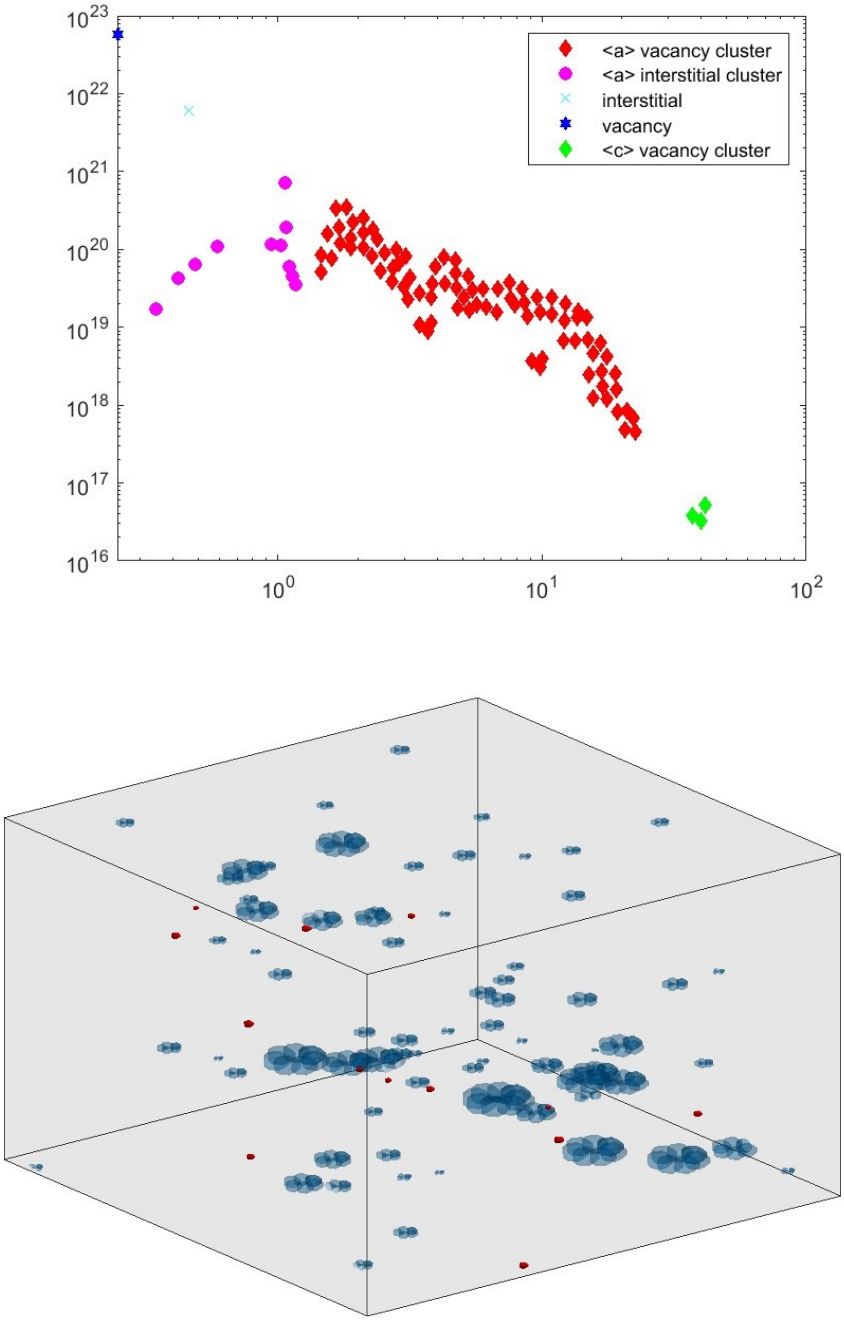

Figure 10.6: a: size and density distribution of microstructures, b: configurations (blue cluster are <a> type vacancy clusters and red spheres are <a> interstitial clusters for the pure Zr model with respect to defect type at dose rate 10^{-8} dpa/s

11 Validation of Multiscale Model

11.1 Multiscale Simulation of The Experiments: Density and Size Distribution

Experimental observations are used to test the capability of the multiscale method. Transmission electron microscopy (TEM) irradiation experiments allow real-time observation of irradiation damaging process under well-controlled conditions and provide unique data to benchmark kinetic models of defect production and agglomeration the driving force behind various irradiation effects on materials microstructure and mechanical properties. Therefore, for validation, OKMC simulations parametrized by experiments including TEM studies are performed in this section. The resulting structures in terms of concentration and size are compared with TEM results from published experimental studies (Figure 11.1). Finally, the macroscopic effect of the resulting structures is compared with structural measurements.

Multiscale simulations were performed the condition of experiments selected from Chapter 3.2 aim at evaluating the resulted cluster density and size distributions with the measured distributions of microstructures. The simulation box (a non-cubic block of Zirconium atoms with dimensions 194.4 x 197 x 198.2 nm^3 (lattice parameter a=3.24 Å)). Boundary conditions are described in detail in 5.3.2.2. The list of kinetic parameters used in the present simulations and the

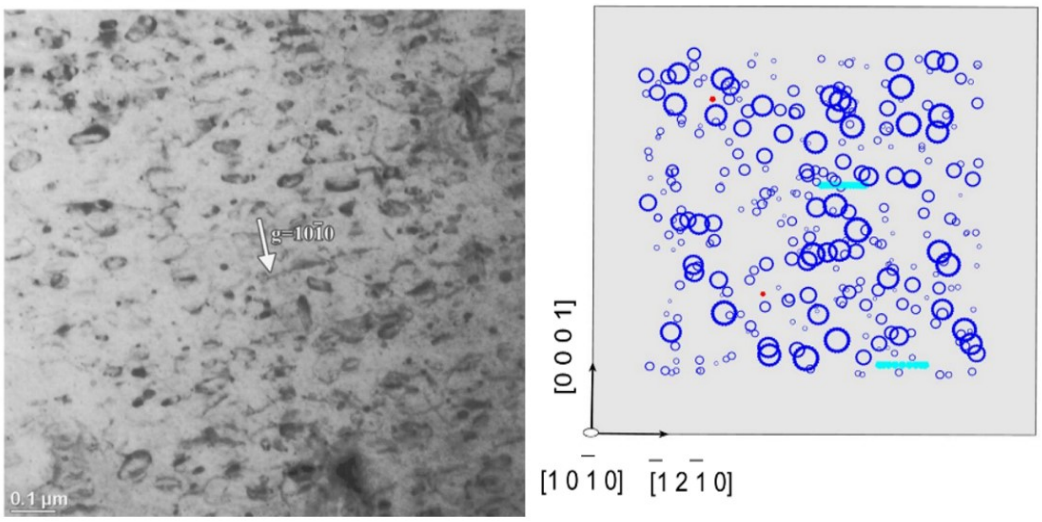

Figure 11.1: TEM image of dislocation loops from alpha-annealed Zircaloy-4 irradiated at nominally 630 °K [73] and the simulated microstructure at same temperature and fluence

description of the models is provided in 7.1.3. Damage accumulation is simulated using the material and irradiation conditions with the Zr-pure model in Table 11.1 and with the 1.14%Sn-Zr model in Table 11.2 and Table 11.3.

To compare with the measurements from transmission electron microscopy (TEM), simple filters are applied to discard the defects that are most likely too small to be resolvable by this technique. For this purpose, vacancy clusters containing less than 50 vacancies (1.15 nm), are ignored, while the others are assumed to be visible to the TEM. All visible <a> type interstitial and clusters were calculated as <a> loop and <c> type vacancy clusters were excluded from the evaluation due to exceptionally low densities of <c> loops in experimental evidence.

Table 11.1: Simulation parameters

	Case 1		**Case 2**	
Temperature [K]	573		623	
Material	Zirconium -pure			
Fluence [n/m^{2}]	5.3×10^{23}		5.3×10^{23}	
Dose rate [dpa/s]	3.56 x10 $^{-4}$		4 x10 $^{-4}$	
Grain Size [μm]	16			
	Vacancy	**Interstitial**	**Vacancy**	**Interstitial**
$D_{\parallel}$ [Ås^{-1}]	1.79 x10 ^{9}	3.44 x10 ^{10}	5.12 x10 ^{9}	5.25 x10 ^{10}
$D_{\perp}$[Ås^{-1}]	1.84 x10 ^{10}	7.63 x10 ^{10}	4.51 x10 ^{10}	1.12 x10 ^{11}
Ref.	[61]			

Figure 11.2 shows visible <a> loop densities as a function of fluence(dose) for Case 1 and Case 2 in which the Zr-Pure model is used. Experimental data derived from Ref. [61] can be seen as red dots. Comparing Case 1 with Case 2, at first glance, it is clearly seen that under constant dose, the cluster density decreases as the temperature increases, whereas the loop size increases. This finding is in agreement with the experimental data. At 573 K, the Pure-Zr model show a qualitative match to experimental results of Ref. [61]. The model overpredicts the loop density as the temperature increases. At the achieved dose value ($5.3\text{x}10^{23}$ n/m^{2}) Overall, the experimental loop sizes are ~5 times larger than the resulted loop sizes.

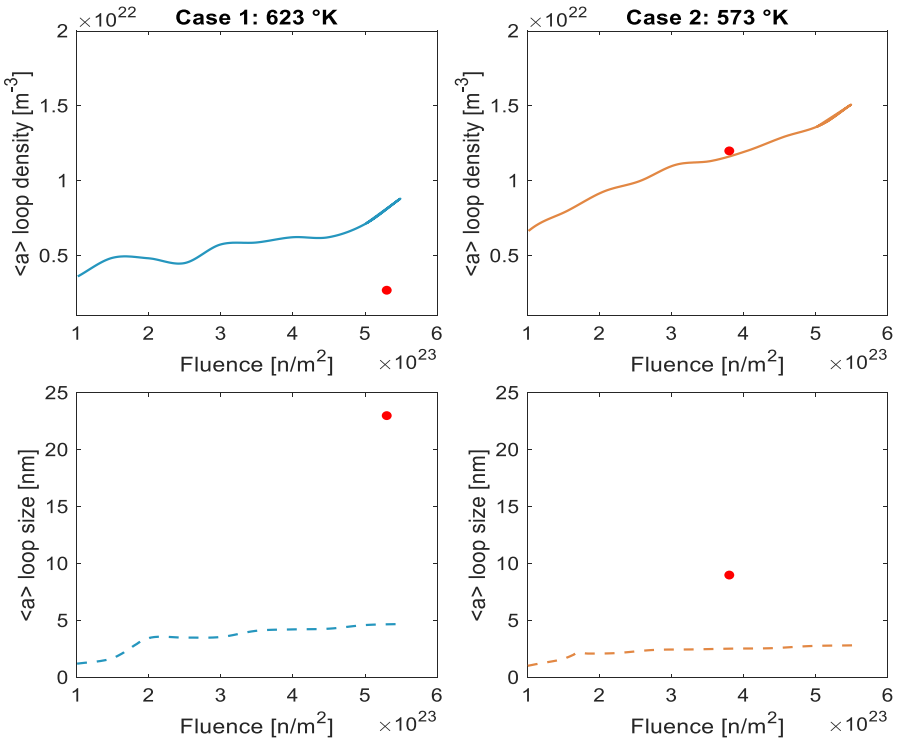

Figure 11.2: Microstructure evolution (processed for TEM comparison) in Zr predicted by the OKMC model (lines) for case 1 and case 2. The points are experimental data from [61].

Figure 11.3 shows visible <a> loop densities as a function of fluence(dose) for Case 3 and Case 4 in which the 1.14%Sn-Zr model is used. Experimental data derived from Ref. [73] can be seen as green dots. For both cases, the predictions regarding the size of <a> loops present an agreement with the measured sizes. in case 3, the model predicts a saturation in visible loop density at the reached fluence (5.5 $x10^{24}n/m^2$). The cause of this is likely related to the treatment of cascade-defect interaction. In particular, the assumption of random combination between cascade defects and pre-existing defects during cascade events does not account for effects that may occur in irradiated metals such as the break-up of large defect clusters by cascades. Same saturation can be observed in Case 4. After a fluence value of $13x10^{24}$ increase in loop density elevates. The overestimation at fluence $2.93x10^{25}$ is about a factor 1.5, but it is about 1.2 order of magnitude for the lower doses (at $5.5x10^{24}$ n/m^2).

Table 11.2: Simulation parameters

	Case 3	**Case 4**
Temperature [K]	630	
Material	Zircaloy-4	
Fluence [n/m$^{2]}$	5.50×10^{24}	2.93×10^{25}
Dose rate [dpa/s]	7.40 x10 $^{-7}$	6.69 x10 $^{-7}$
Grain Size [μm]	15.2	
	Vacancy	**Interstitial**
$D_{\parallel}$ [$Å s^{-1}$]	5.87 x10 ^{9}	5.54 x10 ^{10}
$D_{\perp}$[$Å s^{-1}$]	5.06 x10 ^{10}	1.17 x10 ^{11}
Ref.	[73]	

Figure 11.4 shows visible <a> loop densities and sizes as a function of fluence(dose) for Case 5 and Case 6 in which the 1.14%Sn-Zr model is used. Experimental data derived from Ref. [54] can be seen as red dots. At the simulated temperature 673K, the number density of the loops agrees with the experimental data for case 5. The predicted size of the loops seems to match the experimental evidence at low doses (case 5), and slightly differs from the averaged measurement at higher doses (case 6). The overestimation of loop densities at fluence $3x10^{25}$ n/m^2 is about 4 times These discrepancies can be explained by the trap effect of impurities in Zircaloy-4. They are able to localize vacancy clusters nearby thyself playing a role of traps for vacancy clusters; therefore, it may cause the suppression in loop densities in the experimental evidence. The discrepancies suggest that the model should include a full description of impurities in Zircaloy-4.

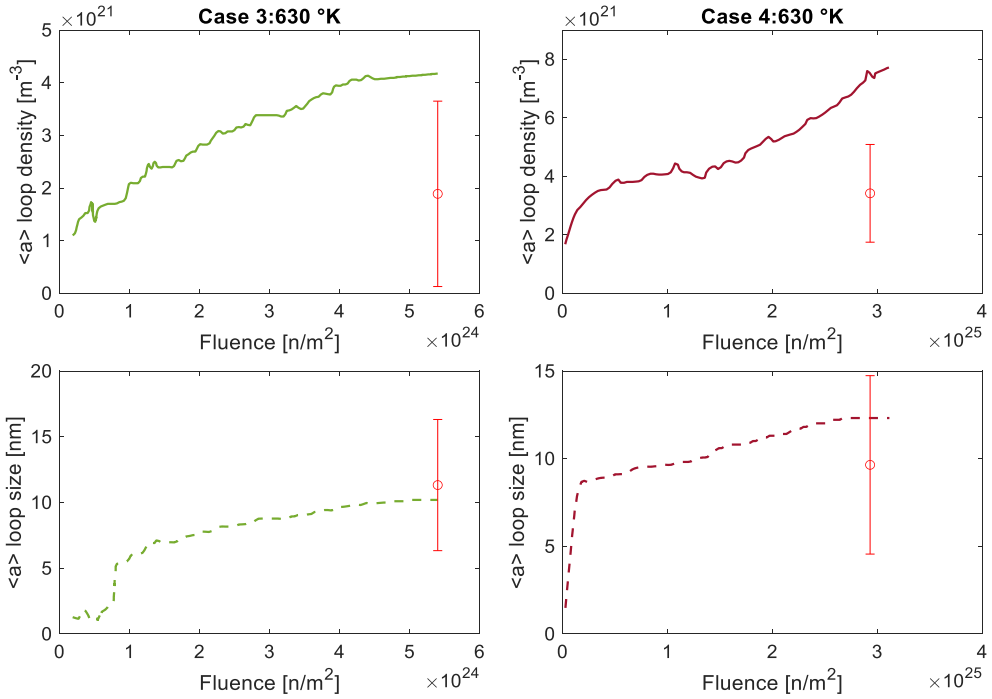

Figure 11.3: Microstructure evolution (processed for TEM comparison) in Zr predicted by the OKMC model (lines) for case 3 and case 4. Error bars are experimental data from [73].

Table 11.3: Simulation parameters

	Case 5	**Case 6**
Temperature [K]	673	
Material	Zircaloy-4	
Fluence [n/m^{2}]	8.1×10^{24}	3×10^{25}
Dose rate [dpa/s]	5.31 x10 $^{-8}$	1.94 x10 $^{-7}$
Grain Size [µm]	15.2	
	Vacancy	**Interstitial**
$D_{\parallel}$ [Ås^{-1}]	1.28×10^{10}	7.53×10^{10}

$D_{\perp}[\text{Å}s^{-1}]$	9.70×10^{10}	1.54×10^{11}
Ref.	[54]	

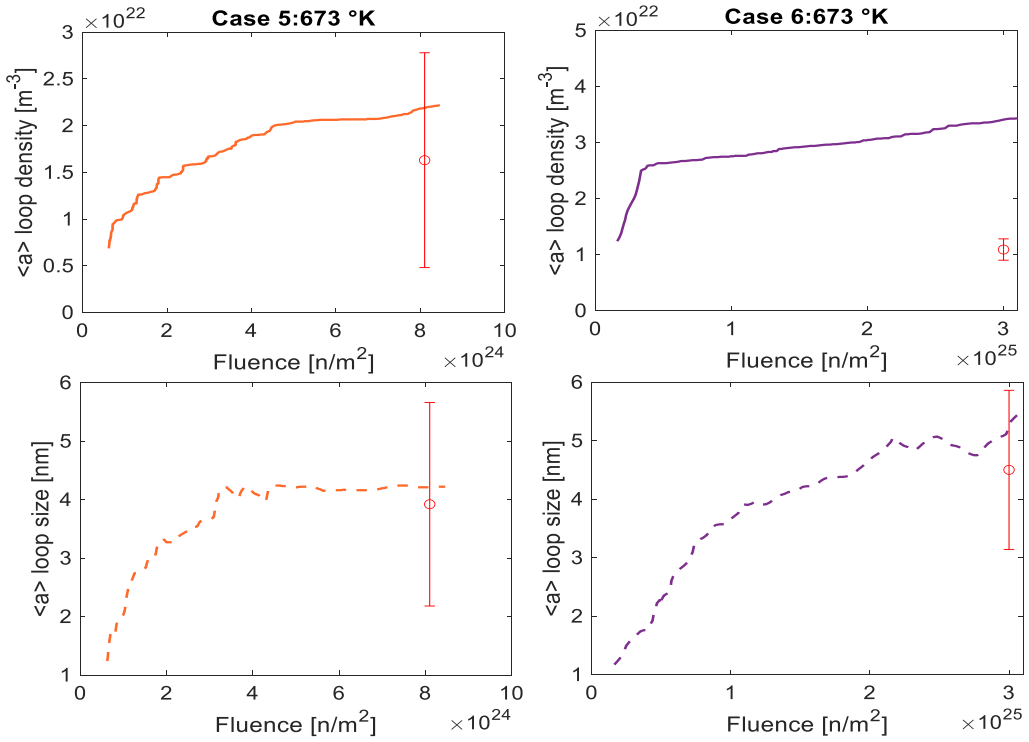

Figure 11.4: Microstructure evolution (processed for TEM comparison) in Zr predicted by the OKMC model (lines) for case 5 and case 6. Error bars are experimental data from [54].

11.2 Macroscopic Deformation Effect

In this section, the macroscopic effect of cluster densities obtained from experimentally conditioned case simulations is evaluated in terms of yield strength and elongation and compared with structural measurements obtained under the same conditions.

11.2.1 Change in Yield Strength

Determination of yield strength change is performed by employing Orowan correlation with the first assumption which accepts that all defect clusters (vacancy and interstitials) are obstacles that increase hardening. Parameters used for the calculation are given in Table 11.4. the strength of the individual barriers (a) was taken 0.25 since it's more typical value in most cases.

Table 11.4: Parameters for the calculation of the yield strength

$\boldsymbol{\alpha_1}$	0.25
G	32.3 GPA
$\boldsymbol{b_{<a>}}$	3.23 A
$\boldsymbol{b_{<c>}}$	5.15 A
M	2

Figure 11.5.a shows the change in yield strength of the 1.14% Sn model as a function of fluence. For case 3, the yield strength increases to 225MPa at a fluence of $5.5x10^{24}$ n/m^2. At the same temperature, at the fluence reached ($3x10^{25}$n/m^2) the resulting density of case 4 is 280 MPa. The increase in yield strength with higher temperature in cases 5 and 6 is almost 2 times higher than the cases at 630 K. The effect of increasing cluster sizes on the calculation rather than decreasing cluster densities with increasing temperature is evident in this finding. The fluence value reached in case 6 shows the highest yield change with 510 MPa. Considering the measurements of the yield strength of unirradiated Zircaloy-4 (which is 365MPa) in Ref. [73] the yield strength increases by %40.

Fig. 11.5.b shows that a great match between measured and calculated irradiation hardening is generally observed for case 3 and 5 at low fluences. In Case 4 and 6 a divergence from the measured value is observed at high fluences. With increasing temperature, the predictions of case 6 are far away from the measured value. It can be concluded that the reason is the overestimation of defect density in case 5.

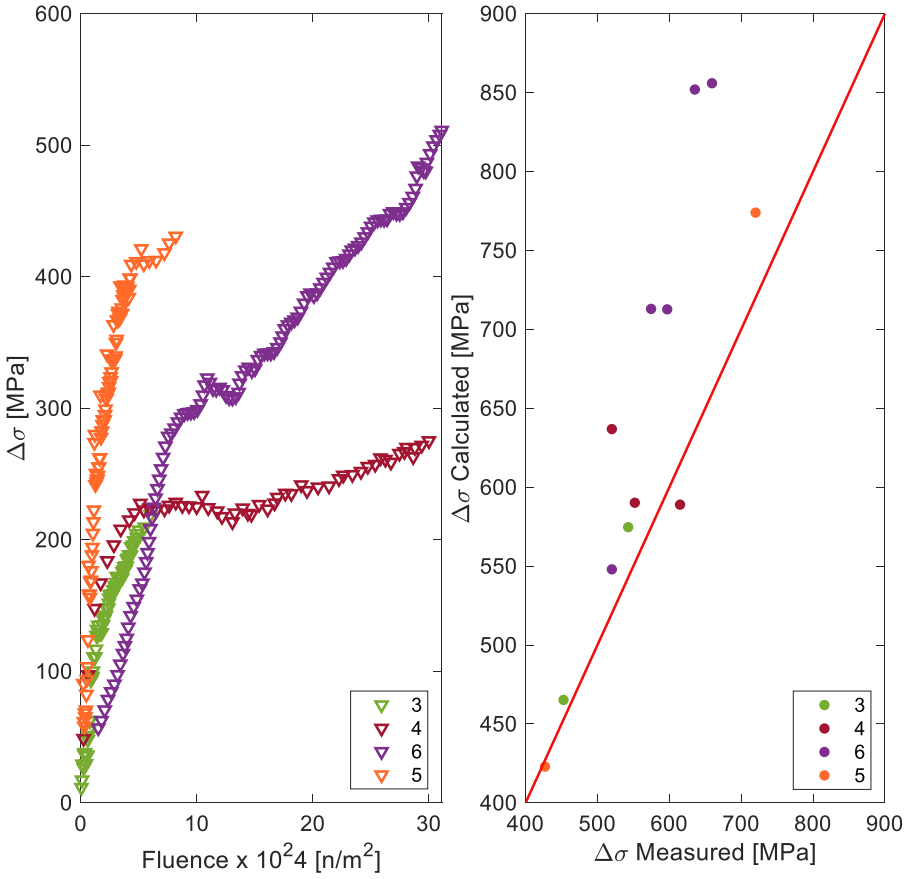

Figure 11.5 a and b: Change of yield strength as a function of fluence for different cases, b. Diagram of measured and calculated change of yield strength. The measured values are taken from Ref. [54,73].

11.2.2 Growth Calculation

Regarding experimental conditions, growth calculation was parametrized for each case. The dislocation loops strength and point defect equivalent densities of clusters were calculated from the resulted simulations. Detailed parameter list of the cases can be seen in Table 11.5. Growth strain was calculated using the parameters with the Zr-pure model in Table 11.5 and with the 1.14%Sn-Zr model in Table 11.6.

For the Zr-pure model, the growth strain as a function of dose is presented in Figure 11.6. The results are compared with experimental measurements by Rogerson [93] in Figure 11.6. The growth strain calculated at 553°K (Case 1) shows a particularly

good agreement when the density of the objects in terms of the density of point defects is related. The growth strain at the reached fluence value is 0.01×10^{-4}. For Case 2 (at 623°K), although the calculated growth values are below the measurements taken at the same temperature, the trend obtained and the observation of the growth break phenomenon after 4.2×10^{24} agree with Rogerson's results.

Table 11.5: Input parameters for the calculation of the growth strain in the pure Zr model

Diffusion coefficient		**573°K**	**623°K**
Vacancy $D_v e\exp\left(-\frac{0.9eV}{k_bT}\right)$	Basal plane	5.62×10^{-14}	2.43×10^{-13}
	Prism plane	4.18×10^{-14}	1.81×10^{-13}
Interstitial $\bar{D}_\iota = \exp\left(-\frac{0.1eV}{k_bT}\right)$	Basal plane	1.07×10^{-09}	1.26×10^{-09}
	Prism plane	7.73×10^{-10}	9.10×10^{-10}
Burgers vector b[cm^{-2}]	3.23×10^{-8}		
		Case 1	**Case 2**
Sink strength ρ [cm^{-2}] $2\pi rN$	<a> SIA loop	5.22×10^{8}	3.87×10^{9}
	<a> V loop	6.27×10^{10}	1.37×10^{11}
	<c> V loop	-	-
Average strain factor	<a> SIA loop	0.5	
	<a> V loop	0.5	
	<c> V loop	1	

Table 11.6: Input parameters for the calculation of the growth strain in the 1.14% Sn-Zr model

Diffusion coefficient		**630°K**		**673°K**	
Vacancy $D_v exp\ (-\frac{0.9eV}{k_bT})$	Basal plane	$5.08x10^{-16}$		$8.45x10^{-13}$	
	Prism plane	$3.65x10^{-16}$		$6.29x10^{-13}$	
Interstitial $\overline{D_i}$=exp($-\frac{0.1eV}{k_bT}$)	Basal plane	$7.44x10^{-7}$		$1.45x10^{-9}$	
	Prism plane	$5.54x10^{-7}$		$1.05x10^{-9}$	
Burgers vector b[cm^{-2}]	3.23×10^{-8}				
		Case 3	**Case 4**	**Case 5**	**Case 6**
Sink strength ρ [cm^{-2}] $2\pi rN$	<a> SIA loop	$4.98x10^{9}$	$5.81x10^{9}$	$5.25x10^{9}$	$6.36x10^{9}$
	<a> V loop	$6.81x10^{10}$	$1.46x10^{11}$	$3.79x10^{11}$	$3.69x10^{11}$
	<c> V loop	-	$6.36\ x10^{8}$	$3.11\ x10^{5}$	$4.75\ x10^{12}$
Average strain factor	<a> SIA loop	0.5			
	<a> V loop	0.5			
	<c> V loop	1			

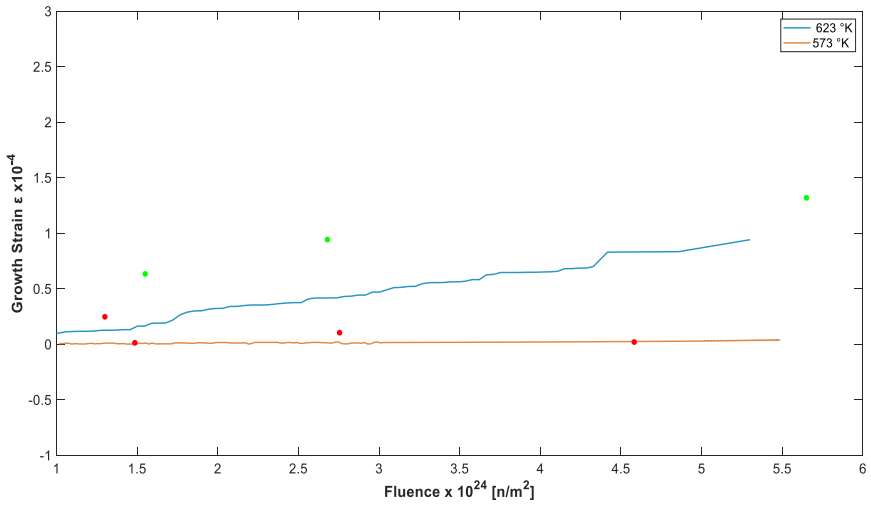

Figure 11.6: Growth elongation as a function of dose for case 1 (573 K) and case 2 (623 K). Red dots (573 K) and green dots (623 K) derived from experimental data in Ref. [93,197].

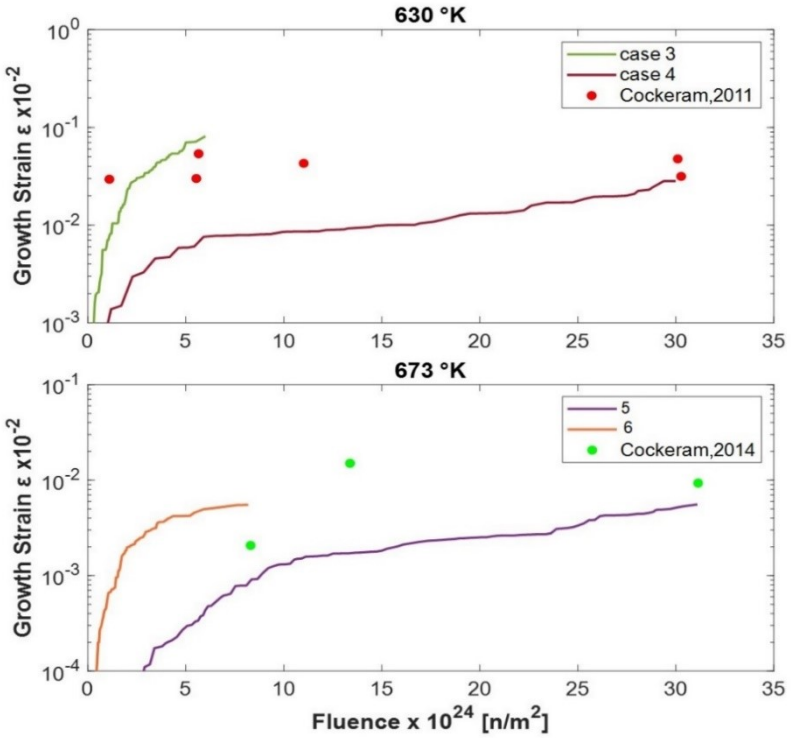

Figure 11.7: Growth elongation as a function of dose for cases 3, 4, 5, and 6. The red dots and green dots were derived from experimental data in Ref [73] and [54], respectively.

For the 1.14 Sn-Zr model, the growth strain as a function of dose is presented for Case 3-6 in Figure 11.7. The results are compared with experimental measurements obtained from [73].Although the experimental values of the growth strain are lower than the calculation data at 5.5 x 10^{24} n/m^2, the calculated strain at the dose reached in case 3 is 0.08%. At the higher dose reached in case 4, the model correctly calculates the calculated strain. In the data of cases 5 and 6 performed at 673 K, the predictions are below the predictions, but at the higher dose level in case 4 the results are closer to the experimental data. The overall growth trend is similar to the experimental data.

12 Conclusions and Outlook

12.1 Summary and Conclusions

It is anticipated that the planned periods of interim storage of spent fuel elements will be exceeded, requiring an extension of the safety case to potentially more than 60 years. Due to these circumstances, the investigation of radiation damage and, therefore, the structural integrity of spent fuel assemblies is of utmost importance for further safety statements regarding long-term interim storage. To assess macroscopic deformation in irradiated materials, it is highly recommended to simulate the radiation-induced microstructure. The nature of radiation damage accumulation, however, is multiscale. As a result, different physical laws govern system evolution at different scales. The simulation range must be extended at all scales, the information lost during transmission between scales must be reduced. In addition, the evolution rules of microstructures must be understood from the atomic level up. Scale and time constraints limit the models, even for zirconium and its alloys, the leading cladding tube material. Therefore, the existing work was initiated and undertaken aiming at investigating the irradiation damage evolution process based on a multiscale method and explain the structural and mechanical behavior of the spent fuel elements in condition of prospective prolonged interim storage.

A computationally efficient modeling sequence compatible with multistage damage mechanisms was developed in a step-by-step procedure: the effect of the radiation field on the lattice structure of the cladding material using a Monte Carlo simulation method. A second step involves generating damage in a lattice structure using a primary knock-on atom and analyzing the temporal evolution of the spatial distributions generated using molecular dynamics (MD). Kinetic Monte Carlo (OKMC) was employed to simulate the formation of defect clusters and the spatial distribution of them over time. During extended storage conditions, temperature fluctuations influence the size and density distribution of the resulting microstructures. For this step, a cluster dynamics routine was developed and

applied using rate theory algorithms to determine the size distribution and the formation sites of defect clusters.

During the course of the work, a feasibility study was conducted on the multiscale investigation of radiation-induced material degradation and the resulting structural-mechanical strength or failure behavior of the cladding tubes.

As part of the validation of the multiscale modelling sequence, TEM-based characterization of microstructures was conducted on cladding tube samples obtained from the HIFR reactor. Multiscale modelling sequences were validated using the results of model calculations based on the above experiments.

An in-depth understanding of a material's microstructure provides the basis for modeling its mechanical behavior correlating its macroscopic properties with its microstructural configuration. The change of the material parameters like yield strength and geometrical elongation (resulting from the multiscale simulations) was investigated. Material degradation and its impact on the SNF cladding structure have been studied in all cases (after LWR operating phase, extended dry interim storage period (60 years), and experimentally parametrized under HFIR irradiation conditions). Using a multiscale simulation, the material hardening and radiation growth that result from radiation-induced microstructure development and formation have been examined. To assess the model's sensitivity to major input parameters (irradiation temperature, alloy content, and dose rate), parametric multiscale simulations were conducted. Using experimentally conditioned cases and structural-mechanical measurements, validation was carried out.

Physico-chemical processes such as precipitation and hydride formation, in combination with radiation damage, can also lead to material damage. A key aspect of assessing the component behavior and integrity of cladding tubes is to monitor how microstructural damage develops in the direction of crack initiation and propagation as a result of thermomechanical stresses and external mechanical loads. Investigations are being conducted using continuum mechanics with crystal plasticity models like finite elements to study these effects.

It is concluded that the entire process chain of radiation-induced material damage has been simulated using a multiscale computational model, and that utilizing this

procedure, precise information can be gained about the temporal change of structural-mechanical property variables in irradiated cladding tubes.

12.2 Outlook

In addition to determining macroscopic or structural-mechanical material parameters, the method provides an alternative to costly structural-mechanical or fracture-mechanical tests that are used for assessing the integrity of spent fuel assemblies. Utilization of this method and its results also provide a basis for studying the relationship between microstructural configuration and material properties as realized and demonstrated in this work. Additionally, the use of the characteristic values can be used to determine the structural-mechanical behavior of the material and therefore to evaluate the component under different irradiation and operational conditions.

The presented feasibility study, due to its innovative nature and multi-scale nature, has a prominent level of potential with respect to the implementations to approximate real conditions in different variations. Long-term research will be required to build high level version for more sophisticated applications. The modelling and simulation work and study performed during the course of the project will form the scientific groundwork for further research and development initiatives and activities. In this regard following research developments are of priority and particular importance:

- For the MD part of multiscale method, advanced potential models for interatomic interactions are needed to improve the simulation quality of the defect cascade formation at every scale using advanced theoretical and numerical methods (partly based on Ab-Initio method).

- Modeling and Simulation of the aggregation process and interaction effects of impurity atoms (such as Fe, Cr, and Sn) and defects towards the microstructure development using the MD and OKMC methods.

- The formation of zirconium hydrides results also considerably in material degradation with influence on the material properties of the cladding

structure. The interaction of the hydride structures and radiation defects and the resulting microstructural agglomeration based on the diffusion process is a fundamental issue for modelling to be involved in the MD and KMC-part of the whole multiscale model.

- Further study aiming at the optimization of the parameter-based correlations between the individual parts of damage process and of the interfaces using theoretical interaction model including the simulation uncertainties should be initiated and realized.

- In this study the effect of the radiation induced microstructures on the macroscopic material properties has been studied based on correlations between defect configuration and continuum mechanical parameters. For a precise simulation of the final impact of the radiation damage and fracture mechanics under macroscopic stress conditions (thermos-mechanical and/or external load), the application of the high-grade continuum mechanical method (finite elements) encompassing the enhanced models for the process of crack initiation, propagation and finally the fracture behavior of the cladding part of fuel elements are needed to cover the whole range of integrity study.

13 References

[1] Kernkraft, E.ON. Stilllegung und Rückbau des Kernkraftwerks - vom Kernkraftwerk zur Grünen Wiese. Hannover; 2008.

[2] Bröskamp, H., Brammer, K. J., & Graf, R. (editor). Endlagerung radioaktiver Abfälle in Deutschland: Abfallaufkommen und Endlagerverfügbarkeit aus EVU-Sicht; 2004.

[3] KTMAT13 Commission for the Storage of High Level Radioactive Waste. Verzeichnis radioaktiver Abfälle: Balance as of December 31, 2013 and forecast; 2013.

[4] Recommendation of the Disposal Commission ESK Guidelines for the Interim Storage of Radioactive Waste with Negligible Heat Generation. In: Bundesanzeiger AT 22.01.2014 B3. p. 2–47.

[5] La Rubia TD de, Bulatov VV. Materials Research by Means of Multiscale Computer Simulation. MRS Bull. 2001;26(3):169–75.

[6] Lu G, Kaxiras E. An Overview of Multiscale Simulations of Materials. arXiv; 2004.

[7] Domain C, Becquart CS. Object Kinetic Monte Carlo (OKMC): A Coarse-Grained Approach to Radiation Damage. In: Handbook of Materials Modeling. Cham: Springer International Publishing; 2020. p. 1287–312.

[8] Lucas GE. Effects of radiation on the mechanical properties of structural materials. Journal of Nuclear Materials 1994;216:322–5.

[9] Phythian WJ, English CA. Microstructural evolution in reactor pressure vessel steels. Journal of Nuclear Materials 1993;205:162–77.

[10] English CA, Phythian WJ, McElroy R-J. Microstructure and Modelling of RPV Embrittlement. MRS Proc. 1996;439.

[11] Eason, E. D., Wright, J. E., & Odette, G. R. An improved embrittlement correlation for reactor pressure vessel steels.

[12] aSTM Standard e900-02. Predicting radiation-Induced Transition Temperature Shift in reactor Vessel Materials,' e706 (IIF). 12th ed. West Conshohocken, Pa: American Society for Testing and Materials.

[13] Malerba L, Caturla MJ,et al. Multiscale modelling for fusion and fission materials: The M4F project. Nuclear Materials and Energy 2021;29:101051.

[14] Malerba L. Multi-scale modelling of irradiation effects in nuclear power plant materials. Understanding and Mitigating Ageing in Nuclear Power Plants 2010:456–543.

[15] McDowell DL. Modeling and experiments in plasticity. International Journal of Solids and Structures 2000;37(1-2):293–309.

[16] van Houtte P, Kanjarla AK, van Bael A, Seefeldt M, Delannay L. Multiscale modelling of the plastic anisotropy and deformation texture of polycrystalline materials. European Journal of Mechanics - A/Solids 2006;25(4):634–48.

[17] Zeman J, Šejnoha M. From random microstructures to representative volume elements. Modelling Simul. Mater. Sci. Eng. 2007;15(4):S325-S335.

[18] Odette GR, Wirth BD, Bacon DJ, Ghoniem NM. Multiscale-Multiphysics Modeling of Radiation-Damaged Materials: Embrittlement of Pressure-Vessel Steels. MRS Bull. 2001;26(3):176–81.

[19] Wirth B, Odette G, et al. Multiscale modeling of radiation damage in Fe-based alloys in the fusion environment. Journal of Nuclear Materials 2004;329-333:103–11.

[20] Becquart CS. RPV steel microstructure evolution under irradiation: a multiscale approach. Nuclear Instruments and Methods in Physics Research Section B: Beam Interactions with Materials and Atoms 2005;228(1-4):111–21.

[21] Nguyen-Manh D, Dudarev SL. Multi-scale modelling of materials for fusion power plants. Computational Materials Science 2006;36(1-2):112–6.

[22] Dudarev SL, Boutard J-L, et al. The EU programme for modelling radiation effects in fusion reactor materials: An overview of recent advances and future goals. Journal of Nuclear Materials 2009;386-388:1–7.

[23] Victoria M, Dudarev S, et al. Modelling irradiation effects in fusion materials. Fusion Engineering and Design 2007;82(15-24):2413–21.

[24] CASL. Advanced Simulation of Light Water Reactors; Available from: https://casl.gov/ (January, 2023).

[25] Turner JA, Clarno K, Sieger M, Bartlett R, Collins B, Pawlowski R, Schmidt R, Summers R. The Virtual Environment for Reactor Applications (VERA): Design and architecture. Journal of Computational Physics 2016;326:544–68.

[26] Jumel S, Domain C, et al. Simulation of the irradiation effects in reactor materials The REVE project. J. Phys. IV France 2000;10(PR6): Pr6-191-Pr6-196.

[27] Jumel S, Domain C, et al. Simulation of irradiation effects in reactor pressure vessel steels: the Reactor for Virtual Experiments (REVE) project. Journal Of Testing and Evaluation 2002;30(1).

[28] Jumel S. RPV-1: a first virtual reactor to simulate irradiation effects in light water reactor pressure vessel steels; 2005.

[29] Jumel S, Van-Duysen JC. RPV-1: A Virtual Test Reactor to simulate irradiation effects in light water reactor pressure vessel steels. Journal of Nuclear Materials 2005;340(2-3):125–48.

[30] Adjanor G, Bugat S, Domain C, Barbu A. Overview of the RPV-2 and INTERN-1 packages: From primary damage to microplasticity. Journal of Nuclear Materials 2010;406(1):175–86.

[31] Becquart CS, Decker KM, Domain C, Ruste J, Souffez Y, Turbatte JC, van Duysen JC. Massively parallel molecular dynamics simulations with EAM potentials. Radiation Effects and Defects in Solids 1997;142(1-4):9–21.

[32] Domain C, Becquart CS, Malerba L. Simulation of radiation damage in Fe alloys: an object kinetic Monte Carlo approach. Journal of Nuclear Materials 2004;335(1):121–45.

[33] Odette GR, Wirth BD. A computational microscopy study of nanostructural evolution in irradiated pressure vessel steels. Journal of Nuclear Materials 1997;251:157–71.

[34] Liu CL, Odette GR, Wirth BD, Lucas GE. A lattice Monte Carlo simulation of nanophase compositions and structures in irradiated pressure vessel Fe-Cu-Ni-Mn-Si steels. Materials Science and Engineering: A 1997;238(1):202–9.

[35] Leclercq S, Lidbury D, van Dyck S, Moinereau D, Alamo A, Mazouzi AA. PERFORM 60 – Prediction of the effects of radiation for reactor pressure vessel and in-core materials using multi-scale modelling – 60years foreseen plant lifetime. Journal of Nuclear Materials 2010;406(1):193–203.

[36] Al Mazouzi A, Alamo A, Lidbury D, Moinereau D, van Dyck S. PERFORM 60: Prediction of the effects of radiation for reactor pressure vessel and in-core materials using multi-scale modelling – 60 years foreseen plant lifetime. Nuclear Engineering and Design 2011;241(9):3403–15.

[37] Fazio C, Briceno DG, Rieth M, Gessi A, Henry J, Malerba L. Innovative materials for Gen IV systems and transmutation facilities: The cross-cutting research project GETMAT. Nuclear Engineering and Design 2011;241(9):3514–20.

[38] Fazio C, Alamo A, Almazouzi A, Grandis S de, Gomez-Briceno D, Henry J, Malerba L, Rieth M. European cross-cutting research on structural materials for Generation IV and transmutation systems. Journal of Nuclear Materials 2009;392(2):316–23.

[39] JPNM. The Joint Programme on Nuclear Materials of the European Energy Research Alliance; Available from: http://www.eera-jpnm.eu/ (January, 2023).

[40] M4F. Multiscale modeling for fusion and fission materials; Available from: http://www.h2020-m4f.eu/ (January, 2023).

[41] Murty KL, Charit I. An introduction to nuclear materials: Fundamentals and applications. Weinheim: Wiley-VCH; 2013.

[42] Ide creation Play Bac and AREVA. A Nuclear Power Plant.

[43] PreussenElektra GmbH. Kernkraftwerk Isar: Umwelterklärung 2021; 2021.

[44] Ministerium für Umwelt, Klima und Energiewirtschaft Baden-Württermberg. GKN II - General information.

[45] Hengstler-Eger RM. Ion irradiation studies of the origins of pressurized water reactor fuel assembly deformation: Doctoral dissertation; 2012.

[46] Olander, D., & Motta, A. Zirconium alloys: Light-Water Reactor Materials; 2009.

[47] Duan Z, Yang H, Satoh Y, Murakami K, Kano S, Zhao Z, Shen J, Abe H. Current status of materials development of nuclear fuel cladding tubes for light water reactors. Nuclear Engineering and Design 2017;316:131–50.

[48] Weidinger H (editor). Zr-alloys, the nuclear material for water reactor fuel. A survey and update with focus on fuel for pressurized water reactor systems; 2008.

[49] Gebhardt, E., Thümmler, F., & Seghezzi, H. D. Reaktorwerkstoffe: Metallische Werkstoffe. Teubner; 1964.

[50] Kopitzki K. Einführung in die Festkörperphysik. 3rd ed. Stuttgart: Teubner; 1993.

[51] ASTM B350. Standard Specification for Zirconium and Zirconium Alloy Ingots for Nuclear Application; 2021.

[52] Hesterberg J., Smith R., & Was G. S. (2019). Atomistic simulation of the obstacle strengths of radiation-induced defects in an Fe–Ni–Cr austenitic stainless steel. Modelling and Simulation in Materials Science and Engineering, 27(8), 085004..

[53] Adamson RB. Effects of neutron irradiation on microstructure and properties of Zircaloy: Zirconium in the nuclear industry: Twelfth international symposium. ASTM Special Technical Publication, ASTM International; 2000.

[54] Cockeram BV, Leonard KJ, Byun TS, Snead LL, Hollenbeck JL. Development of microstructure and irradiation hardening of Zircaloy during low dose neutron irradiation at nominally 377–440°C. Journal of Nuclear Materials 2014;449(1-3):69–87.

[55] Griffiths M. A review of microstructure evolution in zirconium alloys during irradiation. Journal of Nuclear Materials 1988;159:190–218.

[56] Griffiths M (editor). Microstructure Evolution in Zr Alloys during Irradiation: Dose, Dose Rate, and Impurity Dependence: Zirconium in the Nuclear Industry: 15th International Symposium. 100 Barr Harbor Drive, PO Box C700, West Conshohocken, PA 19428-2959: ASTM International; 2009.

[57] Gilbert RW, Farrell K, Coleman CE. Damage structure in zirconium alloys neutron irradiated at 573 to 923 k. Journal of Nuclear Materials 1979;84(1-2):137–48.

[58] Griffiths M, Gilbert RW. The formation of c-component defects in zirconium alloys during neutron irradiation. Journal of Nuclear Materials 1987;150(2):169–81.

[59] Choi Sil, Kim Jh. Radiation-Induced Dislocation And Growth Behavior Of Zirconium And Zirconium Alloys – A Review. Nuclear Engineering and Technology 2013;45(3):385–92.

[60] Northwood DO, Gilbert R, Bahen LE, Kelly PM, Blake RG, Jostsons A, Madden PK, Faulkner D, Bell W, Adamson RB. Characterization of neutron

irradiation damage in zirconium alloys — an international “round-robin” experiment. Journal of Nuclear Materials 1979;79(2):379–94.

[61] Jostsons A, Kelly PM, Blake RG. The nature of dislocation loops in neutron irradiated zirconium. Journal of Nuclear Materials 1977;66(3):236–56.

[62] Woo CH, Liu X. Generation of c-component edge dislocations in α-zirconium during neutron irradiation – An atomistic study. Journal of Nuclear Materials 2009;393(3):513–7.

[63] Holt RA, Gilbert RW. 〈〉 Component dislocations in annealed Zircaloy irradiated at about 570 K. Journal of Nuclear Materials 1986;137(3):185–9.

[64] Bell W. Corduroy contrast observations in neutron-irradiated zirconium and zircaloy. Journal of Nuclear Materials 1975;55(1):14–22.

[65] Idrees Y, Yao Z, Kirk MA, Daymond MR. In situ study of defect accumulation in zirconium under heavy ion irradiation. Journal of Nuclear Materials 2013;433(1-3):95–107.

[66] Holt RA, Causey AR. Volume conservation during irradiation growth of Zr–2.5Nb. Journal of Nuclear Materials 2004;335(3):529–33.

[67] Griffiths M. Evolution of microstructure in hcp metals during irradiation. Journal of Nuclear Materials 1993;205:225–41.

[68] Griffiths M, Gilbert RW, Fidleris V, Tucker RP, Adamson RB. Neutron damage in zirconium alloys irradiated at 644 to 710 k. Journal of Nuclear Materials 1987;150(2):159–68.

[69] Jostsons A, Kelly PM, Blake RG, Farrell K (editors). Neutron Irradiation-Induced Defect Structures in Zirconium. ASTM International; 1979.

[70] Northwood DO. Irradiation damage in zirconium and its alloys. Atomic Energy Review 1977;15(4):547–610.

[71] Northwood DO, Gilbert RW. Neutron radiation damage in zirconium and its alloys. Radiation Effects 1974;22(2):139–40.

[72] Gaumé M, Onimus F, Dupuy L, Tissot O, Bachelet C, Mompiou F. Microstructure evolution of recrystallized Zircaloy-4 under charged particles irradiation. Journal of Nuclear Materials 2017;495:516–28.

[73] Cockeram BV, Smith RW, Leonard KJ, Byun TS, Snead LL. Development of microstructure and irradiation hardening of Zircaloy during low dose neutron

irradiation at nominally 358°C. Journal of Nuclear Materials 2011;418(1-3):46–61.

[74] Jostsons A, Blake RG, Napier JG, Kelly PM, Farrell K. Faulted loops in neutron-irradiated zirconium. Journal of Nuclear Materials 1977;68(3):267–76.

[75] Tucker, R. P., Fidleris, V., & Adamson, R. B. (editor). Zirconium Alloys at 644 to 725 K.: Zirconium in the nuclear industry Sixth international symposium. Philadelphia, Pa: American Society for Testing and Materials; 1984.

[76] Gilbon D, Simonot C. Effect of Irradiation on the Microstructure of Zircaloy-4. In: Zirconium in the Nuclear Industry: Tenth International Symposium. 100 Barr Harbor Drive, PO Box C700, West Conshohocken, PA 19428-2959: ASTM International; null. 521-521-28.

[77] Bossis P, Verhaeghe B, Doriot S, Gilbon D, Chabretou V, Dalmais A, Mardon J-P, Blat M, Miquet A. In PWR Comprehensive Study of High Burn-Up Corrosion and Growth Behavior of M5® and Recrystallized Low-Tin Zircaloy-4. In: Zirconium in the Nuclear Industry: 15th International Symposium. 100 Barr Harbor Drive, PO Box C700, West Conshohocken, PA 19428-2959: ASTM International; null. 430-430-27.

[78] Woo C. Defect accumulation behaviour in hcp metals and alloys. Journal of Nuclear Materials 2000;276(1-3):90–103.

[79] Abromeit C, Naundorf V, Wollenberger H. Phase stability criteria for ion and neutron irradiated alloys. Journal of Nuclear Materials 1988;155-157:1174–8.

[80] Hood GM. Point defect diffusion in α-Zr. Journal of Nuclear Materials 1988;159:149–75.

[81] Motta AT, Lemaignan C. A ballistic mixing model for the amorphization of precipitates in Zircaloy under neutron irradiation. Journal of Nuclear Materials 1992;195(3):277–85.

[82] Harte A, Jädernäs D, Topping M, Frankel P, Race CP, Romero J, Hallstadius L, Darby EC, Preuss M. The effect of matrix chemistry on dislocation evolution in an irradiated Zr alloy. Acta Materialia 2017;130:69–82.

[83] Anand MS, Mansel W, Wallner G, Weck W. Effect of alloying elements on recovery and damage rates in zirconium. Journal of Nuclear Materials 1984;126(2):144–51.

[84] Griffiths M, Gilbon D, Regnard C, Lemaignan C. HVEM study of the effects of alloying elements and impurities on radiation damage in Zr-alloys. Journal of Nuclear Materials 1993;205:273–83.

[85] Harte A, Topping M, Frankel P, Jädernäs D, Romero J, Hallstadius L, Darby EC, Preuss M. Nano-scale chemical evolution in a proton-and neutron-irradiated Zr alloy. Journal of Nuclear Materials 2017;487:30–42.

[86] Higgy HR, Hammad FH. Effect of neutron irradiation on the tensile properties of zircaloy-2 and zircaloy-4. Journal of Nuclear Materials 1972;44(2):215–27.

[87] Holt RA (editor). In-Reactor Deformation of Zirconium Alloy Components: Zirconium in the Nuclear Industry: 15th International Symposium. 100 Barr Harbor Drive, PO Box C700, West Conshohocken, PA 19428-2959: ASTM International; 2009.

[88] Bertsch J, Hoffelner W. Fracture Toughness of Zircaloy Claddings; 2003.

[89] Machiels A. Fracture Toughness Data for Zirconium Alloys Application to Spent Fuel Cladding in Dry Storage EPRI Project Manager. EPRI Palo Alto, CA.

[90] Onimus F., Doriot S., & Béchade J. L. (2020). Radiation effects in zirconium alloys.

[91] Adamson RB, Coleman CE, Griffiths M. Irradiation creep and growth of zirconium alloys: A critical review. Journal of Nuclear Materials 2019;521:167–244.

[92] Savino EJ, Laciana CE. Radiation induced creep and growth of zirconium alloys. Journal of Nuclear Materials 1980;90(1-3):89–107.

[93] Rogerson A. Irradiation growth in zirconium and its alloys. Journal of Nuclear Materials 1988;159:43–61.

[94] Murgatroyd RA, Rogerson A. Irradiation growth in annealed zircaloy-2. Journal of Nuclear Materials 1979;79(2):302–11.

[95] Hayes TA, Rosen RS, Kassner ME. Creep fracture of zirconium alloys. Journal of Nuclear Materials 2006;353(1-2):109–18.

[96] LUNA, I., SICILIA, A. M., PAN, G., & LONG, Y. IN-REACTOR CREEP BEHAVIOR OF ZIRLO® AND OPTIMIZED ZIRLOTM CLADDING; 2018.

[97] Lemaignan C. 2.07-Zirconium alloys: properties and characteristics: Comprehensive nuclear materials; 2012.

[98] Onimus F, Béchade JL, Duguay C, Gilbon D, Pilvin P. Investigation of neutron radiation effects on the mechanical behavior of recrystallized zirconium alloys. Journal of Nuclear Materials 2006;358(2-3):176–89.

[99] Tournadre L, Onimus F, Béchade J-L, Gilbon D, Cloué J-M, Mardon J-P, Feaugas X. Toward a better understanding of the hydrogen impact on the radiation induced growth of zirconium alloys. Journal of Nuclear Materials 2013;441(1-3):222–31.

[100] Le Saux M, Besson J, Carassou S, Poussard C, Averty X. A model to describe the anisotropic viscoplastic mechanical behavior of fresh and irradiated Zircaloy-4 fuel claddings under RIA loading conditions. Journal of Nuclear Materials 2008;378(1):60–9.

[101] Torimaru T, Yasuda T, Nakatsuka M. Changes in mechanical properties of irradiated Zircaloy-2 fuel cladding due to short term annealing. Journal of Nuclear Materials 1996;238(2-3):169–74.

[102] Byun T, Farrell K. Irradiation hardening behavior of polycrystalline metals after low temperature irradiation. Journal of Nuclear Materials 2004;326(2-3):86–96.

[103] Ere B, AME G. Zirconium in the nuclear industry: 10th International symposium Papers. ASTM International; 1994.

[104] Holt R. A., Griffiths M., & Gilbert R. W. c-component dislocations in Zr-2.5 wt% Nb alloy. Journal of Nuclear Materials 1987;149(1):51–6.

[105] IAEA. Practices and developments in spent fuel burnup credit applications: TECDOC 1378; 2003.

[106] Adamson R. B., & Bell W. L. (editor). Irradiation Damage in Zirconium Alloys. ASTM International; 1974.

[107] Ullmaier H, Schilling W (editors). Radiation damage in metallic reactor materials: Physics of modern materials. Characterization of materials, defects, and mechanical properties; 1980.

[108] Stoller RE. Radiation Damage: Mechanisms and Modeling. Oak Ridge National Laboratory; 2012.

[109] Glasstone S., & Sesonske A. Nuclear reactor engineering: Reactor design basics. 4th ed. United States: Chapman and Hall; 1994.

[110] Olander D., and Motta A. Light water reactor materials. Chapter 12: Radiation Damage; 2013.

[111] Was GS. Fundamentals of radiation materials science: Metals and alloys. New York: Springer; 2007.

[112] Johnson L.H. and Shoesmith D.W. (editor). Spent Fuel: Radioactive Waste Forms for the Future, Elsevier Science; 1988.

[113] Doran D. G. Effects of Radiation on Reactor Structural Alloys: ASTM-STP 570. ASTM; 1976.

[114] Wooding S, Howe L, Gao F, Calder A, Bacon D. A molecular dynamics study of high-energy displacement cascades in α-zirconium. Journal of Nuclear Materials 1998;254(2-3):191–204.

[115] Calder A. F., Bacon D. J., Barashev A. V., & Osetsky Y. N. (2010). On the origin of large interstitial clusters in displacement cascades. Philosophical Magazine, 90(7-8), 863-884.

[116] Smith AB, Guenther PT. Fast neutron scattering cross sections of elemental zirconium; 1982.

[117] La Rubia TD de, Phythian WJ. Molecular dynamics studies of defect production and clustering in energetic displacement cascades in copper. Journal of Nuclear Materials 1992;191-194:108–15.

[118] Calder AF, Bacon DJ. A molecular dynamics study of displacement cascades in α-iron. Journal of Nuclear Materials 1993;207:25–45.

[119] La Rubia T de, Guinan MW. Progress in the development of a molecular dynamics code for high-energy cascade studies. Journal of Nuclear Materials 1990;174(2-3):151–7.

[120] Nordlund K, Ghaly M, Averback RS, Caturla M, La Diaz de Rubia T, Tarus J. Defect production in collision cascades in elemental semiconductors and fcc metals. Phys. Rev. B 1998;57(13):7556–70.

[121] Björkas, C., Nordlund, K., & Caturla, M. J. Influence of the picosecond defect distribution on damage accumulation in irradiated -Fe. Phys. Rev. B 2012;85(2):24105.

[122] Le Page J, Mason DR, Race CP, Foulkes WMC. How good is damped molecular dynamics as a method to simulate radiation damage in metals? New J. Phys. 2009;11(1):13004.

[123] Becquart CS, Domain C, van Duysen JC, Raulot JM. The role of Cu in displacement cascades examined by molecular dynamics. Journal of Nuclear Materials 2001;294(3):274–87.

[124] Brinkman JA. Production of Atomic Displacements by High-Energy Particles. American Journal of Physics 1956;24(4):246–67.

[125] Silsbee RH. Focusing in Collision Problems in Solids. Journal of Applied Physics 1957;28(11):1246–50.

[126] Smith AB, Guenther PT. Fast-neutron scattering cross sections of elemental zirconium; 1982.

[127] Wirth BD. An introduction to Material Degradation in Nuclear Environment. Lecture Notes. Berkeley, USA; (2006).

[128] Thompson MW. Defects and Radiation Damage in Metals. Cambridge, UK: Cambridge University Press; 1974.

[129] IAEA. Development of Radiation resistant reactor core structural materials; 2014.

[130] Puigví MA, Diego N de, Serra A, Osetsky YN, Bacon DJ. On the interaction between a vacancy and self-interstitial atom clusters in metals. Philosophical Magazine 2007;87(23):3501–17.

[131] Diego N de, Osetsky Y, Bacon DJ. Structure and properties of vacancy and interstitial clusters in α-zirconium. Journal of Nuclear Materials 2008;374(1-2):87–94.

[132] Diego N de, Serra A, Bacon DJ, Osetsky YN. On the structure and mobility of point defect clusters in alpha-zirconium: a comparison for two interatomic potential models. Modelling Simul. Mater. Sci. Eng. 2011;19(3):35003.

[133] Stoller R. Radiation Damage: Mechanisms and Modeling. Oak Ridge National Laboratory; 2012.

[134] Stoller RE. Radiation Damage Fundamentals: Primary Damage Production; 2011.

[135] Diego N de, Osetsky YN, Bacon DJ. Mobility of Interstitial Clusters in HCP Zirconium. MRS Proc. 2000;650.

[136] Eridon J, Rehn L, Was G. Metastable phase formation in nickel-aluminum alloys during ion beam mixing. Nuclear Instruments and Methods in Physics

Research Section B: Beam Interactions with Materials and Atoms 1987;19-20:626–31.

[137] Brimhall JL, Kissinger HE, Charlot LA. Amorphous phase formation in irradiated intermetallic compounds. Radiation Effects 1983;77(3-4):273–93.

[138] Stoller RE, Golubov SI, Domain C, Becquart CS. Mean field rate theory and object kinetic Monte Carlo: A comparison of kinetic models. Journal of Nuclear Materials 2008;382(2-3):77–90.

[139] Goorley T, James M, et al. Initial MCNP6 Release Overview. Nuclear Technology 2012;180(3):298–315.

[140] Pelowitz DB. MCNP6TM user's manual version 1.0. 1st ed. Los Alamos National Laboratory; 2013.

[141] Greenwood LR, Smither RK. SPECTER: neutron damage calculations for materials irradiations; 1985.

[142] Gilbert, M. R., Marian, J., & Sublet, J. C. Energy spectra of primary knock-on atoms under neutron irradiation. Journal of Nuclear Materials 2015;467:121–34.

[143] Sublet J-C, Eastwood JW, Morgan JG, Gilbert MR, Fleming M, Arter W. FISPACT-II: An Advanced Simulation System for Activation, Transmutation and Material Modelling. Nuclear data sheets 2017;139:77–137.

[144] Motta AT, Olander DR (editors). Chapter 12 - Radiation Damage: Light-Water Reactor Materials. American Nuclear Society; 2006.

[145] Magurno BA, Kinsey RR, Scheffel FM. Guidebook for the ENDF/B-V nuclear data files.

[146] Nordlund K, Zinkle SJ, et al. Primary radiation damage: A review of current understanding and models. Journal of Nuclear Materials 2018;512:450–79.

[147] Konobeyev A, Fischer U, Korovin Y, Simakov SP. Evaluation of effective threshold displacement energies and other data required for the calculation of advanced atomic displacement cross-sections. Nuclear Energy and Technology 2017;3(3):169–75.

[148] Ercolessi F. A molecular dynamics primer: ICTP. Trieste; 1997.

[149] Allen MP. Introduction to molecular dynamics simulation: Lecture Notes. Computational soft matter: from synthetic polymers to proteins 2004;23((1)):1–28.

[150] Atkinson, K. E., & Han, W. Elementary numerical analysis. 2nd ed. New York: John Wiley Sons; 1993.

[151] Gear CW. Numerical initial value problems in ordinary differential equations. Prentice-Hall Series in Automatic Computation 1971.

[152] Narayan K, Behdinan K, Fawaz Z. An engineering-oriented embedded-atom-method potential fitting procedure for pure fcc and bcc metals. Journal of Materials Processing Technology 2007;182(1-3):387–97.

[153] Calder AF, Bacon DJ. A molecular dynamics study of displacement cascades in α-iron. Journal of Nuclear Materials 1993;207:25–45.

[154] Bacon DJ, Calder AF, Gao F. Defect production due to displacement cascades in metals as revealed by computer simulation. Journal of Nuclear Materials 1997;251:1–12.

[155] Lu J. Computer modeling of intergranular fracture in textured materials 1995.

[156] Daw MS, Foiles SM, Baskes MI. The embedded-atom method: a review of theory and applications. Materials Science Reports 1993;9(7-8):251–310.

[157] Becquart CS, Domain C, Sarkar U, DeBacker A, Hou M. Microstructural evolution of irradiated tungsten: Ab initio parameterisation of an OKMC model. Journal of Nuclear Materials 2010;403(1-3):75–88.

[158] F. Gao, D.J. Bacon, A.V. Barashev, H.L. Heinisch. Mater. Res. SocSymp. P 540 1999:703–8.

[159] Caturla MJ, Soneda N, Alonso E, Wirth BD, La Díaz de Rubia T, Perlado JM. Comparative study of radiation damage accumulation in Cu and Fe. Journal of Nuclear Materials 2000; 276(1-3):13–21.

[160] Barashev AV, Bacon DJ, Golubov SI. Monte Carlo modelling of damage accumulation in metals under cascade irradiation. Journal of Nuclear Materials 2000;276(1-3):243–50.

[161] Domain C, Becquart CS, Malerba L. Simulation of radiation damage in Fe alloys: an object kinetic Monte Carlo approach. Journal of Nuclear Materials 2004;335(1):121–45.

[162] Nandipati G, Setyawana W, et al. Object Kinetic Monte Carlo Simulations of Radiation Damage in Neutron-Irradiated Tungsten Part-I: Neutron Flux with a PKA Spectrum Corresponding to the High-flux Isotope Reactor. arXiv; 2015.

[163] Phythian WJ, English CA. Microstructural evolution in reactor pressure vessel steels. Journal of Nuclear Materials 1993;205:162–77.

[164] Brailsford AD, Bullough R. The rate theory of swelling due to void growth in irradiated metals. Journal of Nuclear Materials 1972;44(2):121–35.

[165] Jourdan T, Crocombette J-P. Rate theory cluster dynamics simulations including spatial correlations within displacement cascades. Phys. Rev. B 2012;86(5).

[166] Plimpton S. Fast Parallel Algorithms for Short-Range Molecular Dynamics. Journal of Computational Physics 1995;117(1):1–19.

[167] Stukowski A. Visualization and analysis of atomistic simulation data with OVITO–the Open Visualization Tool. Modelling Simul. Mater. Sci. Eng. 2010;18(1):15012.

[168] Nandipati G, Setyawan W, et al. Object Kinetic Monte Carlo Simulations Of Microstructure Evolution. arXiv; 2013.

[169] Pomraning GC. The Wigner-Seitz Cell; A Discussion and a Simple Calculational Method. Nuclear Science and Engineering 1963;17(2):311–4.

[170] Virtanen P, Gommers R, et al. SciPy 1.0: fundamental algorithms for scientific computing in Python. Nat Methods 2020;17(3):261–72.

[171] Stukowski A. Structure identification methods for atomistic simulations of crystalline materials. Modelling Simul. Mater. Sci. Eng. 2012;20(4):45021.

[172] Nandipati G, Setyawan W, et al. Object Kinetic Monte Carlo Simulations of Radiation Damage in Bulk Tungsten. APS Division of Plasma Physics Meeting Abstracts 2015;2015:JM11.007.

[173] Mendelev MI, Ackland GJ. Development of an interatomic potential for the simulation of phase transformations in zirconium. Philosophical Magazine Letters 2007;87(5):349–59.

[174] Bierbaum M, Tadmor E, et al. OpenKIM - Building a Knowledgebase of Interatomic Models. APS March Meeting Abstracts 2014;2014: T26.004.

[175] Liu S-M, Beyerlein IJ, Han W-Z. Two-dimensional vacancy platelets as precursors for basal dislocation loops in hexagonal zirconium. Nat Commun 2020;11(1):5766.

[176] Yu H, Yao Z, Idrees Y, Zhang HK, Kirk MA, Daymond MR. Accumulation of dislocation loops in the α phase of Zr Excel alloy under heavy ion irradiation. Journal of Nuclear Materials 2017;491:232–41.

[177] Wilson SR, Mendelev MI. Anisotropy of the solid–liquid interface properties of the Ni–Zr B33 phase from molecular dynamics simulation. Philosophical Magazine 2015;95(2):224–41.

[178] Moore AP, Beeler B, Deo C, Baskes MI, Okuniewski MA. Atomistic modeling of high temperature uranium–zirconium alloy structure and thermodynamics. Journal of Nuclear Materials 2015;467:802–19.

[179] Christensen M, Wolf W, et al. Effect of alloying elements on the properties of Zr and the Zr–H system. Journal of Nuclear Materials 2014;445(1-3):241–50.

[180] Ackland GJ, Wooding SJ, Bacon DJ. Defect, surface, and displacement-threshold properties of α-zirconium simulated with a many-body potential. Philosophical Magazine A 1995;71(3):553–65.

[181] Ribis J, Onimus F, Béchade J-L, Doriot S, Barbu A, Cappelaere C, Lemaignan C. Experimental study, and numerical modelling of the irradiation damage recovery in zirconium alloys. Journal of Nuclear Materials 2010;403(1-3):135–46.

[182] Golubov SI, Barashev A, Stoller RE. On the origin of radiation growth of hcp crystals. Office of Scientific and Technical Information (OSTI); 2012.

[183] Choi S, Kim T, Shin S, Lee G, Kwon J, Kim JH. Modeling irradiation growth of zirconium and its alloy in nuclear reactors. 0003-018X 2014.

[184] Christien F, Barbu A. Cluster Dynamics modelling of irradiation growth of zirconium single crystals. Journal of Nuclear Materials 2009;393(1):153–61.

[185] Busby JT, Hash MC, Was GS. The relationship between hardness and yield stress in irradiated austenitic and ferritic steels. Journal of Nuclear Materials 2005;336(2-3):267–78.

[186] Osetsky YN, Bacon DJ, Diego N de. Anisotropy of point defect diffusion in alpha-zirconium. Metall and Mat Trans A 2002;33(13):777–82.

[187] Stukowski A. Computational Analysis Methods in Atomistic Modeling of Crystals. JOM 2014;66(3):399–407.

[188] Gao F, Wooding SJ, Bacon DJ, Calder AF, Howe LM. Computer Simulation of Displacement Cascades in α-Zirconium. MRS Proc. 1996;439.

[189] Takahashi A, Hirose K, Soneda N, Kikuchi M. Molecular Dynamics Simulation of Displacement Cascade in α-Zr. Fracture and Strength of Solids VI 2006;306-308:923–8.

[190] Gao F, Bacon DJ, Howe LM, So CB. Temperature-dependence of defect creation and clustering by displacement cascades in α-zirconium. Journal of Nuclear Materials 2001;294(3):288–98.

[191] Yang X, Zeng X, Chen L, Guo Y, Chen H, Wang F. Molecular dynamics simulations of the primary irradiation damage in Zirconium. Nuclear Instruments and Methods in Physics Research Section B: Beam Interactions with Materials and Atoms 2018;436:92–8.

[192] Zhou W, Tian J, Feng Q, Zheng J, Liu X, Xue J, Qian D, Peng S. Molecular dynamics simulations of high-energy displacement cascades in hcp-Zr. Journal of Nuclear Materials 2018;508:540–5.

[193] Orowan E. Fracture and strength of solids. Reports on Progress in Physics 1948;12:183.

[194] Lucas GE. The evolution of mechanical property change in irradiated austenitic stainless steels. Journal of Nuclear Materials 1993;206(2-3):287–305.

[195] Dollins CC. In-pile dimensional changes in neutron irradiated zirconium base alloys. Journal of Nuclear Materials 1976;59(1):61–76.

[196] Vérité G. Structure, stabilité et mobilité des défauts ponctuels dans le zirconium hexagonal compact étude ab initio; 2013.

[197] Rogerson A, Zee RH. High fluence irradiation growth in single crystal zirconium at 553 K. Journal of Nuclear Materials 1987;151(1):81–3.